PART I: RADIATIVE TRANSFER STUDIES AND OPACITY CALCULATIONS FOR HEATED GASES

PART II: ABSOLUTE INTENSITY MEASUREMENTS FOR THE 2.7 μ BAND OF WATER VAPOR IN A SHOCK TUBE

Thesis by

Richard Walker Patch

In Partial Fulfillment of the Requirements

For the Degree of

Doctor of Philosophy

California Institute of Technology

Pasadena, California

1964

(Submitted April 6, 1964)

ACKNOWLEDGMENTS

The author wishes to express his appreciation to Professor S. S. Penner for his helpful advice and guidance during the course of the research presented here.

Grateful appreciation is also extended to the National Science Foundation for three Graduate Fellowships. The United States Air Force contributed financial support to the research under Contract AF-49(638)984 and Grant AF-AFOSR-71-63.

Dr. T. A. Jacobs, Dr. R. A. Hartunian, and Mr. R. L. Wilkins of Aerospace Corporation were very generous with both their time and funds in accomplishing digital computer work for Part II. Professor W. H. Corcoran and Mr. J. W. Woodward provided much advice on gas chromatographs. Professor H. C. Martel helped in the design of the photodiode preamplifier.

The assistance of Mrs. W. D. Tingley in the preparation of this manuscript is also gratefully acknowledged.

ABSTRACT FOR PART I

Equations for radiative transfer of energy in hot gases are presented for cases involving absorption, spontaneous emission, induced emission, and isotropic scattering. Application of these equations to energy transfer between two infinite parallel plates and also to energy transfer to the nose cone of a reentry vehicle are reviewed.

The Planck and Rosseland mean free paths for radiation are derived. It is shown that the treatments by Nachbar and Simon can be combined to give the continuity, momentum, and energy equations for a reacting, multicomponent gas mixture with radiative energy transfer. The resulting equations are then nondimensionalized. The coupling of radiation and convection in detached shock layers is reviewed.

A simplified method for calculating spectral absorption coefficients for electronic bands of diatomic molecules is presented. A simplified method for calculating continuum radiation in plasmas is reviewed.

ABSTRACT FOR PART II

The apparent spectral absorption coefficients of the H_2O infrared bands in the vicinity of 2.7 μ were measured in a shock tube behind reflected shock waves in an H_2O-Ar mixture.

By interrupting an infrared beam at a 60 kc rate and projecting this beam across the shock tube to a monochromator, it was possible to simultaneously measure both emission and absorption of H_2O at 1000 ^{o}K. The spectral absorption coefficients obtained from emission

measurements averaged 9.8% higher than absorption coefficients obtained from absorption measurements, probably due to experimental errors (smaller than usually encountered in shock tube measurements). At 1933 ^{o}K experimental difficulties precluded simultaneous measurement of infrared emission and absorption, so measurements were restricted to emission.

The apparent absorption coefficients were integrated to give the integrated absorption coefficients for the collections of bands near 2.7 μ. Integrated absorption coefficients were 49.8 cm^{-2} atm^{-1}, 54.7 cm^{-2} atm^{-1}, and 31.6 cm^{-2} atm^{-1} for absorption at 1000 ^{o}K, emission at 1000 ^{o}K, and emission at 1933 ^{o}K, respectively. The two values at 1000 ^{o}K were in good agreement with those of Goldstein, who made no measurements above this temperature.

Photographic materials on pp. 100, 107, 111, 123, and 128 are essential and will not reproduce clearly on Xerox copies. Photographic copies should be ordered.

TABLE OF CONTENTS

SECTION	TITLE	PAGE
	PART I: RADIATIVE TRANSFER STUDIES AND OPACITY CALCULATIONS FOR HEATED GASES	
I.	INTRODUCTION	1
II.	THE FORMULATION OF RADIATIVE TRANSFER PROBLEMS	3
	A. Absorption and Induced Emission of Radiation	5
	B. Transfer of Radiation Without Scattering	6
	C. Absorption and Isotropic Scattering Without Spontaneous Emission of Radiation	7
	D. Absorption and Emission of Radiation and Isotropic Scattering	8
	E. Radiative Energy Transfer from Gases Confined Between Two Infinite Parallel Plates	8
	F. Radiative Energy Transfer to the Nose Cone of a Reentry Vehicle	13
III.	PLANCK AND ROSSELAND MEAN FREE PATHS	17
	A. The Planck Mean Absorption Coefficient	18
	B. The Rosseland Mean Absorption Coefficient	19
IV.	THE CONSERVATION EQUATIONS WITH RADIANT ENERGY TRANSPORT	25
	A. Species Conservation Equations	26
	B. Over-all Continuity Equation	29
	C. Momentum Equation	30
	D. Energy Equation	37

SECTION	TITLE	PAGE
V.	COUPLING OF RADIATION AND CONVECTION IN DETACHED SHOCK LAYERS	43
VI.	SPECTRAL ABSORPTION COEFFICIENTS IN MOLECULAR SYSTEMS	47
VII.	CONTINUUM RADIATION IN HEATED PLASMAS	57
	REFERENCES FOR PART I	64

PART II: ABSOLUTE INTENSITY MEASUREMENTS FOR THE 2.7 μ BAND OF WATER VAPOR IN A SHOCK TUBE

I.	INTRODUCTION	66
II.	THEORETICAL CONSIDERATIONS	73
	A. Vibration-Rotation Spectrum of H_2O Vapor	74
	B. The Slit Function	76
	C. Apparent Absorption Coefficient	79
	D. Shock Tube	81
	E. Absolute Intensity Calibration and Emission Measurements	83
III.	EXPERIMENTAL FACILITIES	91
	A. Shock Tube and Associated Measuring Apparatus	92
	B. Optical System	98
	C. Infrared Detection Electronics for Runs	112
	D. Gas Handling System	121
	E. Gas Chromatograph	125

SECTION	TITLE	PAGE
IV.	EXPERIMENTAL PROCEDURE	132
	A. Optical Preliminaries	132
	B. Preparation of the Gas Mixture	137
	C. Concentration Analysis	138
	D. Preparation and Filling of the Shock Tube	141
	E. Precautionary Runs	142
	F. Simultaneous Determination of Absorption and Emission from H_2O	143
	G. Determination of H_2O Emission Only	146
V.	EXPERIMENTAL RESULTS	146
	A. Conditions behind the Reflected Shock	146
	B. Spectral and Integrated Absorption Coefficients	151
	C. Estimate of Accuracy	155
VI.	DISCUSSION AND COMPARISON OF RESULTS	159
VII.	CONCLUSIONS	167
APPENDIX		
A	Radiant Flux from a Monochromator Focused in a Homogeneous, Non-Scattering, Radiating Substance of Finite Thickness	168
B	Elimination of Error in an Absolute Intensity Calibration Using an Off-Axis Spherical Concave Mirror	173
C	Effective Transmission of a Window at Near Normal Incidence with Media of Equal Indices of Refraction on Either Side	176
D	Steradiancy Outside a Homogeneous, Non-Scattering, Radiating Substance Contained between Two Parallel Partially-Reflecting Windows	179
	REFERENCES FOR PART II	182

PART I: RADIATIVE TRANSFER STUDIES AND OPACITY CALCULATIONS FOR HEATED GASES*

I. INTRODUCTION

During the last decade the scope of activity in applied science covered by the aerodynamicist has broadened enormously. The advent of new developments in space science and technology has led to the necessity of assimilating several large new scientific disciplines into the working tools of the aeronautical engineer:

1. Developments in chemical propulsion techniques have led to the introduction of large sections of classical chemical kinetics into combustion theory and propulsion development.

2. The prospect of space flight applications using low-thrust devices for interplanetary flight maneuvers has turned the attention of many aerodynamicists to basic and applied problems in magnetofluid-dynamics.

3. The two-body and many-body problems of classical mechanics, which were heretofore extensively used by astrophysicists in quantitative descriptions of planetary motion, have become important facets of optimal trajectory calculations for a variety of thrust devices.

This study concerns itself with yet another scientific discipline, which is becoming increasingly important for both the aerodynamicist and the astrodynamicist and which is no less rich in scope and com-

*This is a revised version of a paper by S. S. Penner and R. W. Patch presented at the symposium on "High Temperature in Aeronautics" in honor of Modesto Panetti, which was held at the Politecnico di Torino, Italy, during September 1962.

plexity than any of those mentioned above, namely, the spectroscopy of gases[1-3]. This subject is of great importance in the quantitative understanding of radiative transfer problems in hypersonic flight and in chemical or nuclear-powered rocket engines as well as in other types of advanced propulsion devices. The basic discipline was extensively developed by theoretical physicists during the years when quantum theory became firmly established. More recently it has served as the prime observational tool of the astrophysicists who have brought both the atomic and molecular aspects of the field and the radiative transfer applications to a high degree of development[4-6]. Nevertheless, as has always been true in applied science, the new applications in aeronautics and astronautics require new and significant extensions of all aspects of these developments[7]. In the following sections, brief consideration is given to representative topics from this field of science, some borrowed from the classical literature on opacity calculations and radiative transfer analysis, others recent developments that have been largely motivated by the extension of the fields of interest of the aerodynamicists. In view of the enormous scope and complexity of the subject, one cannot hope to do more than sketch some of the simpler but pertinent aspects of the science.

The following topics will be treated: the formulation of radiative transfer problems (Section II)[5, 6], the definition of opacities and radiation free paths for the important limiting cases of a transparent gas and an opaque gas (Section III)[4, 8], the reformulation of the

conservation equations with proper allowance for radiative energy transport (Section IV)[9-13], the coupling of radiation and convection in detached shock layers (Section V)[14], selected calculations of spectral absorption coefficients in molecular systems (Section VI), and continuum radiation in plasmas containing polyelectronic, partially or completely ionized atoms (Section VII)[15-18].

II. THE FORMULATION OF RADIATIVE TRANSFER PROBLEMS[5, 6, 19]

Consider the geometric arrangement sketched in Fig. 1. Define the spectral steradiancy B_ν on the area dA_1 at the point P as the instantaneous value of the radiant energy ϵ (in erg) incident in unit time in unit solid angle in the frequency interval between ν and $\nu + \Delta\nu$ on unit area of the projected surface normal to the direction of observation. Thus

$$B_\nu \equiv \lim \left| \frac{\Delta\epsilon}{\cos\theta' \Delta A_1 \Delta\omega_1 \Delta\nu \Delta t} \right|_{\Delta t,\, \Delta A_1,\, \Delta\omega_1,\, \Delta\nu \to 0} \tag{1}$$

where Δt is the time increment. If, at any point, B_ν is independent of the direction of the vector $\vec{L}$, the radiation is termed <u>isotropic</u> at that point. The radiation field is said to be <u>homogeneous</u> if B_ν has the same value at all points and in all directions.

In order to find the differential equation for B_ν along a ray, four processes will be considered in various combinations: spontaneous emission, absorption, induced emission, and scattering. If an atom or molecule is in an excited state, there may be a finite probability that it will radiate even if no radiation field is present. This process is

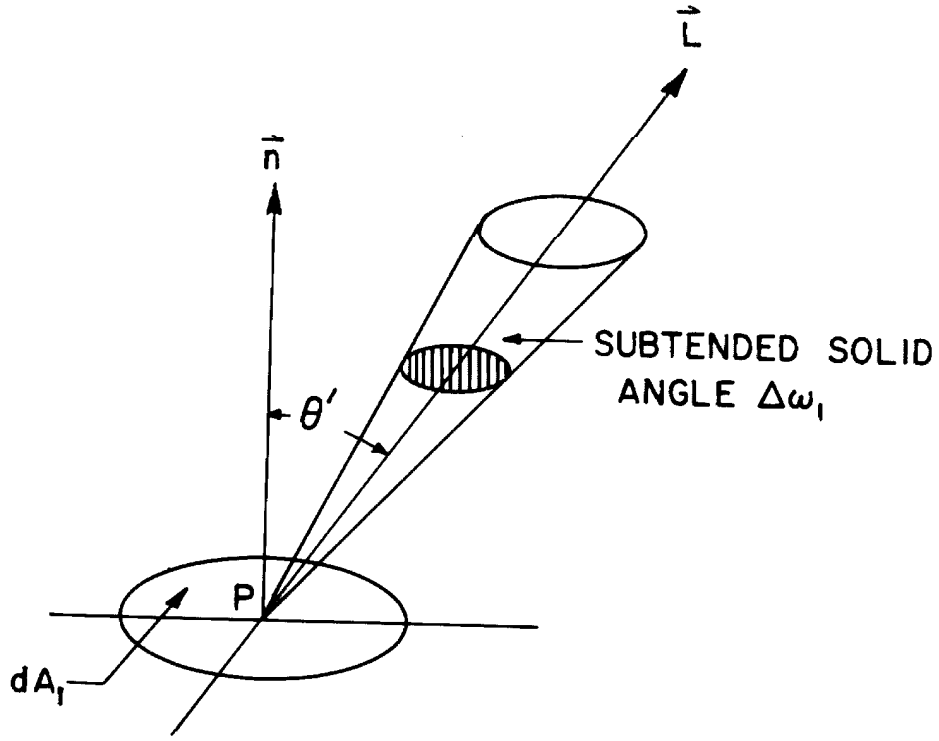

Fig. 1. Schematic diagram illustrating the symbols used in the definition of the spectral steradiancy (or specific intensity or intensity) B_ν.

known as spontaneous emission and is equally probable in all directions. If a radiation field is present, an atom or molecule may absorb a photon and end up in an excited state; this process is known as absorption. Also, if a radiation field and an excited atom or molecule are present, the radiation field may induce the excited particle to emit a photon of the same frequency in the same direction as an incident photon belonging to the field. This process is termed induced emission. The fourth process, that of scattering, occurs if a photon interacts with a particle so that the direction of the photon is changed. In the present study only scattering for which the energy of the photon is unchanged is considered.

In the following discussion the gas is assumed to be in local thermodynamic equilibrium, i.e., the occupation numbers of quantum states must form a Fermi-Dirac or Bose-Einstein equilibrium distribution, as appropriate for the particles. In the absence of radiation, these distributions are maintained by energy transfer in collisions, and it is assumed that for the cases considered the radiation field does not perturb the appropriate distribution appreciably.

A. Absorption and Induced Emission of Radiation

Consider the case where only absorption and induced emission are significant. The induced emission may be thought of as a sort of negative absorption, and its effect is included in the various absorption coefficients in this study, making them slightly smaller than if induced emission did not exist.

Appealing either to experimental observations or to quantum

mechanics, it can be shown that the rate of change of B_ν with distance is proportional to B_ν for a beam of photons propagating in a specified direction. Thus

$$\frac{dB_\nu}{dx} = - P_\nu p B_\nu = - k_\nu \rho_g B_\nu = - k_{L,\nu,T} B_\nu \qquad (2)$$

where the distance x (in cm) is measured in the direction of propagation, P_ν (in cm^{-1} atm^{-1}) is the spectral absorption coefficient per unit pressure per unit length, p (in atm) is the pressure, k_ν (in cm^2/g) is the spectral mass absorption coefficient, ρ_g (in g/cm^3) is the gas density, and $k_\nu \rho_g = k_{L,\nu,T}$ (in cm^{-1}) is the linear absorption coefficient.

B. Transfer of Radiation Without Scattering

If, in addition to absorption and induced emission, spontaneous emission is important, Eq. (2) must be replaced by the following expression

$$\frac{dB_\nu}{dx} = - k_\nu \rho_g B_\nu + \rho_g j_\nu \qquad (3)$$

where j_ν (in erg $ster^{-1}$ sec^{-1} g^{-1} per unit frequency) is called the emission coefficient but actually results only from spontaneous emission, not induced emission. For an isothermal system in thermodynamic equilibrium $dB_\nu/dx = 0$, and, therefore,

$$j_\nu = k_\nu B_\nu \equiv k_\nu B_\nu^o \qquad (4)$$

where B_ν^o is the equilibrium value of B_ν at the temperature T of

the system, i.e., $B_\nu = B_\nu^o$ corresponds to the specific intensity derived from the Planck blackbody radiation law, viz.,

$$B_\nu^o \equiv \frac{R_\nu^o}{\pi} = \frac{2h\nu^3}{c^2} \frac{1}{e^{h\nu/kT} - 1} \tag{5}$$

Here h is Planck's constant, c is the velocity of light, and k denotes the Boltzmann constant. The quantity R_ν^o is the hemispherical radiancy of a blackbody, i.e., the energy radiated per unit time in all directions from a unit area of black surface. The quantity R_ν^o is also known as the Planck function.

Combining Eqs. (3) and (4), the transfer equation takes the form

$$-\frac{1}{\rho_g k_\nu} \frac{dB_\nu}{dx} = B_\nu - B_\nu^o \tag{6}$$

C. Absorption and Isotropic Scattering Without Spontaneous Emission of Radiation

Consider a single ray passing through an elemental volume of gas. A fraction of the photons may be scattered. This scattering is said to be isotropic if there is an equal probability of a photon being scattered in one direction as in another. Assume 1) the extreme case where spontaneous emission of radiation is totally absent, and 2) the ray mentioned above is the only one incident on the element of gas. Then, if B_ν changes by dB_ν in passing through a layer, a part of dB_ν is due to scattering and the other part to absorption and induced emission. Let the former part be $\bar{\omega}_\nu dB_\nu$; then the latter is $(1 - \bar{\omega}_\nu)dB_\nu$, where $\bar{\omega}_\nu$ is called the albedo for single scattering.

It can be shown* that the emission coefficient j_ν is associated exclusively with isotropic scattering by the relation

$$j_\nu = \bar{\omega}_\nu k_\nu \oint B_\nu \frac{d\omega_1}{4\pi}$$

where the integration is to be performed over the complete solid angle. The transfer equation is now of the form

$$-\frac{1}{\rho_g k_\nu}\frac{dB_\nu}{dx} = B_\nu - \bar{\omega}_\nu \oint B_\nu \frac{d\omega_1}{4\pi} \tag{7}$$

D. Absorption and Emission of Radiation and Isotropic Scattering

In the case where spontaneous emission, induced emission, isotropic scattering, and absorption of radiation all occur, the emission coefficient becomes

$$j_\nu = \bar{\omega}_\nu k_\nu \oint B_\nu \frac{d\omega_1}{4\pi} + (1 - \bar{\omega}_\nu) k_\nu B_\nu^o$$

The transfer equation assumes the form

$$-\frac{1}{\rho_g k_\nu}\frac{dB_\nu}{dx} = B_\nu - \bar{\omega}_\nu \oint B_\nu \frac{d\omega_1}{4\pi} - (1 - \bar{\omega}_\nu) B_\nu^o \tag{8}$$

E. Radiative Energy Transfer from Gases Confined Between Two Infinite Parallel Plates[19]

The contribution of a pencil of radiation to the irradiancy or incident flux on a surface is

*Reference (6), pp. 9-13.

$$dI_\nu = \frac{d\varepsilon}{dA_1\, d\nu\, dt} = B_\nu \cos\theta'\, d\omega_1 \tag{9}$$

where the angle θ' is shown in Fig. 2. Set

$$d\omega_1 = \sin\theta'\, d\theta'\, d\phi$$

where ϕ is the azimuthal angle measured around the outward unit normal $\vec{n}$ of the upper boundary plate (see Fig. 2). Integrating Eq. (9) over all directions, the spectral radiant flux density between the bounding plates for $0 \le y \le L$ becomes

$$q_\nu = q_\nu^+ + q_\nu^- \tag{10}$$

where

$$q_\nu^+ = \int_0^{2\pi}\int_0^{\pi/2} B_\nu^+(\theta', \phi) \cos\theta' \sin\theta'\, d\theta'\, d\phi \tag{11}$$

and

$$q_\nu^- = \int_0^{2\pi}\int_{\pi/2}^{\pi} B_\nu^-(\theta', \phi) \cos\theta' \sin\theta'\, d\theta'\, d\phi \tag{12}$$

denote, respectively, the flux density in the downward $(0 < \theta' < \frac{\pi}{2})$ and upward $(\frac{\pi}{2} < \theta' < \pi)$ directions. If B_ν is independent of ϕ, the integration over ϕ may be performed immediately in Eqs. (11) and (12).

The preceding expressions constitute the starting relations for radiative transfer analysis. The excellent texts of Chandrasekhar[5] and Kourganoff[6] may be referred to for elaboration of methods and

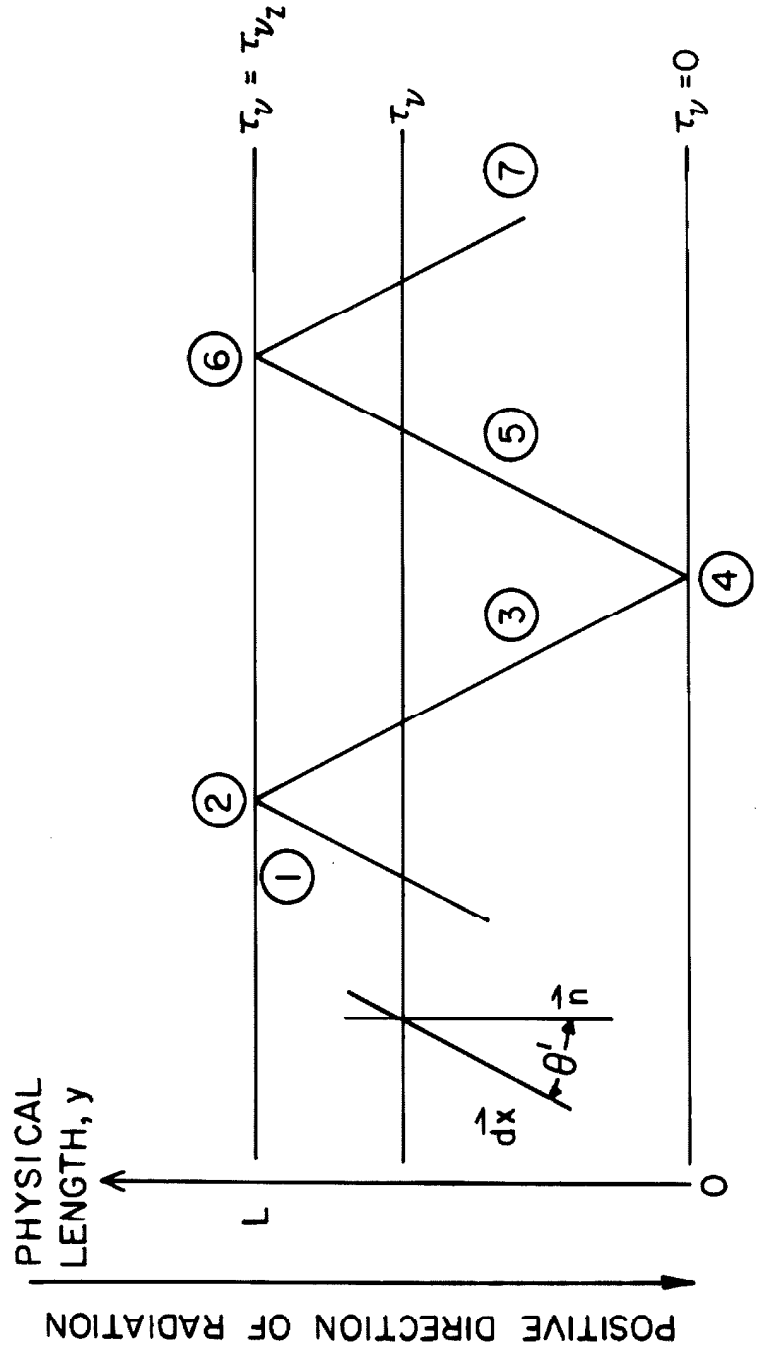

Fig. 2. Schematic diagram relevant to a derivation of the radiative transfer problem between two parallel plates when multiple reflections of rays from the bounding walls are considered (from Ref. (19)).

results in radiative transfer analysis. However, in order to provide an elementary illustration of conventional procedures, the form of q_ν^+ and q_ν^- in a one-dimensional problem without scattering will be indicated[19].

For a one-dimensional problem with local thermodynamic equilibrium and no scattering, Eq. (6) applies. Define the optical depth τ_ν measured normal to the parallel boundary planes by

$$d\tau_\nu = - \rho_g k_\nu \cos \theta' \, dx \tag{13}$$

Using Eq. (13), Eq. (6) becomes

$$\cos \theta' \frac{dB_\nu}{d\tau_\nu} = B_\nu(\tau_\nu) - B_\nu^o(\tau_\nu) \tag{14}$$

The solution of the preceding differential equation is

$$\left.\begin{aligned} B_\nu(\tau_\nu) &= C(\tau_\nu) e^{\tau_\nu/\cos \theta'} \\ C(\tau_\nu) &= C(\tau_\nu^*) - \int_{\tau_\nu^*}^{\tau_\nu} \frac{B_\nu^o(\eta)}{\cos \theta'} \, e^{-\eta/\cos \theta'} \, d\eta \end{aligned}\right\} \tag{15}$$

where τ_ν^* and $C(\tau_\nu^*)$ must be determined after imposition of suitable boundary conditions.

Neglecting reflected radiation, the intensity of radiation towards the upper wall $(\frac{\pi}{2} < \theta' < \pi)$ is determined by the boundary condition at the lower wall $C(0) = B_\nu^-(0)$ at $\tau_\nu = 0$ where $B_\nu^-(0)$ is the specific intensity in the upward direction from the lower wall (see Fig. 2). Thus

$$B_\nu^-(\tau_\nu) = \left[\int_0^{\tau_\nu} \frac{B_\nu^o(\eta)}{-\cos\theta'} e^{-\eta/\cos\theta'} d\eta + B_\nu^-(0) \right] e^{\tau_\nu/\cos\theta'} \tag{16}$$

Similarly, the intensity of radiation towards the lower wall ($0 < \theta' < \frac{\pi}{2}$) is determined by the boundary condition at the upper wall $B_\nu^+(\tau_{\nu_2}) = C(\tau_{\nu_2}) \exp(\tau_{\nu_2}/\cos\theta')$ where $B_\nu^+(\tau_{\nu_2})$ is the specific intensity in the downward direction from the upper wall. Thus

$$B_\nu^+(\tau_\nu) = B_\nu^+(\tau_{\nu_2}) e^{-(\tau_{\nu_2}-\tau_\nu)/\cos\theta'} + \int_{\tau_{\nu_2}}^{\tau_\nu} \frac{B_\nu^o(\eta)}{-\cos\theta'} e^{-(\eta-\tau_\nu)/\cos\theta'} d\eta \tag{17}$$

Next Eqs. (16) and (17) are used in order to compute the corresponding spectral radiant flux densities. Thus it is found [compare Eqs. (11) and (12)] that

$$q_\nu^- = -2\pi \int_0^1 \int_0^{\tau_\nu} B_\nu^o(\eta) e^{(\eta-\tau_\nu)/\mu'} d\eta\, d\mu' - 2\pi B_\nu^-(0) \int_0^1 \mu' e^{-\tau_\nu/\mu'} d\mu' \tag{18}$$

and

$$q_\nu^+ = 2\pi \int_0^1 \int_{\tau_\nu}^{\tau_{\nu_2}} B_\nu^o(\eta) e^{-(\eta-\tau_\nu)/\mu'} d\eta\, d\mu' + 2\pi B_\nu^+(\tau_{\nu_2}) \int_0^1 \mu' e^{-(\tau_{\nu_2}-\tau_\nu)/\mu'} d\mu' \tag{19}$$

Kourganoff[6] has tabulated the function

$$E_n(\eta) \equiv \int_0^1 \mu'^{n-2} e^{-\eta/\mu'} d\mu' \tag{20}$$

In terms of the function $E_n(\eta)$, Eqs. (18) and (19) become

$$q_\nu^-(\tau_\nu) = -2\pi\int_0^{\tau_\nu} B_\nu^o(\eta)E_2(\tau_\nu-\eta)\,d\eta - 2\pi B_\nu^-(0)E_3(\tau_\nu) \tag{21}$$

and

$$q_\nu^+(\tau_\nu) = 2\pi\int_{\tau_\nu}^{\tau_{\nu_2}} B_\nu^o(\eta)E_2(\eta-\tau_\nu)\,d\eta + 2\pi B_\nu^+(\tau_{\nu_2})E_3(\tau_{\nu_2}-\tau_\nu) \tag{22}$$

The net spectral flux in the downward direction is evidently equal to the sum of $q_\nu^-(\tau_\nu)$ and $q_\nu^+(\tau_\nu)$. In the absence of walls $B_\nu^-(0) = B_\nu^+(\tau_{\nu_2}) = 0$, and the flux equations reduce to classical forms given by Milne[5, 6]. Further analysis of the present problem can be carried out simply only for the case of spectrally resolved radiation or for grey radiation[19].

F. Radiative Energy Transfer to the Nose Cone of a Reentry Vehicle

A blunt, reentering nose cone of a reentry missile forms a detached shock wave ahead of it. Under conditions where local thermodynamic equilibrium is prevalent, the air between the detached shock wave and the stagnation point of the nose cone is approximately homogeneous and may be approximated, to first order, by the uniform, flat layer of gas of constant thickness L assumed in deriving the equations of Section IIE.

To solve the radiative energy transfer problem for a nose cone, consider transfer in one direction only (say, the positive direction) with $B_\nu^+(\tau_{\nu_2}) = 0$, i.e., without emission from the shock front itself, which is assumed to be infinitely thin. Thus the flux density at the nose cone surface ($\tau_\nu = 0$) is seen to be

$$q_\nu^+(0) = 2\pi \int_0^{\tau_{\nu_2}} B_\nu^o(\eta) E_2(\eta)\, d\eta$$

from Eq. (22). But, for uniform gases, $B_\nu^o(\eta) = B_\nu^o$ is a constant and, therefore,

$$q_\nu^+(0) = 2\pi B_\nu^o \int_0^1 \int_0^{\tau_{\nu_2}} e^{-\eta/\mu'}\, d\eta\, d\mu'$$

$$= 2\pi B_\nu^o \int_0^1 \left(1 - e^{-\tau_{\nu_2}/\mu'}\right) \mu'\, d\mu'$$

$$= 2\pi B_\nu^o \int_0^{\pi/2} \left(1 - e^{-k_\nu \rho_g y/\cos\theta'}\right) \cos\theta' \sin\theta'\, d\theta'$$

$$q_\nu^+(0) = B_\nu^o \int_0^{2\pi} \left(1 - e^{-k_\nu \rho_g y \sec\theta'}\right) \cos\theta'\, d\Omega \qquad (23)$$

where $d\Omega$ denotes an element of the solid angle. The last form of the integrand in Eq. (23) will be recognized immediately as the spectral emissivity for uniformly distributed gases with linear absorption coefficient $k_\nu \rho_g$, contained by walls a distance y apart, and referring to propagation in the direction θ' relative to the normal distance y.

For a <u>transparent</u> gas layer, the exponential may be expanded

$$e^{-\tau_{\nu_2}/\mu'} = 1 - \frac{\tau_{\nu_2}}{\mu'} + \ldots$$

To first order, only the first two terms are retained and, therefore,

$$q_\nu^+(0) \approx 2\pi B_\nu^o \int_0^1 \tau_{\nu_2} d\mu' = 2\pi B_\nu^o k_\nu \rho_g L = k_\nu \rho_g 2L R_\nu^o \tag{24}$$

It is apparent that this is the well-known result that the effective geometric length that is to be used in radiative transfer calculations for uniformly distributed, transparent gases bounded by infinite parallel planes a distance L apart is $2L$.

If the spectral absorptivity of the wall is a_ν, then the <u>total</u> radiant flux density W absorbed by the wall may be obtained from Eq. (24) by integrating $a_\nu q_\nu^+(0)$ over all frequencies, viz.,

$$W = 2L\rho_g \int_0^\infty a_\nu k_\nu R_\nu^o \, d\nu = 2Lp \int_0^\infty a_\omega P_\omega R_\omega^o(\tau_g) \, d\omega$$

$$= 2Lp \int_0^\infty a_\omega P_\omega \sigma T_g^4 \, \mathfrak{F}(\omega) \, d\omega \tag{25}$$

where $\omega = \nu/c$ is the wave number, P_ω is the spectral absorption coefficient (cm^{-1} atm^{-1}), $R_\omega^o(T_g)$ is the Planck function at the temperature T_g at ω, T_g is the temperature of the uniformly distributed gases in front of the nose cone, and $\mathfrak{F}(\omega) \, d\omega$ is the fractional energy of a blackbody radiator contained in the wave number range between ω and $\omega + d\omega$ if σ represents the Stefan-Boltzmann constant. The incident integrated flux F_R is obtained from Eq. (25) by setting a_ω equal to unity, viz.,

$$F_R = 2Lp \int_0^\infty P_\omega \sigma T_g^4 \, \mathfrak{F}(\omega) \, d\omega$$

The effective engineering emissivity of the shocked gases may be defined as

$$\epsilon_{eff} \equiv \frac{F_R}{\sigma T_g^4} = 2Lp \int_0^\infty P_\omega \mathfrak{F}(\omega)\, d\omega \tag{26}$$

It is of interest* to compare the incident radiant flux, viz.,

$$F_R = 2L\rho_g \sigma T_g^4 \int_0^\infty k_\omega \mathfrak{F}(\omega)\, d\omega$$

with the convective energy transport to a reentry body. The shock stand-off distance L turns out to be a linear function of the nose radius R and is also proportional to the density ratio across the shock front. The spectral absorption coefficient k_ω ($cm^2 g^{-1}$) depends only weakly on density but varies strongly with the gas stagnation temperature. A fit to the available emissivity data for heated air shows[20] that

$$F_R \sim \rho^{3/2} R U^{10}$$

where ρ is the ambient air density and U denotes the missile velocity. On the other hand, the convective heat transfer to a reentry body is given[20] by the approximate relation

$$F_c \sim \left(\frac{\rho}{R}\right)^{1/2} U^3$$

*In the following calculations, the radiant energy exchange is treated as a perturbation on the flow field calculations. This approximation is not justified for very large reentry velocities (compare Section IV B).

Hence the ratio of radiative to convective heat transfer becomes

$$\frac{F_R}{F_c} \sim \rho R^{3/2} U^7$$

i.e., radiative energy transfer becomes relatively much more important as the missile velocity increases and is also favored by high air density and a large nose radius.

III. PLANCK AND ROSSELAND MEAN FREE PATHS[4, 8]

Equation (6) may be written in the form

$$\frac{dB_\nu}{dx} = k_{L,\nu,T}\,(B_\nu^o - B_\nu)$$

or, from Fig. 2

$$\cos\theta' \frac{dB_\nu}{dy} = k_{L,\nu,T}(B_\nu^o - B_\nu) \qquad (6a)$$

where $k_{L,\nu,T} = \rho_g k_\nu$ is the spectral absorption coefficient per unit length, θ' is the angle between the normal to the slab and the direction of propagation in which an incremental length has been denoted by dx. In radiative transfer analysis the Planck and Rosseland mean absorption coefficients are often employed since they represent useful approximations for optically thin (i.e., transparent) gases and for relatively opaque gases, respectively.

A. The Planck Mean Absorption Coefficient[4, 8]

The Planck mean absorption coefficient is useful for optically thin gases for which

$$k_{L,\nu,T}\Delta y \ll 1 \quad \text{and} \quad B_\nu \ll B_\nu^o \tag{27}$$

if Δy denotes a macroscopic distance, such as L in Fig. 2, characteristic of the problem. If the gas is homogeneous, the change in steradiancy in a distance $\Delta y/\cos\theta'$ along any ray is

$$\Delta B_\nu \approx k_{L,\nu,T} B_\nu^o \frac{\Delta y}{\cos\theta'}$$

Consider a slab of thickness Δy with no radiation incident on either face from the outside. In view of Eq. (25), the radiant flux density F_R passing through the bounding planes is

$$F_{\Delta y} = 2\pi\Delta y \int_0^\infty k_{L,\nu,T}\, B_\nu^o \, d\nu$$

Consequently, the effective emissivity ϵ_{eff} is

$$\epsilon_{eff} = \frac{2\pi\Delta y \int_0^\infty k_{L,\nu,T} B_\nu^o \, d\nu}{\sigma T^4}$$

The effective emissivity ϵ_{eff} divided by twice the slab thickness is defined as the reciprocal of the Planck mean free path $\overline{\lambda}_{P\ell}$ and as equal to the Planck mean absorption coefficient $\overline{k}_{L,P\ell}$, viz.,

$$\frac{1}{\overline{\lambda}_{P\ell}} \equiv \overline{k}_{L,\,P\ell} \equiv \frac{\epsilon_{eff}}{2\Delta y} = \frac{\pi \int_0^\infty k_{L,\nu,\,T} B_\nu^o \, d\nu}{\sigma T^4} \tag{28}$$

Thus, in the transparent gas approximation, the Planck mean absorption coefficient equals the usual definition of the isothermal engineering emissivity[7] divided by the appropriate mean beam length for an infinite slab of thickness Δy.

B. The Rosseland Mean Absorption Coefficient[4, 8]

The origin of the Rosseland mean absorption coefficient as the corrent "local" value of the absorption coefficient for relatively opaque gases may be understood on the basis of the following considerations.

For steady state in each volume element of gas, the emitted and absorbed radiant energies must be exactly equal. Consider the arbitrary volume of gas V in Fig. 3. The amount of energy per unit time that traverses the infinitesimal element of surface dA is

$$B_\nu \cos\theta \, dA \, d\Omega \, d\nu$$

where Ω is the solid angle. If the volume is small enough that it may be considered homogeneous and $k_\nu \rho \ell \ll 1$, then the net amount of energy per unit time absorbed as a result of absorption and induced emission is

$$k_\nu \rho \ell \, B_\nu \cos\theta \, dA \, d\Omega \, d\nu$$

where k_ν is the absorption coefficient in, say, cm^2/g.

In Fig. 3 the cylindrical volume contains a mass $dM = \rho \ell \cos\theta \, dA$,

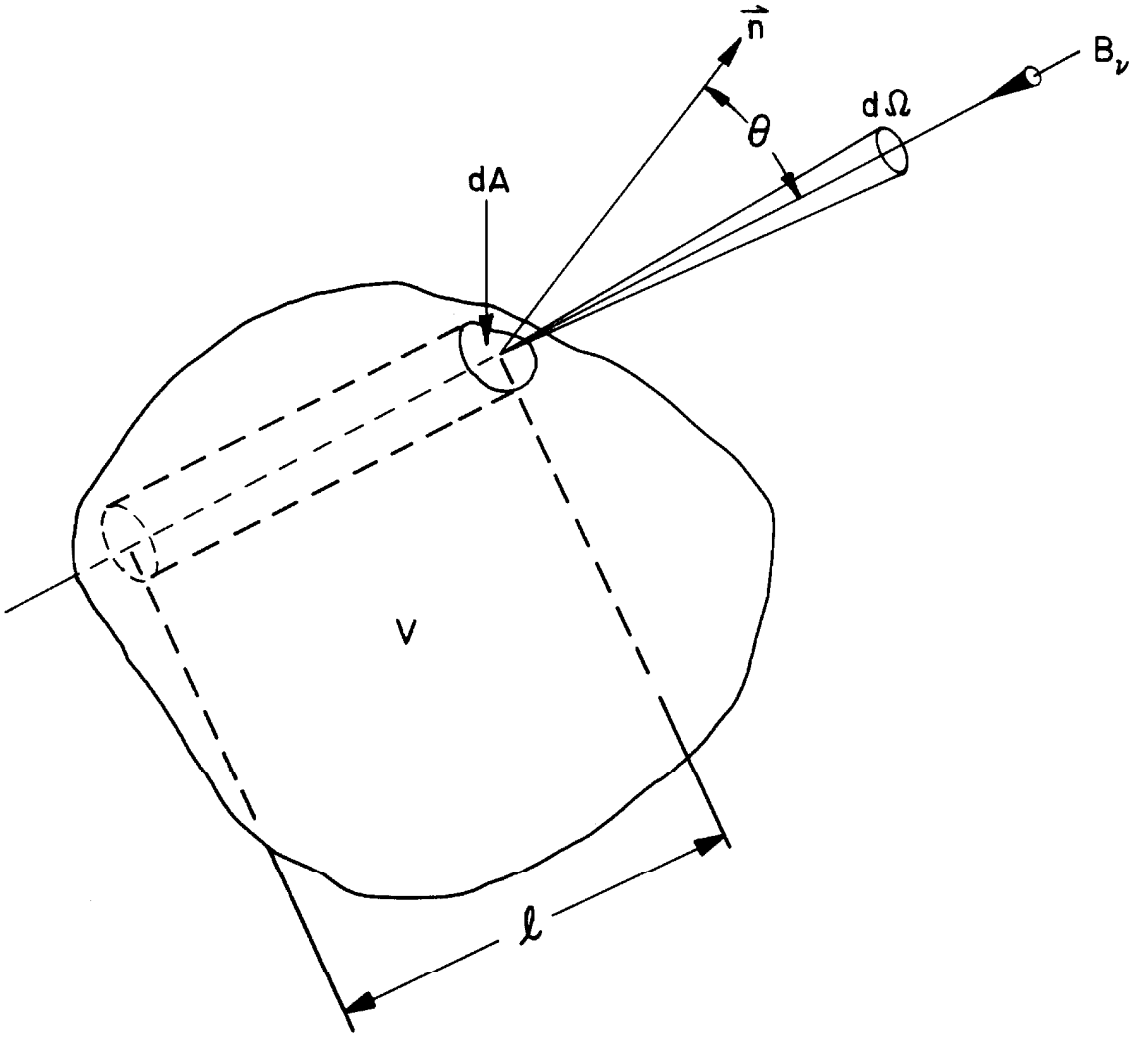

Fig. 3. An arbitrary volume of gas V used in relating J_ν and B_ν^o. All surfaces are assumed to be convex, and the volume is small enough that it can be considered to be homogeneous. The vector $\vec{n}$ is the unit normal to dA.

so the net amount of energy absorbed per unit time becomes

$$k_\nu B_\nu \, dM \, d\Omega \, d\nu$$

Integrating over the volume V and all solid angles, the net energy absorbed per unit mass per unit time is

$$k_\nu \, d\nu \oint B_\nu \, d\Omega$$

Equating the net energy absorbed and the energy lost by spontaneous emission yields

$$k_\nu d\nu \oint B_\nu \, d\Omega = 4\pi \, j_\nu \, d\nu \tag{29}$$

Combining Eqs. (4) and (29),

$$B_\nu^o = \oint B_\nu \, \frac{d\Omega}{4\pi}$$

Define a mean steradiancy J_ν by

$$J_\nu \equiv \oint B_\nu \, \frac{d\Omega}{4\pi} \tag{30}$$

Thus

$$B_\nu^o = J_\nu \tag{31}$$

The quantity J_ν is one of a set of mean values introduced by Eddington[8]. The preceding relation is often referred to as a statement of the continuity equation for radiative transfer in a steady state system.

Again following Eddington[8], it is convenient to define the

following weighted mean values of B_ν:

$$H_\nu \equiv \oint B_\nu \cos\theta' \frac{d\Omega}{4\pi} \tag{32}$$

and

$$K_\nu \equiv \oint B_\nu \cos^2\theta' \frac{d\Omega}{4\pi} \tag{33}$$

Let y be the coordinate parallel to the temperature gradient, x be the distance along any ray, and θ be the angle between a ray and the y axis. Then

$$dy = \cos\theta \, dx$$

Transforming Eq. (6) from x coordinate to y coordinate, multiplying by $d\Omega/4\pi$, and integrating over all solid angles gives

$$-\frac{1}{\rho_g k_\nu} \frac{dH_\nu}{dy} = 0 \tag{34}$$

Similarly, multiplying Eq. (6) by $d\Omega \cos\theta/4\pi$ and integrating over all solid angles gives

$$-\frac{1}{\rho_g k_\nu} \frac{dK_\nu}{dy} = H_\nu \tag{35}$$

Furthermore, since the value of $\cos^2\theta'$ averaged over all solid angles is 1/3, it is clear that for optically rather opaque systems with relatively small temperature gradients for which B_ν is not a strongly varying function of direction,

$$K_\nu \approx \frac{1}{3} J_\nu = \frac{1}{3} B_\nu^o \tag{36}$$

To facilitate finding the appropriate mean absorption coefficient for computing the integrated radiant flux density F_R, let

$$H \equiv \int_0^\infty H_\nu \, d\nu \equiv \frac{F_R}{4\pi} \tag{37}$$

and

$$K \equiv \int_0^\infty K_\nu \, d\nu \tag{38}$$

Integrating Eq. (35) over all frequencies gives

$$-\int_0^\infty \frac{1}{\rho_g k_\nu} \frac{dK_\nu}{dy} \, d\nu = H$$

Or, equivalently,

$$-\int_0^\infty \frac{1}{k_{L,\nu,T}} \frac{dK_\nu}{dy} \, d\nu = H \tag{39}$$

Let a mean absorption coefficient $\bar{k}_{L,Ro}$ be defined by the relation

$$\frac{1}{\bar{k}_{L,Ro}} \frac{dK}{dy} \equiv \int_0^\infty \frac{1}{k_{L,\nu,T}} \frac{dK_\nu}{dy} \, d\nu \tag{40}$$

Thus,

$$-\frac{1}{\bar{k}_{L,Ro}} \frac{dK}{dy} = H = \frac{F_R}{4\pi} \tag{41}$$

From Eq. (36) it follows that for optically rather opaque systems with small temperature gradients,

$$K \approx \frac{1}{3} B^{o} \tag{42}$$

where

$$B^{o} = \int_{0}^{\infty} B_{\nu}^{o} \, d\nu$$

Combining Eqs. (36) and (42) with Eq. (40),

$$\bar{k}_{L, Ro} = \frac{\int_{0}^{\infty} \frac{dB_{\nu}^{o}}{dy} \, d\nu}{\int_{0}^{\infty} \frac{1}{k_{L, \nu, T}} \frac{dB_{\nu}^{o}}{dy} \, d\nu} = \frac{\int_{0}^{\infty} \frac{dB_{\nu}^{o}}{dT} \, d\nu}{\int_{0}^{\infty} \frac{1}{k_{L, \nu, T}} \frac{dB_{\nu}^{o}}{dT} \, d\nu} \tag{43}$$

where the numerator and denominator in the last relation have both been multiplied by the rate of change of slab thickness with temperature (dy/dT). The mean $\bar{k}_{L, Ro}$ is known as the Rosseland mean absorption coefficient, and its reciprocal is known as the Rosseland mean free path.

The usefulness of $\bar{k}_{L, Ro}$ becomes apparent when Eqs. (41) and (42) are combined.*

$$F_{R} = - \frac{4\pi}{3\bar{k}_{L, Ro}} \frac{dB^{o}}{dy} \tag{44}$$

or, in Gibbs' vector notation,

---

*Eq. (44) is characteristic of energy or mass transport processes controlled by diffusion of energy or mass. This category of physical processes may be referred to collectively as percolative phenomena.

$$\vec{F}_R = - \frac{4\pi}{3\bar{k}_{L,\,Ro}} \nabla B^o \tag{45}$$

where $\vec{F}_R$ is the radiant flux density vector. Recalling the assumptions made in deriving Eq. (44), it is clear that, for Eq. (44) to be valid, B^o_ν must not change appreciably in one photon mean free path for all frequencies of importance.

The quantity $\bar{k}_{L,\,Ro}/\rho_g$ may be referred to as the Rosseland mean opacity or, more simply, as the opacity. It is interesting to note that in the diffusion approximation the radiant flux decreases as the opacity increases, i.e., the radiant energy tends to be trapped locally. There are relatively few engineering problems at moderate temperatures in which the diffusion approximation is applicable.

IV. THE CONSERVATION EQUATIONS WITH RADIANT ENERGY TRANSPORT

The conservation equations for reacting, multicomponent gas mixtures without radiant energy transport were derived by Chapman and Cowling[9] using kinetic theory and by Truesdell[10] and Nachbar, Williams, and Penner[11] using continuum theory. The equivalence of the results derived by these different methods has been stressed by Nachbar *et al.*[11]. A similar situation prevails for a single-component gas with radiant energy transfer. Thomas[12] treated both the gas and the radiation as continua, whereas Simon[13] gave somewhat more general derivations treating both the gas and the radiation as discrete particles.

It is shown below that the results of Nachbar *et al.*[11] and of

Simon[13] may be combined to give the conservation equations for a reacting, multicomponent gas mixture with radiant energy transfer. The momentum and energy equations are given both for an optically thin gas and for a gas where the diffusion approximation for radiant energy transfer is applicable. In addition, all the conservation equations are nondimensionalized so that one can ascertain which terms need be retained for a particular problem. Throughout, six assumptions are made:

1. There are no body forces.
2. There is no ionization.
3. There is no scattering of thermal radiation.
4. The mass-averaged velocity of the gas (excluding the photons) is much less than the velocity of light.
5. No nuclear reactions take place.
6. The gas is in local thermodynamic equilibrium.

All relations will be derived in Cartesian coordinates using the summation convention[21]. The text by Aris[21] is helpful if other coordinate systems are needed.

A. Species Conservation Equations

The continuity equation for each species of a reacting, multicomponent gas mixture is[11]

$$w_k = \frac{\partial(\rho Y_k)}{\partial t} + \frac{\partial(\rho Y_k v_{k,i})}{\partial x_i} \tag{46}$$

where w_k is the net rate of production of mass of species k per

unit volume, ρ is the total gas density, Y_k is the mass fraction of species k, $v_{k,i}$ is the ith component of the velocity of species k with respect to the coordinate system, t is time, and x_i is the ith Cartesian coordinate. This equation is not altered by thermal radiation, provided w_k is understood to include the production of species k by photochemical reactions as well as by conventional chemical reactions.

To nondimensionalize Eq. (46) for application to a specific problem, let L be a length characteristic of the problem (such as the detachment distance of a shock wave ahead of a bluff body). Let t_s be a time characteristic of the problem (such as the time for free stream density to change by a factor e during atmospheric entry by a body). Similarly, select values of ρ, Y_k, and w_k characteristic of the problem and denote them with a subscript s. Select a characteristic velocity U_s. Let

$$\rho \equiv \rho_s \rho^* \tag{47}$$

$$Y_k \equiv Y_{ks} Y_k^* \tag{48}$$

$$v_{k,i} \equiv U_s v_{k,i}^* \tag{49}$$

$$w_k \equiv w_{ks} w_k^* \tag{50}$$

$$t \equiv t_s t^* \tag{51}$$

$$x_i \equiv L x_i^* \tag{52}$$

where the comma between subscripts has been omitted except to separate indices from other subscripts. The quantities with superscript * are assumed to be of order one[†] and are nondimensional.

Using Eqs. (47) - (52) and multiplying Eq. (46) by $L/U_s\rho_s Y_{ks}$ yields

$$\frac{Lw_{ks}}{U_s\rho_s Y_{ks}} w_k^* = \frac{L}{U_s t_s} \left(\frac{\partial(\rho Y_k)}{\partial t}\right)^* + \left(\frac{\partial(\rho Y_k v_{k,i})}{\partial x_i}\right)^* \tag{53}$$

where * after a parenthesis indicates that all quantities inside the pair of parentheses are starred.

The dimensionless ratio called the Strouhal Number S is defined by

$$S \equiv \frac{L}{U_s t_s} \tag{54}$$

Damköhler's first similarity group, which is the ratio of the convection time to the characteristic chemical time, is defined by

$$D_{Ik} \equiv \frac{Lw_{ks}}{U_s\rho_s Y_{ks}} \tag{55}$$

Consequently, Eq. (53) becomes

$$D_{Ik} w_k^* = S \left(\frac{\partial(\rho Y_k)}{\partial t}\right)^* + \left(\frac{\partial(\rho Y_k v_{k,i})}{\partial x_i}\right)^* \tag{56}$$

Another useful form of Eq. (46) can be obtained by first defining the diffusion velocity $V_{k,i}$ of species k by

[†] In general this would not be true for all $v_{k,i}^*$ and x_i^* in a boundary layer.

$$v_{k,i} \equiv v_i + V_{k,i} \tag{57}$$

where v_i is the mass-weighted average velocity of the mixture. In addition, it is necessary to define the Euler total time derivative† by

$$\frac{D}{Dt} \equiv \frac{\partial}{\partial t} + v_j \frac{\partial}{\partial x_j} \tag{58}$$

Thus Eq. (46) becomes

$$\frac{D(\rho Y_k)}{Dt} = w_k - V_{k,i} \frac{\partial(\rho Y_k)}{\partial x_i} - \rho Y_k \frac{\partial v_{k,i}}{\partial x_i} \tag{59}$$

B. Over-all Continuity Equation

The over-all continuity equation is obtained by summing Eq. (46) over all species. Noting that

$$\sum_k w_k = 0 \tag{60}$$

it follows from Eq. (46) that

$$\frac{\partial(\rho v_i)}{\partial x_i} = - \frac{\partial \rho}{\partial t} \tag{61}$$

In nondimensional form Eq. (61) becomes

$$\left(\frac{\partial(\rho v_i)}{\partial x_i} \right)^* = - S \left(\frac{\partial \rho}{\partial t} \right)^* \tag{62}$$

† Also known as material derivative, convected derivative, or convective derivative because it gives the rate of change of a quantity as a particle moving with the mass-weighted average velocity of the fluid is followed.

An alternate form of Eq. (61) is

$$\frac{D\rho}{Dt} = - \rho \frac{\partial v_i}{\partial x_i} \tag{63}$$

C. Momentum Equation

The momentum equation for a gas in the presence of radiation was derived by Simon[13]. Before writing it down, a few quantities should be defined. Let $F_{R,i}$ be the ith component of radiant flux density in, say, erg/cm^2 sec given by[13]

$$F_{R,i} = \int_0^\infty \oint B_\nu \ell_i \, d\Omega \, d\nu \tag{64}$$

where ℓ_i is the direction cosine between the center of the increment of solid angle $d\Omega$ and axis i.

The stress tensor $\mathcal{T}_{ij}$ (which differs in sign from Simon's P_O^{ij}) gives the external force $\vec{\xi}$ per unit area on the surface of a volume moving with the gas due only to gas pressure and gas shear forces (not radiation)

$$\xi_i = \mathcal{T}_{ij} n_j \tag{65}$$

where ξ_i is the ith component of $\vec{\xi}$, and n_j is the jth component of a unit outward normal from the surface. The radiation stress tensor $\mathcal{T}_{R,ij}$ (which differs in sign from Simon's P_R^{ij}) gives the external force $\vec{\xi}_R$ per unit area on a volume fixed with respect to the coordinates due only to radiation pressure and shear forces.

$$\xi_{R,i} = \mathrm{J}_{R,ij} n_j \tag{66}$$

From Ref. (13)

$$\mathrm{J}_{R,ij} = -\frac{1}{c}\int_0^\infty \oint B_\nu \ell_i \ell_j \, d\Omega \, d\nu \tag{67}$$

The momentum equation therefore becomes[13]

$$\frac{\partial(\rho v_i)}{\partial t} + \frac{\partial}{\partial x_j}(\rho v_i v_j - \mathrm{J}_{ij} - \mathrm{J}_{R,ij}) + \frac{1}{c^2}\frac{\partial F_{R,i}}{\partial t} = 0 \tag{68}$$

To nondimensionalize Eq. (68), let

$$\mathrm{J}_{ij} \equiv -p\delta_{ij} + \mathrm{J}_{v,ij} \tag{69}$$

where p is gas pressure, and $\mathrm{J}_{v,ij}$ is known as the viscous stress tensor. Also let

$$v_i \equiv U_s v_i^* \tag{70}$$

$$p^* \equiv \frac{p - p_s}{\rho_s U_s^2} \tag{71}$$

$$\mathrm{J}_{v,ij} \equiv \frac{\mu_s U_s}{L}\mathrm{J}^*_{v,ij} \tag{72}$$

where quantities with subscript s are characteristic values for the problem, and μ_s is the characteristic dynamic viscosity of the gas. In addition, for a gas with $\bar{k}_{LP\ell} L \leq 1$ and little external radiation incident on it, let

$$\mathcal{J}_{R,ij} \equiv \frac{R_s^o \bar{k}_{LP\ell} L}{c} \mathcal{J}^*_{R,ij} \tag{73}$$

$$F_{R,i} \equiv R_s^o \bar{k}_{LP\ell} L F^*_{R,i} \tag{74}$$

where R_s^o is the Planck blackbody function at some characteristic temperature T_s of the problem. In Eqs. (70) - (74) it is assumed that all starred quantities are of order one.

If quantities from Eqs. (69) - (74), etc. are substituted into Eq. (68) and the resulting equation multiplied by $L/\rho_s U_s^2$ then

$$S\left(\frac{\partial(\rho v_i)}{\partial t}\right)^* + \left(\frac{\partial(\rho v_i v_j)}{\partial x_j}\right)^* + \left(\frac{\partial p}{\partial x_i}\right)^* - \frac{\mu_s}{L\rho_s U_s}\left(\frac{\partial \mathcal{J}_{v,ij}}{\partial x_j}\right)^*$$
$$- \frac{LR_s^o \bar{k}_{LP\ell}}{c\rho_s U_s^2}\left(\frac{\partial \mathcal{J}_{R,ij}}{\partial x_j}\right)^* + S\frac{LR_s^o \bar{k}_{LP\ell}}{c^2 \rho_s U_s}\left(\frac{\partial F_{R,i}}{\partial t}\right)^* = 0 \tag{75}$$

Define a dimensionless ratio

$$G \equiv \frac{R_s^o \bar{k}_{LP\ell} L}{c\rho_s U_s^2} \tag{76}$$

which is proportional to the ratio of radiant energy to kinetic energy of the gas. Also, let

$$\mathfrak{B} = \frac{U_s}{c} \tag{77}$$

$$\mathfrak{R} = \frac{\rho_s U_s L}{\mu_s} \tag{78}$$

where $\mathfrak{R}$ is the Reynolds number of the gas. Substituting dimension-

less ratios from Eqs. (76) - (78) into Eq. (75) gives

$$S\left(\frac{\partial(\rho v_i)}{\partial t}\right)^* + \left(\frac{\partial(\rho v_i v_j)}{\partial x_j}\right)^* + \left(\frac{\partial p}{\partial x_i}\right)^* - \frac{1}{\mathcal{R}}\left(\frac{\partial \tau_{v,ij}}{\partial x_j}\right)^* - G\left(\frac{\partial \tau_{R,ij}}{\partial x_j}\right)^* = 0 \tag{79}$$

where the term containing $F^*_{R,i}$ was dropped because it also contained $\mathcal{R}$. Due to assumptions made in Eqs. (73) and (74), Eq. (79) is only valid for $\bar{k}_{LP\ell} L \leq 1$.

In cases where $\bar{k}_{LRo} L >> 1$, the diffusion approximation is applicable if B^o_ν does not change appreciably in one photon mean free path for all frequencies of importance. The diffusion approximation to the momentum equation has been worked out[13], but before introducing it some new quantities must be brought in. Let μ_R be radiation viscosity defined by[13]

$$\mu_R = \frac{16\sigma T^4}{15\,\bar{k}_{LRo} c^2} \tag{80}$$

There are two possible definitions of the radiation pressure in cases where the diffusion approximation is applicable. In this study let[13]

$$P_R \equiv \frac{4R^o}{3c} \tag{81}$$

The radiation stress tensor may be written

$$\tau_{R,ij} \equiv -P_R \delta_{ij} + \tau_{Rv,ij} \tag{82}$$

where $\Im_{Rv,ij}$ is the viscous radiation stress tensor for a volume fixed with respect to the coordinates. It can be shown from Ref. (13) that

$$\Im_{Rv,ij} = \mu_R \left(\frac{\partial v_\ell}{\partial x_\ell} \delta_{ij} + \frac{\partial v_i}{\partial x_j} + \frac{\partial v_j}{\partial x_i} \right)$$

$$+ \frac{\zeta_R}{c^2} \left(\frac{\partial T}{\partial x_i} v_j + \frac{\partial T}{\partial x_j} v_i \right) + \frac{5\mu_R}{c^2} \left(\frac{Dv_i}{Dt} v_j + \frac{Dv_j}{Dt} v_i \right) \qquad (83)$$

where ζ_R is the radiation thermal conductivity given by

$$\zeta_R \equiv \frac{16 \sigma T^3}{3 \overline{k}_{LRo}} \qquad (84)$$

For $\beta \ll 1$ Eq. (83) becomes

$$\Im_{Rv,ij} = \mu_R \left(\frac{\partial v_\ell}{\partial x_\ell} \delta_{ij} + \frac{\partial v_i}{\partial x_j} + \frac{\partial v_j}{\partial x_i} \right) \qquad (85)$$

From relations in Ref. (13) it can be shown that

$$F_{R,i} = - \zeta_R \frac{\partial T}{\partial x_i} + 4P_R v_i$$

$$- \mu_R \left(6 v_j \frac{\partial v_i}{\partial x_j} + 5 \frac{\partial v_i}{\partial t} + 6 v_i \frac{\partial v_\ell}{\partial x_\ell} + v_j \frac{\partial v_j}{\partial x_i} \right) \qquad (86)$$

Equation (68) becomes

$$\frac{\partial(\rho v_i)}{\partial t} + \frac{\partial(\rho v_i v_j)}{\partial x_j} + \frac{\partial p}{\partial x_i} + \frac{\partial P_R}{\partial x_i} - \frac{\partial \tau_{v,ij}}{\partial x_j} - \frac{\partial \tau_{Rv,ij}}{\partial x_j}$$

$$- \frac{1}{c^2} \frac{\partial}{\partial t} \left[\zeta_R \frac{\partial T}{\partial x_i} - 4P_R v_i + \mu_R \left(6v_j \frac{\partial v_i}{\partial x_j} + 5 \frac{\partial v_i}{\partial t} + 6v_i \frac{\partial v_\ell}{\partial x_\ell} \right.\right.$$

$$\left.\left. + v_j \frac{\partial v_j}{\partial x_i} \right) \right] = 0 \qquad (87)$$

The procedure for nondimensionalizing Eq. (87) is the same as before. Let

$$\tau_{Rv,ij} \equiv \frac{\mu_{Rs} U_s}{L} \tau^*_{Rv,ij} \qquad (88)$$

$$\mu_R \equiv \mu_{Rs} \mu^*_R \qquad (89)$$

$$\zeta_R \equiv \zeta_{Rs} \zeta^*_R \qquad (90)$$

$$P_R \equiv \frac{R^o_s}{c} P^*_R \qquad (91)$$

Define a radiation Reynolds number by

$$\mathcal{R}_R \equiv \frac{\rho_s U_s L}{\mu_{Rs}} \qquad (92)$$

Let

$$\mathcal{C} \equiv \frac{R^o_s}{c \rho_s U_s^2} \qquad (93)$$

where the dimensionless ratio $\mathcal{C}$ is proportional to the ratio of the

radiation energy density to the kinetic energy of the gas.

Substituting the quantities defined by Eqs. (88) - (91), etc. into Eq. (87), multiplying by $L/\rho_s U_s^2$, making use of Eqs. (92) - (93), etc. and dropping terms containing $\mathcal{B}^2$ (there are none containing merely $\mathcal{B}$) gives

$$S\left(\frac{\partial(\rho v_i)}{\partial t}\right)^* + \left(\frac{\partial(\rho v_i v_j)}{\partial x_j}\right)^* + \left(\frac{\partial p}{\partial x_i}\right)^* + \mathcal{C}\left(\frac{\partial P_R}{\partial x_i}\right)^*$$

$$- \frac{1}{\mathcal{R}}\left(\frac{\partial \mathcal{J}_{v,ij}}{\partial x_j}\right)^* - \frac{1}{\mathcal{R}_R}\left(\frac{\partial \mathcal{J}_{Rv,ij}}{\partial x_j}\right)^* = 0 \qquad (94)$$

Comparing Eqs. (87) and (94), it is evident that the $(1/c^2)\partial[\ ]/\partial t$ term in Eq. (87) may be neglected.

In order to evaluate $\mathcal{J}_{ij}$ in Eq. (68) and $\mathcal{J}_{v,ij}$ in Eq. (87) for a multicomponent gas, it is necessary to show that Eq. (68) is equivalent to the momentum equation in Ref. (11) except for the radiation terms. Eq. (68) is easily transformed to

$$\rho \frac{Dv_i}{Dt} = - v_i \frac{\partial \rho}{\partial t} - v_i \frac{\partial(\rho v_j)}{\partial x_j} - \frac{\partial p}{\partial x_i} + \frac{\partial \mathcal{J}_{v,ij}}{\partial x_j} + \frac{\partial \mathcal{J}_{R,ij}}{\partial x_j} \qquad (95)$$

where the $(1/c^2)\partial F_{R,i}/\partial t$ term has been neglected. Multiplying the continuity equation, Eq. (61), by v_i gives

$$0 = v_i \frac{\partial \rho}{\partial t} + v_i \frac{\partial(\rho v_j)}{\partial x_j} \qquad (96)$$

Adding Eqs. (95) and (96) yields

$$\rho \frac{Dv_i}{Dt} = - \frac{\partial p}{\partial x_i} + \frac{\partial \Im_{v,ij}}{\partial x_j} + \frac{\partial \Im_{R,ij}}{\partial x_j} \tag{97}$$

Except for the radiation term involving $\Im_{R,ij}$, Eq. (97) above is equivalent to Eq. (34) in Ref. (11). Consequently,[11, 21]

$$\Im_{v,ij} = (\mathcal{K} - \frac{2}{3}\mu) \frac{\partial v_\ell}{\partial x_\ell} \delta_{ij} + \mu\left(\frac{\partial v_i}{\partial x_j} + \frac{\partial v_j}{\partial x_i}\right) - \rho \sum_k Y_k V_{k,i} V_{k,j} \tag{98}$$

where $\mathcal{K}$ is the coefficient of bulk viscosity for the mixture, and μ is the dynamic viscosity for the mixture.

D. Energy Equation

Simon[13] has derived the energy equation for a gas in the presence of radiation. It is

$$\frac{\partial}{\partial t}\left(\rho\bar{e} + \frac{1}{2}\rho v^2\right) + \frac{\partial}{\partial x_i}\left[\left(\rho\bar{e} + \frac{1}{2}\rho v^2\right)v_i\right] + \frac{\partial E_R}{\partial t} + \frac{\partial F_{R,i}}{\partial x_i} + \frac{\partial}{\partial x_i}\left[\left(\rho\delta_{ij} - \Im_{v,ij}\right)v_j + F_i\right] = 0 \tag{99}$$

where $\bar{e}$ is the internal energy per unit mass of gas, v is the magnitude of the mass-weighted average velocity $\vec{v}$, F_i is the ith component of the heat flux density of the gas itself, and E_R is the energy density of radiation given by

$$E_R = \frac{1}{c}\int_0^\infty \oint B_\nu \, d\Omega \, d\nu \tag{100}$$

Equation (99) can be written

$$\rho \frac{D}{Dt}\left(\bar{e} + \frac{1}{2} v^2\right) + \left(\bar{e} + \frac{1}{2} v^2\right)\left(\frac{\partial \rho}{\partial t} + \frac{\partial(\rho v_i)}{\partial x_i}\right) + \frac{\partial E_R}{\partial t}$$

$$+ \frac{\partial F_{R,i}}{\partial x_i} + \frac{\partial(p v_j)}{\partial x_j} - \frac{\partial(\Im_{v,ij} v_j)}{\partial x_i} + \frac{\partial F_i}{\partial x_i} = 0 \qquad (101)$$

The second term is zero by virtue of Eq. (61).

If the scalar product of $\vec{v}$ with $\rho D\vec{v}/Dt$ is taken, Eq. (97) becomes

$$\rho v_i \frac{Dv_i}{Dt} = - v_i \frac{\partial p}{\partial x_i} + v_i \frac{\partial \Im_{v,ij}}{\partial x_j} + v_i \frac{\partial \Im_{R,ij}}{\partial x_j} \qquad (102)$$

From Eq. (102) it follows that

$$\rho \frac{D}{Dt}\left(\frac{v^2}{2}\right) = \frac{\partial(\Im_{v,ij} v_j)}{\partial x_i} - v_i \frac{\partial p}{\partial x_i} + v_j \frac{\partial \Im_{R,ij}}{\partial x_i} - \Im_{v,ij} \frac{\partial v_j}{\partial x_i} \qquad (103)$$

Combining Eqs. (101) and (103),

$$\rho \frac{D\bar{e}}{Dt} = - \frac{\partial E_R}{\partial t} - \frac{\partial F_{R,i}}{\partial x_i} - p \frac{\partial v_j}{\partial x_j} + \Im_{v,ij} \frac{\partial v_j}{\partial x_i}$$

$$+ v_j \frac{\partial \Im_{R,ij}}{\partial x_i} - \frac{\partial F_i}{\partial x_i} \qquad (104)$$

Equations (53) and (54) in Ref. (11) may be combined to give Eq. (104) except for the radiation terms and the body force. Consequently[11],

$$\bar{e} = \sum_k Y_k \bar{e}_k + \frac{1}{2} \sum_k Y_k V_{k,j} V_{k,j} \qquad (105)$$

where $\bar{e}_k$ is the internal energy of species k per unit mass of species k. Also[11]

$$F_i = -\zeta \frac{\partial T}{\partial x_i} - \sum_k \mathcal{J}_{k,ij} V_{k,j} + \rho \sum_k Y_k \bar{e}_k V_{k,i}$$

$$+ \frac{\rho}{2} \sum_k Y_k V_{k,j} V_{k,j} V_{k,i} \tag{106}$$

where ζ is the thermal conductivity of the gas mixture, and the stress tensor $\mathcal{J}_{k,ij}$ gives the external force $\vec{\xi}_k$ on species k per unit area on the surface of a volume, moving with the average velocity $\vec{v}_k$ of species k. The stress $\vec{\xi}_k$ is due to the molecules of species k crossing the surface.

$$\xi_{k,i} = \mathcal{J}_{k,ij} n_j \tag{107}$$

where n_j is the jth component of the outward unit normal.

Enthalpy $\bar{h}$ per unit mass is defined by

$$\bar{h} \equiv \bar{e} + \frac{p}{\rho} \tag{108}$$

From Eqs. (63) and (108) it is easily shown that

$$\rho \frac{D\bar{h}}{Dt} = \rho \frac{D\bar{e}}{Dt} + \frac{Dp}{Dt} + p \frac{\partial v_i}{\partial x_i}$$

So Eq. (104) becomes

$$\rho \frac{\partial \bar{h}}{\partial t} + \rho v_i \frac{\partial \bar{h}}{\partial x_i} = \frac{\partial p}{\partial t} + v_i \frac{\partial p}{\partial x_i} - \frac{\partial E_R}{\partial t} + \beth_{v,ij} \frac{\partial v_j}{\partial x_i}$$

$$+ v_j \frac{\partial \beth_{R,ij}}{\partial x_i} - \frac{\partial F_i}{\partial x_i} - \frac{\partial F_{R,i}}{\partial x_i} \tag{109}$$

To nondimensionalize Eq. (109), neglect the diffusion terms in Eq. (106) with the result

$$F_i \approx - \zeta \frac{\partial T}{\partial x_i} \tag{110}$$

Let

$$\zeta \equiv \zeta_s \zeta^* \tag{111}$$

$$T \equiv T_s T^* \tag{112}$$

$$\bar{h} \equiv C_{ps} T_s \bar{h}^* \tag{113}$$

where C_{ps} is a characteristic specific heat at constant pressure for the gas. Also let

$$E_R \equiv \frac{R_s^{\circ} \bar{k}_L P \ell L}{c} E_R^* \tag{114}$$

$$P_e \equiv \frac{C_{ps} \rho_s U_s L}{\zeta_s} \tag{115}$$

where P_c is the Péclet number. For a perfect gas with constant specific heat it is readily shown that

$$\frac{U_s^2}{C_{ps} T_s} = (\gamma - 1) M_s^2 \tag{116}$$

where γ is the characteristic ratio of specific heats and M_s is the characteristic Mach number. Equation (116) is quite adequate for non-dimensionalizing Eq. (109) even if the gas is imperfect and has variable specific heat.

For the case $k_{LP\ell} \leq 1$ quantities defined by Eqs. (73), (74), (110) - (114), etc. are substituted into Eq. (109), the resultant equation multiplied by $L/\rho_s U_s^3$, and advantage taken of Eqs. (115), (116), etc. with the result

$$\frac{S}{(\gamma-1)M_s^2}\left(\rho\frac{\partial\bar{h}}{\partial t}\right)^* + \frac{1}{(\gamma-1)M_s^2}\left(\rho v_i\frac{\partial\bar{h}}{\partial x_i}\right)^*$$

$$= S\left(\frac{\partial p}{\partial t}\right)^* + \left(v_i\frac{\partial p}{\partial x_i}\right)^* - SG\left(\frac{\partial E_R}{\partial t}\right)^* + \frac{1}{\mathcal{R}}\left(\beth_{v,ij}\frac{\partial v_j}{\partial x_i}\right)^*$$

$$+ G\left(v_j\frac{\partial \beth_{R,ij}}{\partial x_i}\right)^* + \frac{1}{P_e(\gamma-1)M^2}\left(\frac{\partial(\zeta\,\partial T)}{\partial x_i\partial x_i}\right)^* - \frac{G}{\mathcal{R}}\left(\frac{\partial F_{R,i}}{\partial x_i}\right)^* \tag{117}$$

All terms in Eq. (109) are represented in Eq. (117).

When the diffusion approximation is applicable ($\bar{k}_{LRo}L \gg 1$ etc.), Eq. (109) takes a somewhat different form. Before modifying Eq. (109), however, it is necessary to find E_R in the diffusion approximation. From relations in Ref. (13)

$$E_R = 3P_R - 5\mu_R\frac{\partial v_i}{\partial x_i} - \frac{2}{c^2}\left(\zeta_R\frac{\partial T}{\partial x_i} + 5\mu_R\frac{Dv_i}{Dt}\right)v_i \tag{118}$$

If $\mathcal{R} \ll 1$, Eq. (118) becomes

$$E_R = 3P_R - 5\mu_R \frac{\partial v_i}{\partial x_i} \tag{119}$$

From Eqs. (82), (86), (109), (110), and (119)

$$\rho \frac{\partial \bar{h}}{\partial t} + \rho v_i \frac{\partial \bar{h}}{\partial x_i}$$

$$= \frac{\partial p}{\partial t} + v_i \frac{\partial p}{\partial x_i} - 3 \frac{\partial P_R}{\partial t} + 5 \frac{\partial}{\partial t} \left(\mu_R \frac{\partial v_i}{\partial x_i} \right) + \beth_{v,ij} \frac{\partial v_j}{\partial x_i}$$

$$- v_j \frac{\partial P_R}{\partial x_j} + v_j \frac{\partial \beth_{Rv,ij}}{\partial x_i} + \frac{\partial}{\partial x_i} \left[(\zeta + \zeta_R) \frac{\partial T}{\partial x_i} \right]$$

$$- 4 \frac{\partial (P_R v_i)}{\partial x_i} + \frac{\partial}{\partial x_i} \left[\mu_R \left(6 v_j \frac{\partial v_i}{\partial x_j} + 5 \frac{\partial v_i}{\partial t} + 6 v_i \frac{\partial v_\ell}{\partial x_\ell} + v_j \frac{\partial v_j}{\partial x_i} \right) \right] \tag{120}$$

Equation (120) is most easily nondimensionalized if a radiation Péclet number P_{eR} is defined.

$$P_{eR} \equiv \frac{C_{ps} \rho_s U_s L}{\zeta_{Rs}} \tag{121}$$

Substituting characteristic and starred quantities into Eq. (120), multiplying by $L/\rho_s U_s^3$, and utilizing Eq. (121) gives

$$\frac{S}{(\gamma-1)M_s^2}\left(\rho\frac{\partial\bar{h}}{\partial t}\right)^* + \frac{1}{(\gamma-1)M_s^2}\left(\rho v_i\frac{\partial\bar{h}}{\partial x_i}\right)^*$$

$$= S\left(\frac{\partial p}{\partial t}\right)^* + \left(v_i\frac{\partial p}{\partial x_i}\right)^* - 3S\mathcal{G}\left(\frac{\partial P_R}{\partial t}\right)^* - 4\mathcal{G}\left[\frac{\partial}{\partial x_i}\left(P_R v_i\right)\right]^*$$

$$+\frac{5S}{\mathcal{R}_R}\left[\frac{\partial}{\partial t}\left(\mu_R\frac{\partial v_i}{\partial x_i}\right)+\frac{\partial}{\partial x_i}\left(\mu_R\frac{\partial v_i}{\partial t}\right)\right]^* + \frac{1}{\mathcal{R}}\left(\mathcal{J}_{v,ij}\frac{\partial v_j}{\partial x_i}\right)^*$$

$$-\mathcal{G}\left(v_i\frac{\partial P_R}{\partial x_i}\right)^* + \frac{1}{P_e(\gamma-1)M_s^2}\left[\frac{\partial}{\partial x_i}\left(\zeta\frac{\partial T}{\partial x_i}\right)\right]^*$$

$$+\frac{1}{\mathcal{R}_R}\left\{v_j\frac{\partial\mathcal{J}_{Rv,ij}}{\partial x_i}+\frac{\partial}{\partial x_i}\left[\mu_R\left(6v_j\frac{\partial v_i}{\partial x_j}+6v_i\frac{\partial v_\ell}{\partial x_\ell}+v_j\frac{\partial v_j}{\partial x_i}\right)\right]\right\}^*$$

$$+\frac{1}{P_{eR}(\gamma-1)M_s^2}\left[\frac{\partial}{\partial x_i}\left(\zeta_R\frac{\partial T}{\partial x_i}\right)\right]^* \qquad (122)$$

This is the final form of the nondimensionalized energy equation with the diffusion approximation. All terms in Eq. (120) are represented in Eq. (122).

V. COUPLING OF RADIATION AND CONVECTION IN DETACHED SHOCK LAYERS[14]

In Section IIF radiant energy transfer to the nose cone of a reentry missile was considered in the transparent gas approximation for the special case in which it is justified to assume that radiation losses account for only a minor fraction of the energy in the shock layer. In these studies it is customary to solve for the flow field without regard to the radiation problem and then to use the resulting temperature, density, and composition profiles for making approxi-

mate estimates of the radiant energy transport. This type of perturbation calculation must clearly become invalid for sufficiently large reentry velocities $U^{(20)}$.

Goulard[14] has examined the coupling between radiative and convective energy transport in detached shock layers by using incompressible, axisymmetric potential flow theory in the stagnation region[22]. He justifies this important simplification by noting that the studies of Vaglio-Laurin and Ferri[23] show that exact non-radiative shock layer calculations give results in good accord with those derived from the constant-density assumption in the stagnation region. Goulard[14] shows for transparent gases that the rate of change of the dimensionless temperature $C_p T/\bar{h}_S$ with the logarithm of the axial distance z in the stagnation region is given by the relation

$$\frac{d\left(\frac{C_p T}{\bar{h}_S}\right)}{d \log z} = \frac{4\bar{k}_{L,P\ell,S} y \sigma T_S^4}{\rho_\infty U_\infty \bar{h}_S} \frac{\bar{k}_{L,P\ell}}{\bar{k}_{L,P\ell,S}} \frac{\rho_S}{\rho} \left(\frac{T}{T_S}\right)^4 \qquad (123)$$

where $\bar{h}$ is the specific enthalpy, C_p the specific heat at constant pressure, ρ the density, y the thickness of the stagnation region, the logarithm is to the base e, and the other symbols have their usual meaning. The subscripts S and ∞ denote stagnation and free stream conditions, respectively.

Goulard[14] defines a parameter Γ as the radiant energy lost from an infinite transparent gas layer at the uniform temperature T_S

radiating across its two limiting planes (which are a distance y apart) divided by the total energy crossing the shock layer. Consequently, Eq. (123) becomes

$$\frac{d\left(\frac{C_p T}{\bar{h}_S}\right)}{d \log z} = \Gamma \frac{\bar{k}_{L, P\ell}}{\bar{k}_{L, P\ell, S}} \frac{\rho_S}{\rho} \left(\frac{T}{T_S}\right)^4 \tag{124}$$

The parameter Γ plays a prominent role in problems on stellar turbulence[4].

Goulard[14] obtains simple solutions for heated air for the special case $\Gamma \ll 1$, which he shows to be applicable for representative reentry vehicles with a one foot nose radius for several weight-to-drag ratios and reentry angles at reentry velocities up to 35,000 feet per second (compare Fig. 4). The occurrence of radiant energy transport decreases T_S and convective heat transfer. The conventional perturbation procedure, in which the flow equations are first solved, and radiant energy transfer is computed for an isothermal shock layer, overestimates the heat transfer by an extent that depends on Γ and y. Thus the reduced deviations in radiant heat transfer and temperature from the corresponding values in which radiant energy loss is not considered in the solution of the flow equations become

$$\frac{q_R - q_R^o}{q_R^o} = -(\beta + 3) \quad \text{for} \quad \Gamma \ll 1 \tag{125}$$

and

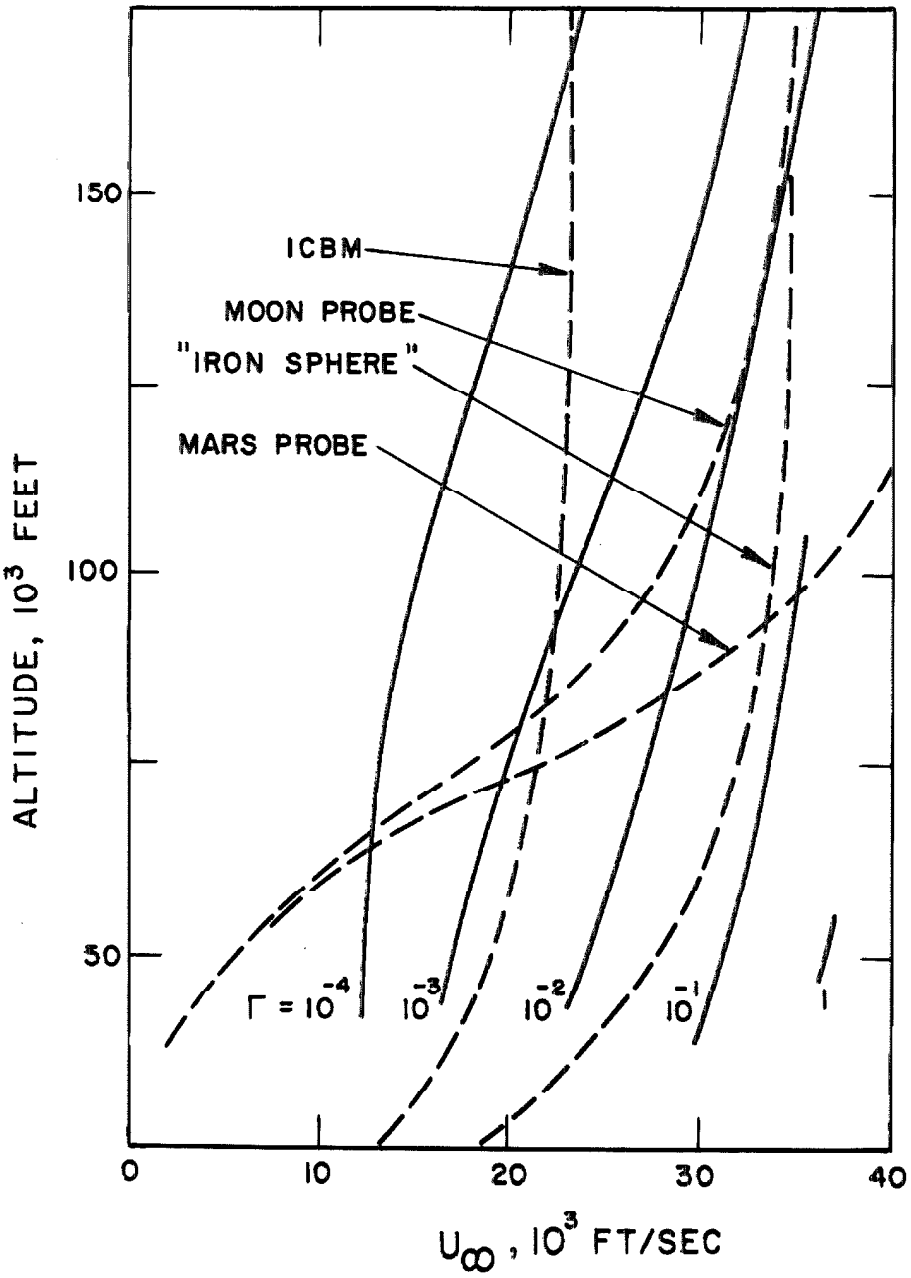

Fig. 4. Altitude-velocity curves for selected missions and curves of constant Γ for the stagnation point of the shock layer formed over a hemispherical nose cone of one foot radius; reproduced from Ref. (14).

$$\frac{T - T_S}{T_S} = \Gamma \log \left(\frac{z}{y}\right) \quad \text{for} \quad \Gamma \ll 1 \tag{126}$$

where the logarithm is to the base e, and β is defined by the relation

$$\frac{\overline{k}_{L,\,P\ell}}{\overline{k}_{L,\,P\ell,\,S}} \frac{\rho_S}{\rho} = \left(\frac{T}{T_S}\right)^{\beta}, \quad \beta \approx 7 \text{ to } 10 \tag{127}$$

The quantities q_R and q_R^o denote, respectively, the calculated radiative energy transport with and without coupling of radiation and convection.

VI. SPECTRAL ABSORPTION COEFFICIENTS IN MOLECULAR SYSTEMS[7]

Thus far in the present discussion nothing has been said about the evaluation of spectral absorption coefficients either from experimental measurements or from theoretical studies. For high-temperature gases this subject is of vast scope since it involves many topics in theoretical spectroscopy and high-temperature thermodynamics. In this section and the next section the physical ideas involved in two particular calculations are summarized.

The derivation of simplified relations for the computation of spectral absorption coefficients in electronic band systems of diatomic molecules is considered in the reprint below. These band systems fall in the ultraviolet and visible regions of the spectrum and make important contributions to radiant energy transfer at elevated temperatures. For example, the NO molecules formed at equilibrium in the heated air behind the detached shock contribute to the radiant heat transfer to the nose cone of a reentry vehicle.

J. Quant. Spectrosc. Radiat. Transfer. Vol. 2, pp. 263–271. Pergamon Press Ltd. Printed in Great Britain

APPROXIMATE SPECTRAL ABSORPTION COEFFICIENT CALCULATIONS FOR ELECTRONIC BAND SYSTEMS BELONGING TO DIATOMIC MOLECULES*

R. W. PATCH† W. L. SHACKLEFORD† and S. S. PENNER

Division of Engineering
California Institute of Technology
Pasadena, California

(*Received* 22 *November* 1961)

Abstract—The spectral absorption coefficients in electronic band systems of diatomic emitters have been computed in the past by models that may be described as 'the just overlapping line model' and a model 'utilizing a smeared out rotational structure'. Although the basic relations are obtained by utilizing somewhat different physical arguments, the resulting equations are, in fact, identical.

Spectral absorption coefficients have been calculated for the NO γ-bands at 2000°K by using the approximate theoretical relations. The calculated results are in good agreement with estimates derived by numerical calculations in which, however, the absorption coefficient data were averaged over intervals of 2000 cm^{-1}.

NOMENCLATURE

- B_e rotational constant, (cm^{-1})
- ΔB difference in rotational constants, (cm^{-1})
- c velocity of light, (cm sec^{-1})
- C band factor, (cm^{-1}-atm^{-1})
- D exponential coefficient, (cm)
- e charge of electron, (e.s.u.)
- E energy of level, (ergs)
- f electronic absorption oscillator strength, dimensionless
- h Planck's constant, (erg-sec)
- j rotational quantum number, dimensionless
- k Boltzmann constant, (erg-°K^{-1})
- m mass of electron, (g)
- n number of lines per j'' level for $v''v'$-band, dimensionless
- N particle density, (cm^{-3})
- P_ω average spectral absorption coefficient, (cm^{-1}-atm^{-1})
- p pressure, (atm)
- q Franck–Condon factor, dimensionless
- Q partition function, dimensionless
- r internuclear distance, (cm)

*Supported by the Air Force Office of Scientific Research under Contract AF 49 (638)-984.
†NSF Predoctoral Fellow.

S integrated absorption coefficient for line, (cm^{-2}-atm^{-1})
T temperature, (°K)
v vibrational quantum number, dimensionless
$\delta\omega$ average line spacing, (cm^{-1})
α integrated absorption coefficient for band, (cm^{-2}-atm^{-1})
ϕ band smearing factor, dimensionless
ψ normalized time-independent vibrational eigenfunction, ($cm^{-1/2}$)
ω term value or wave number, (cm^{-1})

Superscripts

$'$ upper electronic state
$''$ lower electronic state

Subscripts

h band head
j rotational quantum number
v vibrational quantum number
00 0-0 rotationless transition
0 vibrational quantum number 0

I. DERIVATION OF THE THEORETICAL EQUATIONS

THE origin of the theoretical equations obtained for the 'just-overlapping line model' is documented in the literature.[1] Since full appreciation of the results requires considerable familiarity with quantitative spectroscopy, a somewhat simpler derivation is presented in the following section IA. The results derived by using a procedure for smearing the rotational fine structure in electronic band systems have been published and used by KECK *et al.*[2]. Since no derivation of the basic equations is given in Ref. 2, we rederive the desired expressions in section IB.

A. *The 'just-overlapping line model'*

Consider the simplified energy level diagram for a diatomic molecule shown in Fig. 1. Two electronic states are indicated. The vibrational and rotational term values (or energy levels) of the upper electronic state are identified by the subscripts v' and j', respectively; the corresponding term values of the lower electronic state bear the subscripts v'' and j'', respectively. Radiative transitions may take place between vibrational levels of the two electronic states, subject to the rotational selection rules

$$j'-j'' = \pm 1 \text{ or } j'-j'' = 0. \tag{1}$$

The rotational term values for the large values of j'' and j' which make the dominant contributions to the spectral absorption coefficients are given by the expressions

$$\omega_{j''} = j''(j''+1)B_e'' \tag{2}$$

and

$$\omega_{j'} = j'(j'+1)B_e' \simeq j''(j''+1)B_e'. \tag{3}$$

The fraction of the v'' molecules in the j'' state is given by the relation

$$\frac{N_{v''j''}}{N_{v''}} = \frac{(2j''+1)\exp\left[-j''(j''+1)B_e''hc/kT\right]}{\sum_{j=0}^{\infty}(2j''+1)\exp\left[-j''(j''+1)B_e''hc/kT\right]}. \tag{4}$$

It is well known that we may use the approximation

$$\sum_{j''=0}^{\infty}(2j''+1)\exp\left[-j''(j''+1)B_e''hc/kT\right] \simeq \int_0^{\infty} 2j''[\exp(-j''^2 B_e''hc/kT)]\mathrm{d}j'' = \frac{kT}{B_e''hc} \tag{5}$$

at moderate and high temperatures. Hence it follows that

$$\frac{N_{v''j''}}{N_{v''}} \simeq \frac{2j''B_e''hc\exp-[j''(j''+1)B_e''hc/kT]}{kT}. \tag{6}$$

In a given vibration–rotation band involving transitions between v' and v'', each j''-level is found to participate in the formation of $n = 2$ or more rotational lines when proper allowance is made for the selection rules and for spin splitting. We shall simplify the following analysis by assuming that all of these lines have equal integrated absorption coefficients, $S_{v''v';j''}$, viz.,

$$S_{v''v';j''} \equiv \int_0^{\infty} P_{\omega;v''v';j''}\,\mathrm{d}\omega. \tag{7}$$

The sum of $S_{v''v';j''}$ for all of the lines belonging to a specified j''-level is proportional to the population of that level. Letting $\alpha_{v''v'}$ be the integrated absorption coefficient for all lines of all rotational levels for the $v''v'$-band, we find that, approximately,

$$S_{v''v';j''} = \frac{\alpha_{v''v'}}{n}\frac{N_{v''j''}}{N_{v''}} \tag{8}$$

if n represents the number of rotational lines per j''-level. Combining equations (6) and (8), we now obtain

$$S_{v''v';j''} = \frac{2\alpha_{v''v'}j''B_e''hc}{nkT}\exp\left[-j''(j''+1)B_e''hc/kT\right]. \tag{9}$$

Equation (9) is identical with equation (14–31) of Ref. 1 if we use the approximation $j''(j''+1) \simeq j''^2$.

The approximate wave number ω at which a line occurs is given by the difference between the final and initial term values (compare Fig. 1), i.e.,

$$\omega = \omega_{v'} - \omega_{v''} + \omega_{j'} - \omega_{j''}. \tag{10}$$

Combining equations (2), (3), and (10), we obtain

$$\omega = \omega_{v'} - \omega_{v''} - j''(j''+1)(B_e'' - B_e'). \tag{11}$$

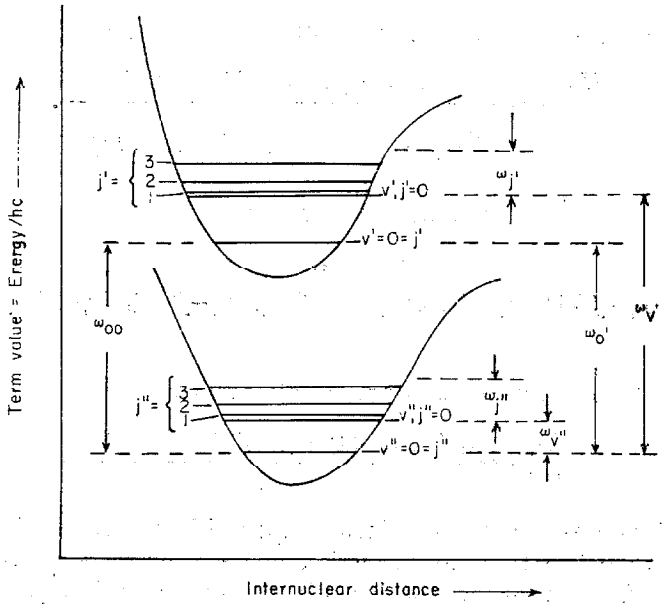

FIG. 1. Simplified energy level diagram for diatomic molecules. The spacing of the rotational levels is exaggerated for the sake of clarity.

For a given vibrational transition, $\omega_{v'}$ and $\omega_{v''}$ are constant whence it follows that the average line spacing $\delta\omega_{j''}$ in a band where each j''-level is associated with n lines is*

$$\delta\omega_{j''} = \frac{2j''|B_e'' - B_e'|}{n} = \frac{2j''\Delta B}{n} \tag{12}$$

where

$$\Delta B \equiv |B_e'' - B_e'|. \tag{13}$$

Combining equations (9) and (12), and setting $P_{\omega;v''v'}$ equal to the local value of $S_{v''v';j''}$ divided by the local line spacing (i.e. using a 'just-overlapping' line model), we find for the $v''v'$-band that

$$P_{\omega;v''v'} = \frac{S_{v''v';j''}}{\delta\omega_{j''}} = \frac{\alpha_{v''v'}B_e''hc}{kT\Delta B}\exp -[j''(j''+1)B_e''hc/kT]. \tag{14}$$

We may replace $j''(j''+1)$ in equation (14) by writing equation (11) in the form

$$j''(j''+1) = \frac{\omega - \omega_{v'} + \omega_{v''}}{B_e' - B_e''} \tag{15}$$

provided that the right-hand side of equation (15) is positive. If it is negative, ω lies in a wave number region where no rotational transitions occur and, therefore, $P_{\omega;v''v'}$ is to be set equal to zero.

*Equations (12) and (14) are equivalent to equations (14–33) and 14–34) of Ref. 1, if we note that the line spacing in Ref. 1 is computed for each *branch* of a band. The present method appears simpler conceptually since we do not require a final summation over band branches.

The integrated absorption coefficient, $\alpha_{v''v'}$, is related to the electronic absorption oscillator strength, f, and the Franck–Condon factor, $q_{v''v'}$ by the expression

$$\alpha_{v''v'} = \frac{\pi e^2 N f q_{v''v'}}{mc^2 p Q_{v''}} \exp(-hc\omega_{v''}/kT) \tag{16}$$

if induced emission terms are negligibly small, which will normally be justified except at high temperatures. The Franck–Condon factor is defined, as usual, by the square of the vibrational overlap integral

$$q_{v''v'} = |\int \psi_{v'} \psi_{v''} \, dr|^2. \tag{17}$$

Equation (16) follows directly from equation (2–21) of Ref. 1 and from the definition of the electronic f-number (compare p. 150 of Ref. 1). The vibrational partition function is

$$Q_{v''} = \sum_{v''} \exp -(hc\omega_{v''}/kT) \tag{18}$$

and should be summed from zero over all integral values of v'' to the value corresponding to the dissociation limit.

Combining equations (14) and (16) leads to the relation

$$P_{\omega;v''v'} = \frac{\pi e^2 N f q_{v''v'} h B_e''}{mcp Q_{v''} kT \Delta B} \left\{ \exp -[j''(j''+1)B_e'' + \omega_{v''}] \frac{hc}{kT} \right\}. \tag{19}$$

The actual value of the spectral absorption coefficient is the sum of the contributions made by individual bands in the band system; thus

$$P_\omega = \sum_{v''} \sum_{v'} P_{\omega;v''v'}. \tag{20}$$

Combining equations (11), (19), and (20) we obtain the form of the results given by KECK *et al.*[2] viz.,

$$P_\omega = \frac{\pi e^2 N f h}{mcpkT} \left\{ \exp[-(\omega_{00} - \omega)hc/kT] \right\} \phi \tag{21}$$

where

$$\phi = \frac{B_e''}{Q_{v''} \Delta B} \sum_{v''} \sum_{v'} q_{v''v'} \exp \left\{ -[j''(j''+1)B_e' + \omega_{v'} - \omega_{00}]hc/kT \right\}. \tag{22}$$

It is interesting to observe that the final expression for P_ω is independent of the number of band branches, i.e. it is independent of the value of n.

B. *The 'smeared rotational line model'*

Although KECK *et al.*[2] do not present a detailed derivation of their results, they suggest that equations (21) and (22) may be obtained by refining the procedure described

in an earlier paper by KIVEL, MAYER and BETHE[3], which has recently been adapted to the calculation of spectral absorption coefficients in infrared vibration–rotation bands.[4] The results given in Ref. 4 may also be derived by using a procedure analogous to that described in the preceding section IA.

We start with the equation*

$$\frac{1}{f_{v'v''}}\frac{\mathrm{d}f_{v'v''}}{\mathrm{d}\omega} \propto \frac{\mathrm{d}}{\mathrm{d}\omega}\left[\exp(-E_{j''}/kT)\right], \tag{23}$$

and we find therefore that

$$\frac{\mathrm{d}f_{v'v''}}{\mathrm{d}\omega} \simeq f_{v'v''}\frac{hcB_e''}{|B_e' - B_e''|kT}\exp(-E_{j''}/kT) \tag{24}$$

since

$$E_{j''} \simeq j''(j''+1)hcB_e'' \simeq \frac{hcB_e''}{B_e' - B_e''}(\omega - \omega_{v'v''}). \tag{25}$$

Equation (24) holds for $B_e' \neq B_e''$ if $|B_e' - B_e''|$ represents the absolute value of the difference between the rotational constants. For a band system, we must again sum over v'' and v' in order to obtain all contributions at a given wave number. Thus

$$\sum_{v'}\sum_{v''}\frac{N_{v''}}{p}\frac{\mathrm{d}f_{v'v''}}{\mathrm{d}\omega} \simeq \sum_{v'}\sum_{v''}\frac{N_{v''}}{p}f_{v'v''}\frac{hcB_e''}{|B_e' - B_e''|kT}\exp(-E_{j''}/kT) \tag{26}$$

where $N_{v''}$ is the total number of molecules per unit volume in the lower electronic state with vibrational quantum number v'' and p denotes the pressure.

In terms of the Franck–Condon factors $q_{v'v''}$, we may write

$$f_{v'v''} = fq_{v'v''} \tag{27}$$

where f is the electronic f-number. Setting N equal to the total concentration of absorbing species, and noting the equilibrium relation

$$\frac{N_{v''}}{N} = \frac{\exp(-E_{v''}/kT)}{Q_{v''}}, \tag{28}$$

we find that

$$\frac{N_{v''}}{p}\frac{\mathrm{d}f_{v'v''}}{\mathrm{d}\omega} \simeq \frac{hcB_e''f}{|B_e' - B_e''|kT}\frac{N}{p}\frac{1}{Q_{v''}}q_{v'v''}\left[\exp-(E_{v''}+E_{j''})/kT\right]. \tag{29}$$

The spectral absorption coefficient at the wave number ω associated with the $v''v'$-band, $P_{\omega;v''v'}$, may now be obtained from the relation

$$P_{\omega;v''v'} = \frac{\pi e^2}{mc^2}\frac{N_{v''}}{p}\frac{\mathrm{d}f_{v'v''}}{\mathrm{d}\omega} \tag{30}$$

whence it follows, in view of equation (29), that equation (19) is obtained. Proceeding as before, we may again derive equations (21) and (22).

*Compare equation (14–6) of Ref. 1 and the basic equation used in Ref. 4.

II. CALCULATIONS OF SPECTRAL ABSORPTION COEFFICIENTS FOR THE NO γ-BANDS AT 2000°K

From equations (15), (21), and (22) we obtain the relation

$$P_\omega = \frac{\pi e^2 N f h B_e''}{mcpkTQ_{v''}\Delta B} \sum_{v''} \sum_{v'} q_{v''v'} \exp\left\{ -\left[\frac{\omega - \omega_{v'} + \omega_{v''}}{B_e' - B_e''} B_e' + \omega_{v''} - \omega \right] (hc/kT) \right\} \quad (31)$$

or

$$P_\omega = \sum_{v''} \sum_{v'} \frac{\pi e^2 N f h B_e'' q_{v''v'}}{mcpkTQ_{v''}\Delta B} \left[\exp - \left(\frac{\omega_{v''} B_e' - \omega_{v'} B_e''}{B_e' - B_e''} \right) \frac{hc}{kT} \right] \left[\exp - \left(\frac{B_e''}{B_e' - B_e''} \right) \frac{hc\omega}{kT} \right]. \quad (32)$$

Let

$$C_{v''v'} = \frac{\pi e^2 N f h B_e'' q_{v''v'}}{mcpkTQ_{v''}\Delta B} \left[\exp - \left(\frac{\omega_{v''} B_e' - \omega_{v'} B_e''}{B_e' - B_e''} \right) \frac{hc}{kT} \right] \quad (33)$$

and

$$D \equiv \frac{B_e'' hc}{(B_e' - B_e'')kT}. \quad (34)$$

Then

$$P_{\omega;v''v'} = C_{v''v'} \exp(-D\omega) \quad (35)$$

or

$$\ln P_{\omega;v''v'} = -D\omega + \ln C_{v''v'}. \quad (36)$$

Reference to equation (36) shows that $\ln P_{\omega;v''v'}$ varies linearly with ω and that the slopes of these plots are independent of ω. To the order of approximation to which the present theory has been worked out, it is apparent that the band head coincides with the band origin (compare equation (11)).* Consequently, it is only necessary to compute $P_{\omega;v''v'}$ at $\omega = \omega_{v'} - \omega_{v''}$ and then to draw appropriate straight lines. The value of $P_{\omega;v''v'}$ at the band head is

$$P_{\omega;v''v';h} = \frac{\pi e^2 N f h B_e'' q_{v''v'}}{mcpkTQ_{v''}\Delta B} \exp(-hc\omega_{v''}/kT). \quad (37)$$

Once $P_{\omega;v''v'}$ is known, we may obtain P_ω according to equation (20) by performing a numerical or graphical addition.

The NO γ-bands corresponding to the transitions $A^2\Sigma^+ \rightarrow X^2\Pi$ are important in radiant heat transfer from heated air. An electronic f-number of about 0·0025 has been obtained by WEBER and PENNER[5] and by BETHKE[6] experimentally for this band system. Franck–Condon factors have been calculated by KIVEL, MAYER and BETHE[3]. Assuming an f number of 0·0025, MEYEROTT, SOKOLOFF and NICHOLLS[7] obtained curves of spectral absorption coefficients as a function of wave number for the NO γ-band contribution to the absorption coefficient of air. In order to compare our results directly with

*For the NO γ-system, the band head is actually close to the band origin (cf. p. 405 of Ref. 1).

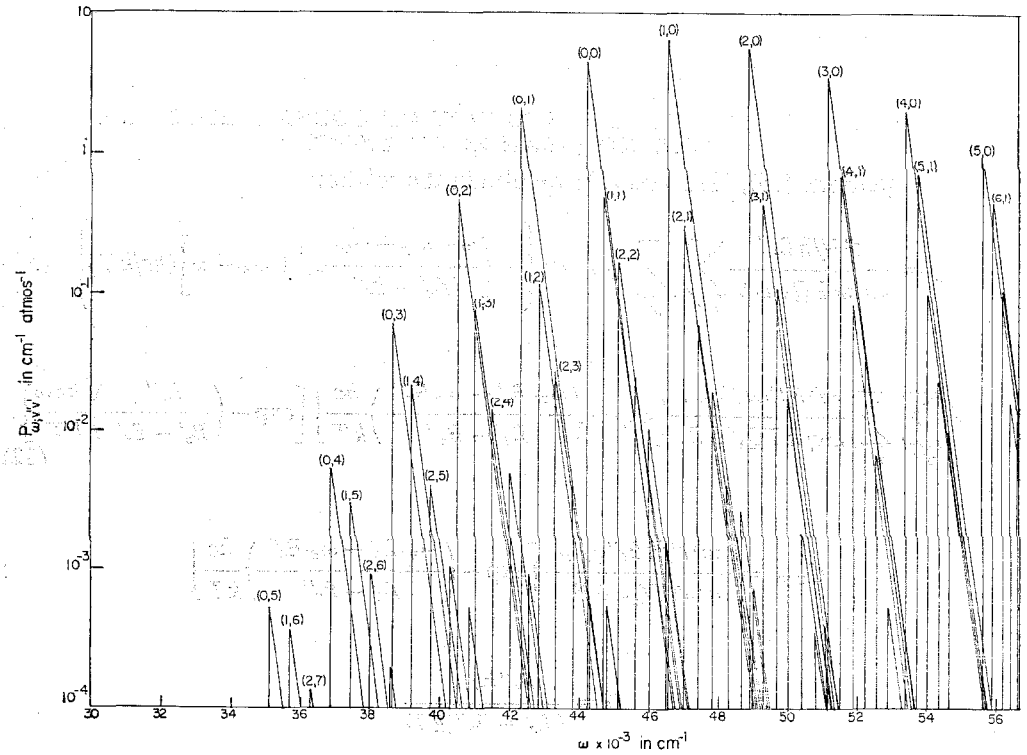

FIG. 2. Approximate values for the spectral absorption coefficients of various NO γ-bands at 2000°K; the numbers in parentheses correspond to (v', v''). The solid curves were computed from equations (34), (35) and (37).

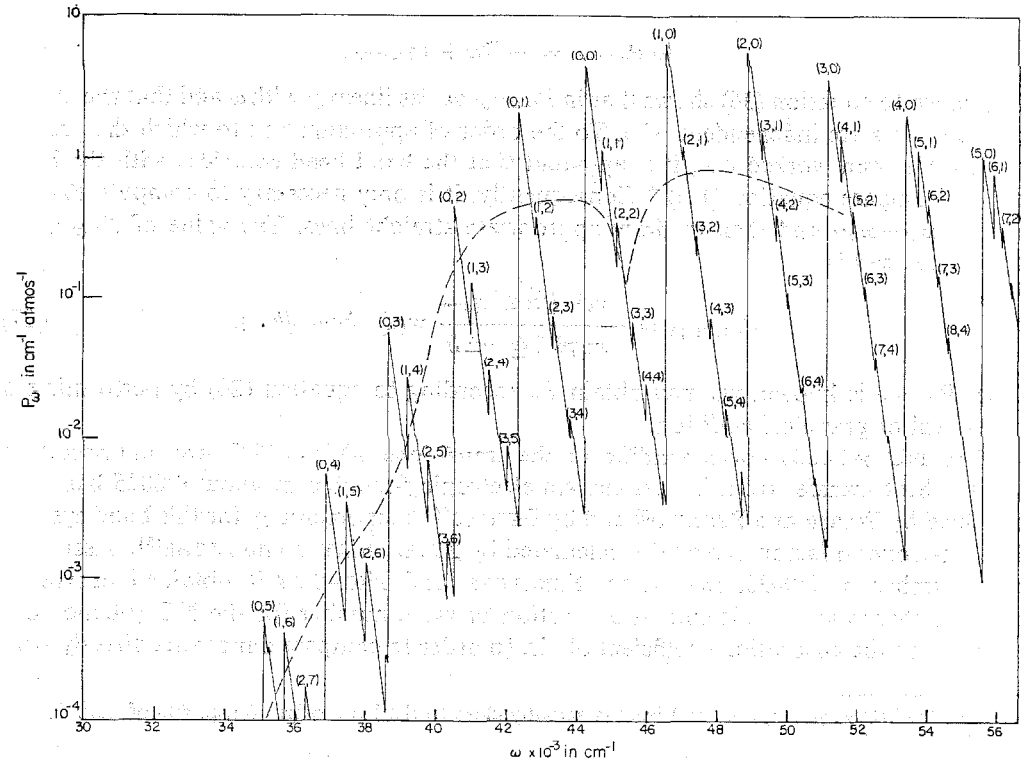

FIG. 3. Approximate values for the spectral absorption coefficients of the NO γ-band system at 2000°K. The solid curves were obtained from the data given in Fig. 2; the dotted curves are taken from Ref. 7. Band heads (v', v'') are indicated on the absorption coefficient curves.

those of MEYEROTT *et al.*, we have also used $f = 0{\cdot}0025$.* Spectroscopic constants were obtained from HERZBERG[8].

Results computed from equations (36) and (37) for $P_{\omega;v''v'}$ at 2000°K are shown in Fig. 2; the final values of P_ω are plotted in Fig. 3, together with the values given in Ref. 7. The method that was used by MEYEROTT *et al.* is not specified in detail, but it is noted that averages were employed over frequency intervals of 2000 cm^{-1}. Consequently, the results shown in Fig. 3 must be considered to be in good agreement.

REFERENCES

1. S. S. PENNER, *Quantitative Molecular Spectroscopy and Gas Emissivities*. Sections 11–8, 11–20 and 14–6. Addison–Wesley, Reading, Mass. (1959).
2. J. C. KECK, J. CAMM, B. KIVEL and T. WENTINK, Jr., *Ann. Phys.* **7**, 1 (1959).
3. B. KIVEL, H. MAYER and H. BETHE, *Ann. Phys.* **2**, 57 (1957).
4. S. S. PENNER, K. P. G. SULZMANN and C. B. LUDWIG, *J.Q.S.R.T.* **1**, 96 (1961).
5. D. WEBER and S. S. PENNER, *J. Chem. Phys.* **26**, 860 (1957).
6. G. W. BETHKE, *J. Chem. Phys.* **31**, 662 (1959).
7. R. E. MEYEROTT, J. SOKOLOFF and R. W. NICHOLLS, *Absorption Coefficients of Air*, Lockheed Aircraft Corporation, Missiles and Space Division, Report LMSD-288052 (1959).
8. G. HERZBERG, *Molecular Spectra and Molecular Structure, Volume I, Spectra of Diatomic Molecules*, Van Nostrand, Princeton, N.J. (1950).

*KECK *et al.* have obtained the value $f = 0{\cdot}001 \pm 0{\cdot}0005$ from high-temperature emission measurements.

VII. CONTINUUM RADIATION IN HEATED PLASMAS

At very high temperatures gas plasmas consist largely of atoms, ions, and electrons. These systems emit at equilibrium both discrete (line) radiation and continua. The line radiation can be estimated only with considerable difficulty[24, 25] since it usually involves a large number of lines of different strengths. However, the continuum radiation can be approximated quite simply[16-18]. As the temperature is raised, most of the atoms and ions equilibrate in excited energy states which may be considered to be similar in first approximation to the excited states of the H atom. Therefore, it may be assumed that at sufficiently high temperatures, the continuum emission from a heated plasma results largely from bound-free transitions and free-free transitions* of atoms and ions, the excited states of which may be described by hydrogenic wave functions.

In the hydrogenic approximation the total linear absorption coefficient $k_{L,m}$ with a bound-free contribution from an m-ion (i.e., an m times ionized atom) and a free-free contribution from an (m+1) ion may be written as[4]

$$k_{L,m}(\chi) = aN_m(m+1)^2\theta^{-2}e^{-\chi}im F_m(\chi) \qquad (128)$$

where

*An example of a bound-free transition involving the m-times ionized atom A^{m+} is $A^{m+} \rightarrow A^{(m+1)+} + e$; the corresponding free-free transition for the (m+1)-times ionized atom $A^{(m+1)+}$ corresponds to the process $A^{(m+1)+} + e \rightarrow A^{(m+1)+} + e$.

$$a = \frac{16\pi^2}{3\sqrt{3}} \frac{g_e g_{m+1}}{g_m} \frac{e^6}{ch} (1.6 \times 10^{-12})^{-2} \tag{129}$$

$$\chi \equiv \frac{h\nu}{\theta} \tag{130}$$

$$\chi_{i,m} \equiv \frac{I_m}{\theta} \tag{131}$$

$$F_m(\chi) = \chi^{-3} \left(2\chi_{i,m} \sum_{n=1}^{\infty} \frac{e^{\chi_{i,m}/n^2}}{n^3} + 1 \right) \tag{132}$$

Here g_e is the degeneracy of a free electron, g_m is the degeneracy of an m-ion, N_m is the number density (cm^{-3}) of m-ions in the ground state, θ is the temperature in electron volts, e is the charge of an electron, I_m is the ionization potential of the m-ion, and n is the principal quantum number. The sum is to be evaluated for those values of n for which bound-free transitions are possible for a given value of χ. The first term on the right-hand side of Eq. (132) represents the bound-free contribution, and the second term represents the free-free contribution to the absorption coefficient.

The factor $g_e g_{m+1}/g_m$ was approximated by unity by Unsöld[4], and the validity of this approximation for the purposes of this study was confirmed by Penner and Thomas[18]. For $g_e g_{m+1}/g_m = 1$, a has the value 7.3×10^{-16} cm^2 $(eV)^2$.

In an ionized gas containing m-ions with $m = 0, 1, 2, \ldots$, the total continuum absorption coefficient is obtained by summing the contributions made by the separate m-ions, viz.,

$$k_L(\chi) = a0^{-2} \sum_m N_m (m+1)^2 e^{-\chi_{i,m}} F_m(\chi) \tag{133}$$

Following Raizer[16] and Pappert and Penner[17] in making a variety of special assumptions, very simple expressions may be obtained for $k_L(\chi)$ and also for the Planck and Rosseland mean free paths.

In order to obtain the simplified results for the radiation mean free paths and the mean opacities, the following important approximation is made[15]: The mean number of electrons per atom $\overline{m}$ is assumed to be given by the relation

$$I_{m-\frac{1}{2}} = \theta \log \left(\frac{\overline{A}\,\theta^{3/2}}{N\overline{m}} \right) \tag{134}$$

where the logarithm is to the base e and

$$N\overline{m} = N_e \tag{135}$$

is the number of free electrons per unit volume, and N is the total number density (cm^{-3}) of atoms and ions. Also

$$\overline{A} = \frac{g_e g_{m+1}}{g_m} \left[\frac{2\pi m_e (1.6 \times 10^{-12})}{h^2} \right]^{3/2} \tag{136}$$

where m_e is the mass of an electron. For $g_e g_{m+1}/g_m = 1$, $\overline{A}$ has the value $3.0 \times 10^{21}\ cm^{-3}\ (eV)^{-3/2}$.

The empirical relation introduced in Eqs. (134) - (136) is consistent with the Saha equation

$$\frac{N_{m+1} N_e}{N_m} = \overline{A}\,\theta^{3/2} e^{-I_m/\theta} \tag{137}$$

in the following sense: I_m is to be replaced by $I_{\overline{m}-\frac{1}{2}}$, and the hypothetical ion species corresponding to $m = \overline{m} + \frac{1}{2}$ and $m = \overline{m} - \frac{1}{2}$ are equal in number. It has been shown[18] that the number of electrons per atom computed by the use of Eq. (133) agrees with the exact solution of the Saha equation (in which, however, no allowance is made for such factors as the influence of electron concentration on ionization potential, etc.) within a few per cent (compare Fig. 5).

Pappert and Penner[17] and Penner and Thomas[18] have obtained modifications of Raizer's earlier estimates[16] for the Planck and Rosseland mean free paths. The result[18] may be written in the form

$$\overline{\lambda}_{P\ell} \equiv \frac{1}{\overline{k}_{L,\,P\ell}} = \frac{1.8 \times 10^{37}\theta^{7/2}}{N^2\overline{m}\left[(\overline{m}-\frac{1}{2})^2\chi_{i,\,\overline{m}-(3/2)} + (\overline{m}+\frac{1}{2})^2\chi_{i,\,\overline{m}-\frac{1}{2}}\right]} \quad \text{(cm)} \tag{138}$$

where

$$\chi_{i,\,\overline{m}-\frac{1}{2}} = \frac{I_{\overline{m}-\frac{1}{2}}}{\theta} \tag{139}$$

Also

$$\overline{\lambda}_{Ro} \equiv \frac{1}{\overline{k}_{L,\,Ro}} = \frac{3.6 \times 10^{36}\theta^{7/2}}{N^2\overline{m}\,(\overline{m}^2 + (1/4))} \quad \text{(cm)} \tag{140}$$

Eqs. (138) and (140) were derived directly from the definitions given in Eqs. (28) and (43), respectively, by using spectral absorption coefficients computed from Eq. (133).

Equations (138) and (140) have been shown[18] to yield results for nitrogen at a temperature of 5 eV (58,025 ^{o}K) and number densities

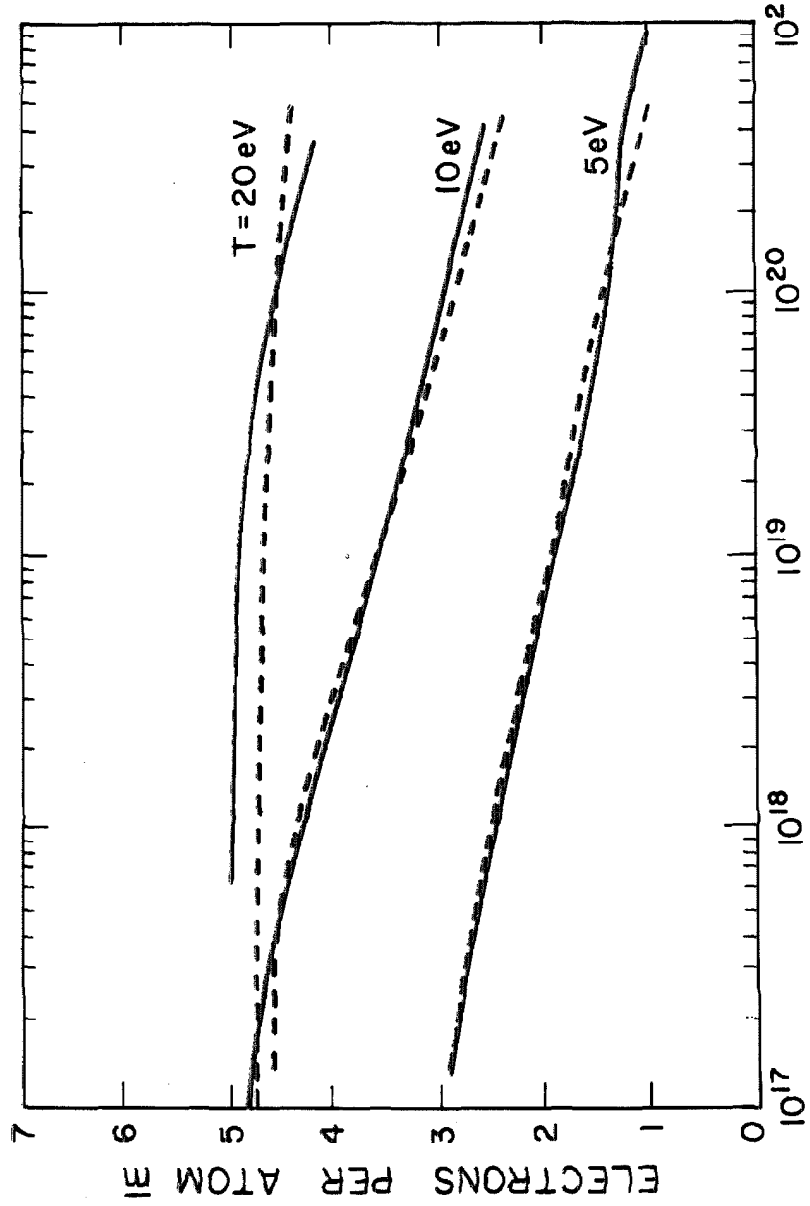

Fig. 5. Average number of free electrons $\bar{m}$ per atom for nitrogen as a function of number density N of atoms and ions at various temperatures. The dashed curve is based on Raizer's approximation, Eq. (134) with $g_e g_{m+1}/g_m = 1$. The solid curve is based on Armstrong's data (26). The graph is based upon a graph in Ref. 18).

from 10^{15} cm^{-3} to 10^{21} cm^{-3} that agree within a factor of three or better with numerical calculations performed by Armstrong[26]. See Fig. 6. Additional calculations[17] were also encouraging.

The simplified method for continuum opacity calculations on high-temperature plasmas should become better for more complicated atoms and ions (i.e., for nuclei with larger atomic number). For atoms such as Be, which has a spectroscopic "window" (i.e., does not emit) for $\chi = h\nu/\theta > 2$, the approximation procedure breaks down.

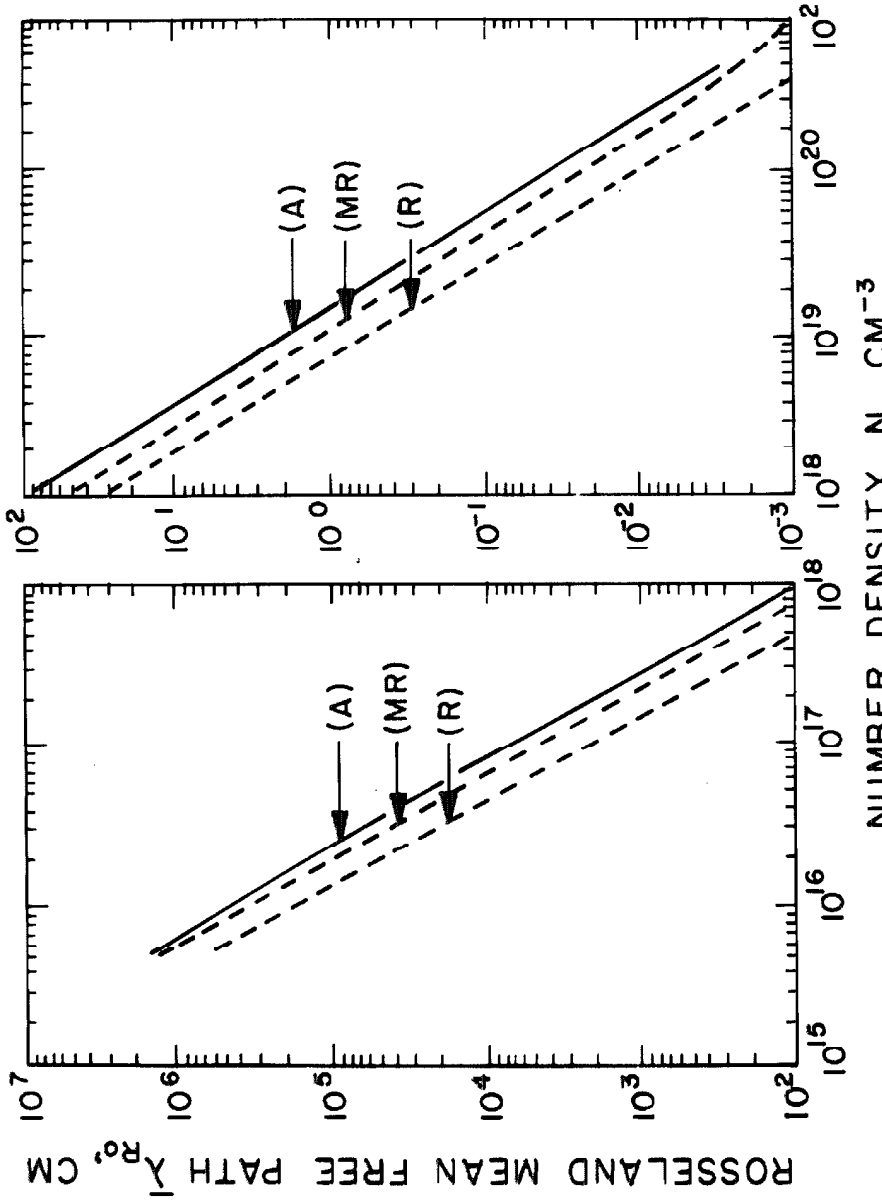

Fig. 6. The Rosseland mean free path as a function of number density N of atoms and ions for nitrogen at 5 eV. The symbols A, R, and MR identify results obtained by by Armstrong (A)[26] and derived from Raizer (R)[16] and modified-Raizer (MR)[17] approximations, respectively. In the latter two cases $g_e g_{m+1}/g_m$ was set equal to one. The graphs are based on two graphs in Ref. (18).

REFERENCES

1. G. Herzberg, Atomic Spectra and Atomic Structure, Prentice-Hall, New York, 1937.

2. G. Herzberg, Spectra of Diatomic Molecules, 2nd ed., D. Van Nostrand, Princeton, 1950.

3. G. Herzberg, Infrared and Raman Spectra of Polyatomic Molecules, D. Van Nostrand, Princeton, 1945.

4. A. Unsöld, Physik der Sternatmosphären, Julius Springer, Berlin, 1958.

5. S. Chandrasekhar, Radiative Transfer, Dover, New York, 1960.

6. V. Kourganoff, Basic Methods in Transfer Problems, Dover, New York, 1963.

7. S. S. Penner, Quantitative Molecular Spectroscopy and Gas Emissivities, Addison-Wesley, Reading, Mass., 1959.

8. A. S. Eddington, The Internal Constitution of the Stars, Cambridge at the University Press, Cambridge, 1926.

9. S. Chapman and T. G. Cowling, The Mathematical Theory of Nonuniform Gases, Cambridge University Press, Cambridge, 1939.

10. C. Truesdell, Handbuch der Physik, Volume III/1, Julius Springer, Berlin, 1960.

11. W. Nachbar, F. Williams, and S. S. Penner, "The Conservation Equations for Independent Coexistent Continua and for Multicomponent Reacting Gas Mixtures," Quart. Appl. Math 17, 43-54 (1959).

12. L. H. Thomas, "The Radiation Field in a Fluid in Motion," Quart. J. Math 1, 239-251 (1930).

13. R. Simon, "The Conservation Equations of a Classical Plasma in the Presence of Radiation," J. Quant. Spectrosc. Radiat. Transfer 3, 1-14 (1963).

14. R. Goulard, "The Coupling of Radiation and Convection in Detached Shock Layers," J. Quant. Spectrosc. Radiat. Transfer 1, 249-257 (1961).

15. Yu. P. Raizer, "A Simple Method of Calculating the Degree of Ionization and Thermodynamic Functions of a Multiply Ionized Ideal Gas," JETP (U. S. S. R.) 9, 1124-1125 (1959).

16. Yu. P. Raizer, "Simple Method for Computing the Mean Range of Radiation in Ionized Gases at High Temperatures," JETP (U. S. S. R.) 10, 769-771 (1960).

17. R. A. Pappert and S. S. Penner, "Approximate Continuous Opacity Calculations for Polyelectronic Atoms at High Temperatures," J. Quant. Spectrosc. Radiat. Transfer 1, 258-268 (1961).

18. S. S. Penner and M. Thomas, "Approximate Theoretical Calculations of Continuum Opacities," Calif. Inst. of Tech., Pasadena, Calif., Technical Report No. 44, Contract Nonr-220(45), NR 015 401, November 1963.

19. R. and M. Goulard, "One-dimensional Energy Transfer in Radiant Media," Int. J. Heat and Mass Transfer 1, 81-91 (1960).

20. R. E. Meyerott, "Radiation Heat Transfer to Hypersonic Vehicles," pp. 431-450 in Third AGARD Combustion and Propulsion Colloquium, Pergamon Press, London, 1959.

21. Rutherford Aris, Vectors, Tensors, and the Basic Equations of Fluid Mechanics, Prentice-Hall, Englewood Cliffs, N. J., 1962.

22. W. D. Hayes and R. F. Probstein, Hypersonic Flow Theory, Academic Press, New York, 1959.

23. R. Vaglio-Laurin and A. Ferri, "Theoretical Investigation of the Flow Field about Blunt-Nosed Bodies in Supersonic Flight," J. Aerospace Sciences 25, 761-770 (1958).

24. Harris Mayer, "Methods of Opacity Calculations," Los Alamos Scientific Laboratory of the University of California, Los Alamos, N. Mex., Report LA-647, March 1948.

25. D. R. Bates and Agnete Damgaard, "The Calculation of the Absolute Strengths of Spectral Lines," Phil. Trans. Roy. Soc. (London) A242, 101-122 (1949).

26. B. H. Armstrong, "Mean Absorption Coefficients of Air, Nitrogen, and Oxygen from 22,000° to 220,000°," Lockheed Aircraft Corp., Sunnyvale, Calif., Report LMSD-49759, July 1959. See also B. H. Armstrong and R. E. Meyerott, "Absorption Coefficients for High-Temperature Nitrogen, Oxygen, and Air," Phys. Fluids 3, 138-140 (1960).

PART II: ABSOLUTE INTENSITY MEASUREMENTS FOR THE 2.7μ BAND OF WATER VAPOR IN A SHOCK TUBE

I. INTRODUCTION

The purpose of this study was two-fold. First, the integrated absorption coefficient of the collective vibration-rotation bands of hot H_2O vapor between 2700 and 4550 wave numbers was desired because this quantity is needed for a priori calculations of the emissivity of H_2O vapor under arbitrary conditions[1]. Such emissivities are needed to study radiant heat transfer in aircraft, missile, and space propulsion devices utilizing fuels containing hydrogen and likewise for heat transfer to vehicles entering or reentering planetary atmospheres and utilizing ablating heat shields containing bound hydrogen. The integrated absorption should also be useful in studying the infrared signature of the wakes of such propulsion devices, wakes of ablating heat shields, and in studying planetary atmospheres.

Second, it was desired to demonstrate that shock tubes can be used to obtain reliable values for spectral and integrated absorption coefficients of a gas provided proper precautions are taken. Some previous work had made this open to question (compare Ref. (2) with (3) and Ref. (3) with (4)).

A review of theoretical calculations of the integrated absorption coefficients of bands and individual lines is appropriate, among other reasons, because such calculations were used to obtain integrated absorption coefficients, cited in this study, for H_2O bands when only the integrated absorption coefficients of single lines were measured.

Cross[5] derived the relative integrated absorption coefficients (or strengths) of individual transitions in a vibration-rotation band of a rigid asymmetric rotor with the same asymmetry in the initial and final states. Yamamoto[6] used Cross's results together with perturbation theory to calculate line and spectral absorption coefficients for H_2O bands at 220 °K and 300 °K. Wyatt[7] made more complete calculations for H_2O bands at 200 °K, 250 °K, and 300 °K assuming Cross's strengths[5] for the stronger lines and symmetric top strengths for the weaker lines. Unfortunately, high temperatures populate many more rotational and vibrational states, greatly complicating calculations. Gray[8] has made simplified calculations for band envelopes of the P- and R-branches of H_2O bands at 1111 °K assuming symmetric top strengths.

In most calculations anomalies in the intensity distribution among the lines of a vibration-rotation band of H_2O cause inaccuracies. These have been observed by Benedict[9] and were presumed to arise from three sources: differing asymmetry in the upper and lower states, Coriolis interactions between different vibrational levels and the rotation, and perturbations between individual vibrational levels[10]. Centrifugal stretching[11], mechanical anharmonicity, and electrical anharmonicity[12] can also cause anomalies. Most of these anomalies are more important at high temperatures.

Past experimental measurements of integrated absorption coefficients of the H_2O bands between 2700 cm^{-1} and 4550 cm^{-1} were accomplished by absorption, emission, or refraction techniques.

Absorption measurements were made by projecting an infrared beam through a volume of H_2O vapor of known thickness $\mathfrak{L}$ and vapor pressure p_{H_2O}. The absorption and induced emission of the H_2O caused a net attenuation of the beam. A monochromator set at a wave number ω was used to transmit only a certain range of wave numbers of this beam to a detector, and an apparent spectral absorption coefficient $P_{\omega, ap}$ (including induced emission) was obtained from the attenuation of the spectral region of the beam measured by the detector.

Assume that the beam was collimated so that the path length L was equal to the thickness $\mathfrak{L}$ of the H_2O. Let $\mathfrak{F}_{e,o}$ be the radiant flux in, say, ergs/sec from the exit slit of the monochromator with no H_2O vapor in the optical path, and let $\mathfrak{F}_e$ be the radiant flux in, say, ergs/sec from the exit slit with H_2O present in a cell in the optical path. Then if the temperature of the vapor was low enough that negligible spontaneous emission was present, $P_{\omega, ap}$ could be defined by

$$\frac{\mathfrak{F}_e}{\mathfrak{F}_{e,o}} \equiv e^{-P_{\omega, ap} L p_{H_2O}} \tag{1}$$

If a monochromator could be built to pass only radiation of a single wave number, then Eq. (1) would become

$$\frac{\mathfrak{F}_e}{\mathfrak{F}_{e,o}} = e^{-P_{\omega} L p_{H_2O}} \tag{2}$$

where P_{ω} is the spectral absorption coefficient including induced

emission. The integrated absorption coefficient a of a band or group of overlapping bands is defined by

$$a \equiv \int_{\text{bands}} P_{\omega'} \, d\omega' \tag{3}$$

where ω' is the wave number of the radiation.

The most common method of making absorption measurements on H_2O involved a cell full of water vapor and equipped with two windows transparent to infrared[13-17]. The light beam went directly through the cell (single pass) or was reflected back and forth to increase the path length. Some cells were heated, but this caused sealing problems that limited this type of cell to 1500 ^{o}K.

A single-pass variant of the above arrangement minimized the sealing problem by placing the windows in cool locations at opposite ends of a coaxial furnace and cell assembly[18]. The windows were each cooled by a continuous flow of inert gas restricted to the ends of the cell. Stable gas-vapor interfaces were achieved between the inert gas at the ends and the water vapor in the center of the cell. To date this cell has only reached 1111 ^{o}K.

Another approach utilized a rocket burner burning H_2 with O_2[19]. A converging-diverging nozzle was provided, and infrared absorption measurements were made utilizing an optical path just downstream of the nozzle exit, intersecting and perpendicular to the rocket axis. A temperature of 2200 ^{o}K was achieved, but minor difficulties were encountered with partial chemical freezing and inhomogeneity of the expanding exhaust flow and absorption of infrared by

atmospheric H_2O and CO_2 just outside the rocket exhaust. The apparatus was limited to 1 atm pressure at the nozzle exit.

In a number of the studies referenced above, the total pressure was not always high enough to assure overlapping lines. To obtain good accuracy, such measurements were almost always made with optically thick gas, for which the relation

$$\alpha \approx \int_{\text{bands}} P_{\omega, ap}\, d\omega \tag{4}$$

was not valid unless the lines overlapped. At too low a static pressure Eq. (4) gives values of α that are too low, as will be discussed in Section VI.

If the integrated absorption coefficient S of a single line of a band is measured, the integrated absorption coefficient α for the entire band may be calculated using the theory mentioned above. Such a measurement was made using a multiple-pass cell and a high resolution monochromator[20]. Unfortunately, α's calculated from such measurements could never be more accurate than the theory used. This method was also used by Benedict[21].

The emission of a single line in a flame may be measured and used to obtain S. Except when using a monochromator of the highest dispersion, the line must be optically thin at all wave numbers, i.e.

$$P_{\omega'} L p_i \ll 1 \tag{5}$$

where p_i is the partial pressure of the emitting species. Such a line is called a weak line. The quantity usually measured is the radiancy

R_L of the line[1]

$$R_L = \pi \int_{\text{line}} \epsilon_{\omega'} B^o_{\omega'} \, d\omega' \approx \pi B^o_{\omega'_o} \int_{\text{line}} \epsilon_{\omega'} \, d\omega' \tag{6}$$

where $\epsilon_{\omega'}$ is the spectral emissivity of the line and $B^o_{\omega'}$ is the spectral blackbody steradiancy (or brightness or intensity) at wave number ω' and the gas temperature. The quantity $B^o_{\omega'_o}$ is the spectral blackbody steradiancy at the wave number ω_o of the center of the line and the gas temperature. It is readily shown that, for a weak line,

$$S \approx \frac{R_L}{\pi B^o_{\omega_o} p_i L} \tag{7}$$

The integrated absorption coefficient a for the band can then be calculated as mentioned above, subject to the same inaccuracies. Difficulty is also encountered from temperature and composition inhomogeneities in the flame.

The refractive index n of H_2O vapor was also used to measure S[22]. From Ref. (1) it is easily shown that

$$S = \frac{(n - n_o) 4\pi^2 \omega_o \left[(\omega_o - \omega')^2 + b^2 \right] \left[1 - e^{-hc\omega_o/kT} \right]}{(\omega_o - \omega') p_i} \tag{8}$$

for a line with dispersion contour, where n_o is the refractive index at the line center, ω_o is the wave number of the line center, b is the half width of the line, h is Planck's constant, c is the velocity of light, k is the Boltzmann constant, and T is the temperature. The

refractive index at wave numbers near ω_o was determined by passing continuum light through a grating monochromator and thence through a refractometer employing a hollow prism containing the water vapor. This method also suffered from inaccuracies in determining α from S theoretically.

Another method of finding α from n involves a monochromator and refractometer of low resolution so that the change in n for individual lines is not resolved[23]; only the slow change in n due to the entire band is recorded. The principal difficulty is the influence of neighboring bands on n. The method has not been applied to H_2O.

The best apparatus for obtaining pure homogeneous vapor at known pressure and known temperature exceeding 1500 ^oK is the shock tube. Because the high temperature in the vapor exists for only a msec or so, the walls are not heated appreciably, so there are no serious sealing problems. However, spectroscopic measurements must be made in a short interval of time, limiting the spectral resolution.

An absorption experiment on the H_2O bands between 2700 cm^{-1} and 4550 cm^{-1} was performed in a shock tube at the California Institute of Technology by Timnat[24]. The water vapor was mixed with Ar and heated to between 1420 ^oK and 2238 ^oK by the incident shock wave. Infrared radiation from a Globar was chopped, passed transversely across the shock tube, dispersed by an IR2 monochromator with an NaCl prism, and detected by a gold-doped germanium photodiode. The resulting signal was recorded on an oscilloscope. The ratio of amplitudes before and after the incident shock gave the change in absorption by the H_2O.

Unfortunately, the NaCl prism provided only moderate dispersion so the monochromator slits had to be narrow, impairing the signal-to-noise ratio. Alignment and mechanical vibration problems also existed. Although emission by H_2O was recorded along with the chopped signal, it could not be evaluated for want of calibration.

Timnat's apparatus was largely rebuilt for the present work, and all these difficulties overcome. The present measurements were mostly made with monochromator slit settings providing an effective band width of 206 cm^{-1} at 3704 cm^{-1} near the center of the group of H_2O bands. The wavelength adjustment of the monochromator was varied in steps of 0.1 μ, causing the measurements to overlap spectrally. The apparent absorption coefficient was measured both in emission and in absorption at nine wave numbers between 3125 cm^{-1} and 4167 cm^{-1} at temperatures near 1000 ^{o}K. The apparent absorption coefficient was measured in emission at nineteen wave numbers between 2703 cm^{-1} and 4545 cm^{-1} at temperatures near 1933 ^{o}K.

II. THEORETICAL CONSIDERATIONS

In this section the vibration-rotation spectrum of H_2O is examined and the measured bands are described. The slit function of a monochromator is discussed. Due to the finite width of the slit function, an apparent absorption coefficient $P_{\omega, ap}$ was measured rather than the true absorption coefficient P_{ω}. The results of this are examined. Pertinent shock tube gas dynamics are reviewed. Emission and absorption equations are given together with relevant corrections and equations for intensity calibration.

A. Vibration-Rotation Spectrum of H_2O Vapor

The H_2O molecule consists of two H atoms each bonded to an O atom at the center. The two bond lengths are equal, but the molecule is bent. It has an angle of 104° 27' between bonds. Consequently, H_2O has three nondegenerate normal vibrations: a symmetric stretching vibration with frequency ν_1 corresponding to 3650.0 cm^{-1}, a bending vibration ν_2 of 1595.0 cm^{-1}, and an assymetric stretching vibration ν_3 of 3755.41 cm^{-1} [12]. The vibrations and rotation are quantized, so the energy E of the molecule is[12]

$$E = (v_1 + \tfrac{1}{2})h\nu_1 + (v_2 + \tfrac{1}{2})h\nu_2 + (v_3 + \tfrac{1}{2})h\nu_3$$

$$+ DJ(J+1) + f(J,\tau) \qquad (9)$$

where we have neglected coupling between the vibrations and rotations and have assumed harmonic oscillators. Here v_1, v_2, and v_3 are vibrational quantum numbers assuming the values

$$v_k = 0, 1, 2, \ldots$$

J is the total angular momentum quantum number assuming the values

$$J = 0, 1, 2, \ldots$$

τ is an index somewhat analogous to a quantum number, which indicates the orientation of the total angular momentum vector with respect to the principal axes of the molecule and assumes the values

$$\tau = -J, -J+1, \ldots, 0, \ldots, J-1, J$$

The quantities ν_1, ν_2, and ν_3 are the classical frequencies of vibration of the three normal modes, and D is a constant. The variable $f(J,\tau)$ is a complicated function of J and τ.

The wave number ω' of a transition is, of course, given by the Bohr frequency condition

$$hc\omega' = E(v_1', v_2', v_3', J', \tau') - E(v_1'', v_2'', v_3'', J'', \tau'') \qquad (10)$$

where ' above a quantum number denotes the upper state, and " denotes the lower state. To the harmonic oscillator approximation it can be shown[11] that only one v_k can change during a transition and then by only one quantum. In practice, however, both these rules are violated, resulting in groups of H_2O vibration-rotation bands near 1590, 3100, 3700, 5300, 7200, and 9100 cm^{-1}. These bands are identified by using the designation

$$v_1''v_2''v_3'' \rightarrow v_1'v_2'v_3'$$

We are interested in the bands near 3100 cm^{-1} and 3700 cm^{-1} which actually all overlap. At room temperature the transitions involved are principally

000 → 100	3650.0 cm^{-1}
000 → 020	3151.0 cm^{-1}
000 → 001	3755.41 cm^{-1}

The third transition here is much the strongest. At higher temperatures H_2O becomes vibrationally excited so transitions such as[8]

$010 \rightarrow 030$	$3073.4\ cm^{-1}$
$010 \rightarrow 011$	$3737.0\ cm^{-1}$
$010 \rightarrow 110$	$3630.0\ cm^{-1}$

become important. Of course, bands with $\Delta v_1 = 1$ all have about the same wave number, and likewise for $\Delta v_2 = 2$ and $\Delta v_3 = 1$. Bands that obey the harmonic oscillator selection rules given above tend to be stronger than those that do not. Each band contains a large number of lines corresponding to different changes in J and τ and to different initial quantum states.

No line is actually monochromatic as Eq. (10) might lead one to think. The line is broadened by natural broadening due to Heisenberg's uncertainty principle, Doppler broadening due to the velocity of the molecules, and collision broadening due to perturbations during collisions. Collision broadening predominates in all cases in this study and is proportional to $pT^{-1/2}$.

B. The Slit Function

The slit function $g(\omega' - \omega)$ is proportional to the response of a monochromator set at ω to radiation of the same or slightly different wave number ω' [1]. For this study g will always be normalized so that

$$\int_0^\infty g(\omega' - \omega)\, d\omega' = 1 \qquad (11)$$

Ideal slit functions for equal and for unequal entrance and exit slits for a monochromator that is not near its limit of resolution are given in Fig. 1A and Fig. 1B, respectively. Actual monochromators may

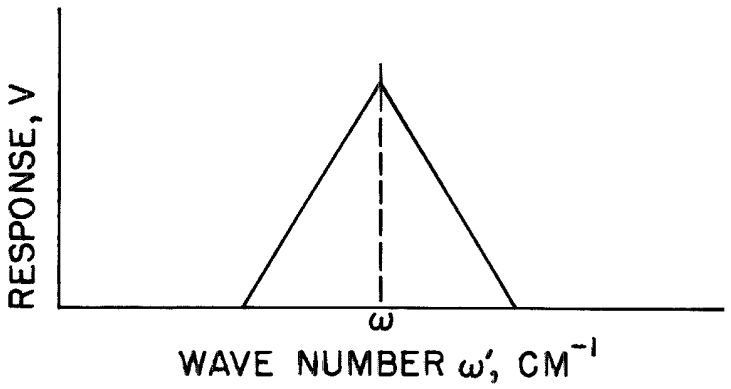

Fig. 1A. Ideal slit function of monochromator with equal entrance and exit slits.

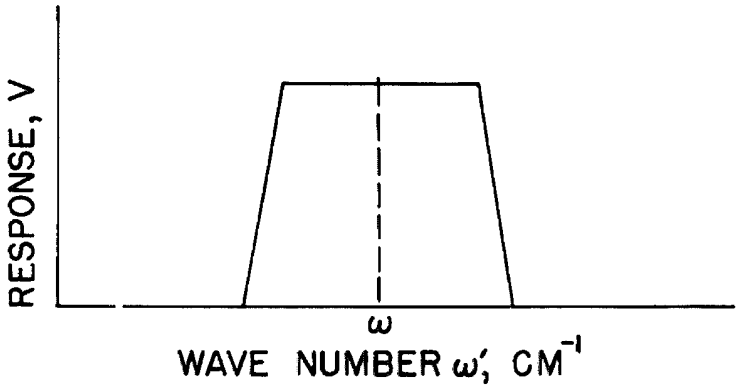

Fig. 1B. Ideal slit function of monochromator with unequal entrance and exit slits.

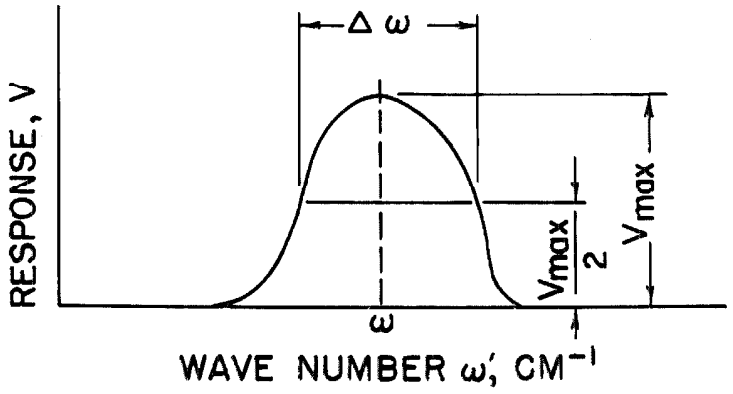

Fig. 1C. Diagram showing how the effective band width is obtained from any slit function.

depart from these somewhat due to various defects. The width of the slit function is described by the effective band width, which is determined as shown in Fig. 1C.

To measure the slit function, a light source containing an isolated spectral line is required. The wave number control of the monochromator is then moved through the wave number of the line, while simultaneously measuring the energy of the radiation passing through the exit slit. If we call the slit function thus measured with ω' constant $g(\omega' - \omega)_{\omega'}$ and call the desired slit function measured with ω constant $g(\omega' - \omega)_{\omega}$ then

$$g(\omega' - \omega)_{\omega} \approx g(\omega' - \omega)_{\omega'} \tag{12}$$

This relation would be exact if the slit function did not change slowly with ω.

In this study it is assumed that the change of the slit function with ω may be described by

$$\frac{\Delta\omega}{\Delta\omega_o} = \frac{\delta_1\omega}{\delta_1\omega_o} \tag{13}$$

where ω_o is the wave number of the line used to measure the slit function, and $\delta_1\omega$ and $\delta_1\omega_o$ are the theoretical effective band widths for 1 mm slits at wave numbers ω and ω_o, respectively. The latter two quantities are obtained from the dispersion of the prism material. Next a new slit function $\hat{g}$ is defined such that

$$\hat{g}\left(\frac{\omega' - \omega}{\Delta\omega}\right) = g(\omega' - \omega) \tag{14}$$

It is assumed that slit functions at different wave numbers bear a similarity, in addition to Eq. (13), given by

$$\hat{g}\left(\frac{\omega' - \omega}{\Delta\omega}\right) = \frac{\delta_1\omega_o}{\delta_1\omega}\,\hat{g}\left(\frac{\omega' - \omega_o}{\Delta\omega_o}\right) \tag{15}$$

where the factor $\delta_1\omega_o/\delta_1\omega$ has been included in the definition of $\hat{g}[(\omega'-\omega)/\Delta\omega]$; as in Eq. (11), this quantity will be normalized according to

$$\int_0^\infty \hat{g}\left(\frac{\omega' - \omega}{\Delta\omega}\right) d\omega' = 1 \tag{16}$$

at all wave numbers.

C. Apparent Absorption Coefficient

Realizable monochromators have a slit function of finite width, and, consequently, in absorption studies an apparent absorption coefficient $P_{\omega, ap}$ is measured instead of the true absorption coefficient P_ω. The same is true for emission studies. In Appendix A an expression is obtained for the radiant flux $\mathfrak{F}_e$ passing through the exit slit of a monochromator and resulting from emission by a homogeneous non-scattering medium of thickness $\mathfrak{L}$ focused on the entrance slit. If the medium is H_2O, Appendix A gives

$$\mathfrak{F}_e = F_\omega \int_0^\infty B^o_{\omega', g}\left(1 - e^{-P_{\omega'}\mathfrak{L}p_{H_2O}}\right) g(\omega' - \omega, \omega)\, d\omega' \tag{17}$$

where $B^o_{\omega', g}$ is evaluated at the temperature of the water vapor, and F_ω is a factor depending on the slit widths and wave number setting of the monochromator. For an ideal (but unattainable) monochromator, g becomes the Dirac delta function δ, so that

$$\mathfrak{F}_e = F_\omega B^o_{\omega, g}\left(1 - e^{-P_\omega \mathfrak{L} p_{H_2O}}\right) \tag{18}$$

Consequently, it is convenient to define an apparent absorption coefficient $\tilde{P}_{\omega, ap}$ for emission for more realistic cases where $g(\omega' - \omega, \omega) \neq \delta(\omega' - \omega)$. The defining equation is

$$\mathfrak{F}_e \equiv F_\omega B^o_{\omega, g}\left(1 - e^{-\tilde{P}_{\omega, ap} \mathfrak{L} p_{H_2O}}\right) \tag{19}$$

Comparing Eqs. (17) and (19) and neglecting the variation of $B^o_{\omega'}$ across the slit function,

$$\int_0^\infty \left(1 - e^{-P_{\omega'} \mathfrak{L} p_{H_2O}}\right) g(\omega' - \omega, \omega)\, d\omega' = 1 - e^{-\tilde{P}_{\omega, ap} \mathfrak{L} p_{H_2O}} \tag{20}$$

For absorption studies if the variation with ω' of the spectral steradiancy incident upon the water vapor is neglected, and the f-number of the optics is large,

$$\frac{\mathfrak{F}_e}{\mathfrak{F}_{e,o}} = \int_0^\infty e^{-P_{\omega'} \mathfrak{L} p_{H_2O}}\, g(\omega' - \omega, \omega)\, d\omega' \tag{21}$$

Comparing Eqs. (1) and (21),

$$\int_0^\infty e^{-P_{\omega'} \mathfrak{L} p_{H_2O}}\, g(\omega' - \omega, \omega)\, d\omega' = e^{-P_{\omega, ap} \mathfrak{L} p_{H_2O}} \tag{22}$$

Comparing Eqs. (20) and (22) and recalling Eq. (11), it is clear that the apparent absorption coefficients for both emission and absorption are equal, i.e.,

$$P_{\omega, ap} = \tilde{P}_{\omega, ap} \tag{23}$$

The integrated absorption coefficient a of the H_2O bands between 2700 cm^{-1} and 4550 cm^{-1} was calculated in the present study by the approximation

$$a \approx \int_{2700}^{4550} P_{\omega, ap}\, d\omega \tag{24}$$

whereas the exact expression is Eq. (3).

Equation (24) is equivalent to

$$a \approx -\frac{1}{\mathfrak{L}p_{H_2O}} \int_{2700}^{4550} \log\left[\int_0^{\infty} e^{-P_{\omega'}\mathfrak{L}p_{H_2O}}\, g(\omega' - \omega, \omega)\, d\omega'\right] d\omega \tag{25}$$

where the logarithm is to the base e. Equation (25) can be integrated only for specific forms of $P_{\omega'}$ and g and then only by numerical methods or series expansion. The error involved in the use of Eq. (24) or (25) is calculated in Section VC for a particular case.

D. Shock Tube

The shock tube consisted of a driver separated from the driven end by a single diaphragm and was designed with a reduction in tube cross-sectional area at the diaphragm. Spectroscopic measurements were made behind the reflected shock wave at the extremity of the driven end.

One-dimensional gas dynamics[25] is almost always used to calculate conditions behind the reflected shock wave, and the validity of this assumption has been verified by a number of investigators[26-29].

The initial temperature, pressure, and composition of the gas in the driven end of the shock tube are measured as well as the incident shock velocity. This enables the temperature, pressure, and chemically-frozen or chemically-equilibrated composition behind the reflected shock to be calculated, depending on which assumption is more realistic. These conditions obtain until the expansion wave from the driver or a reflected wave from the contact surface interferes.

The special case of a single-diaphragm shock tube with area change at the diaphragm section has been analyzed[30]. Utilizing Refs.(25) and (30), wave diagrams were constructed for the two sets of conditions used in the present study. No interferences were revealed by the wave diagrams for the 200 μsec time interval during which spectroscopic measurements were made behind the reflected shock wave.

The interaction of the reflected shock wave with the laminar boundary layer on the shock tube walls has been analyzed[31]. If the ratio of specific heats γ of the gas is not high enough, the boundary layer will separate. The ratio of specific heats in the present experiments was made sufficiently high by adding a large amount of Ar to the water vapor.

Behind the incident and reflected shock fronts there are rotational, vibrational, and chemical relaxations. Huber[32] measured relaxation times for pure water vapor which he believed were the vibrational relaxation times but which may have included some faster rotational relaxation. Based on Ref. (32), the rotational and vibrational relaxations should be too fast to observe in the present study.

The amount of gas composition change would have been negligible in all runs even if chemical equilibrium were attained.

E. Absolute Intensity Calibration and Emission Measurements

A schematic diagram of the blackbody, front-surface concave spherical mirror M1, 115 cps chopper, and monochromator entrance optics arranged for absolute intensity calibration is given in Fig. 2. The principle used was to make M1 of large enough diameter so every ray traced backwards from the monochromator prism and through the entrance slit to M7, the LiF lens, and M1 would terminate in the blackbody aperture. The chopper motor was below the infrared beam.

To image every point of the blackbody aperture as a point at the center of the shock tube, M1 should be a concave ellipsoidal mirror. However, it is shown in Appendix B that no error in steradiancy and, consequently, no error in the absolute intensity calibration will result from the aberrations concomitant with an off-axis concave spherical mirror as long as the aperture of the blackbody is sufficiently larger than the image of the entrance slit formed at the center of the shock tube.

To find the spectral steradiancy $B_{\omega', c}$ during absolute intensity calibration for any ray between the LiF lens and the window in Fig. 2, three losses were considered: the reflection loss at the window next to the blackbody, the absorption loss at the mirror M1, and the reflection loss at the single shock tube window. Since the beams passing through the windows were not collimated, interference effects arising from multiple reflections could be neglected. The effective transmission

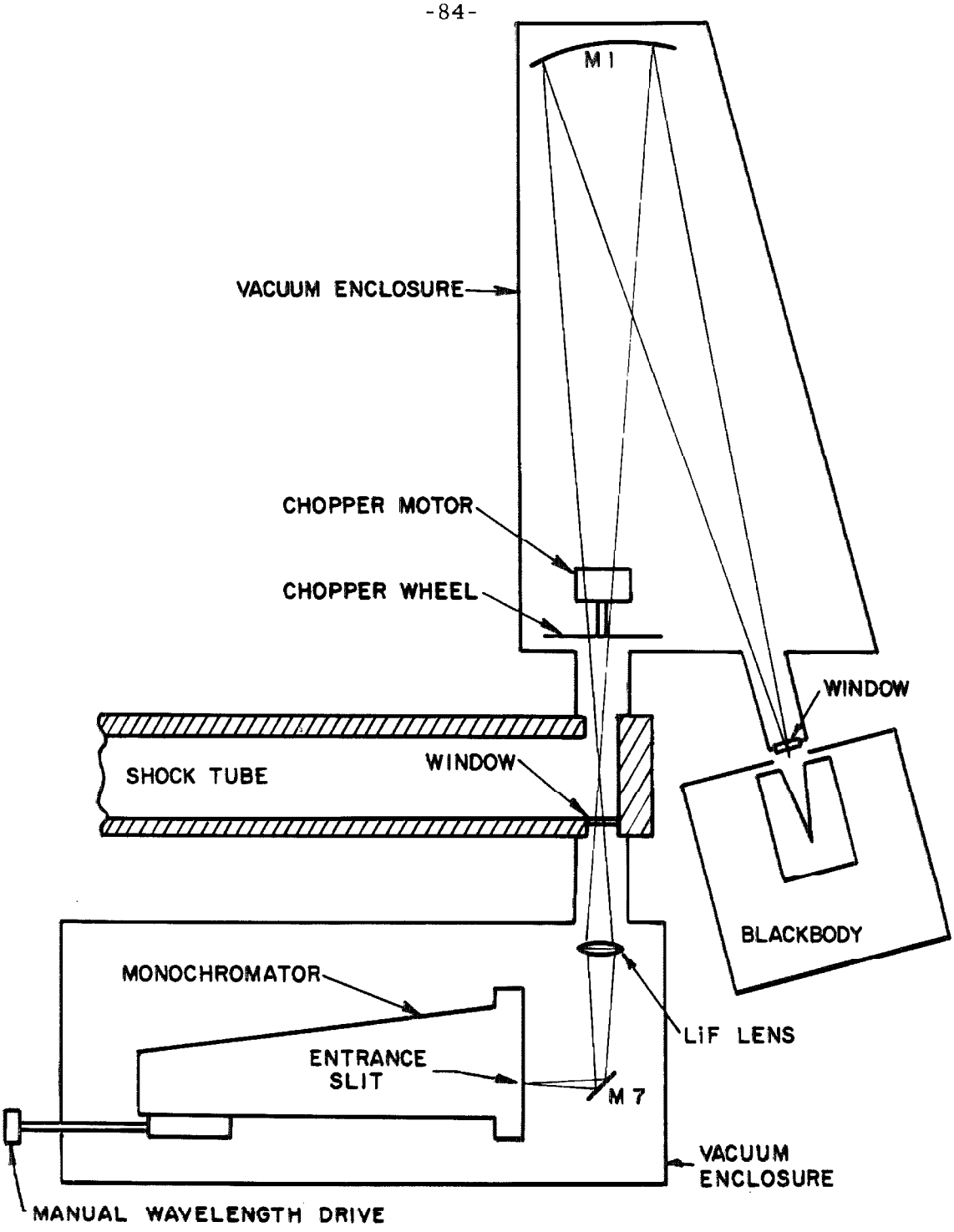

Fig. 2. Schematic diagram of blackbody infrared source and monochromator entrance optics arranged for absolute intensity calibration (top view). The temperature of the blackbody was determined with a thermocouple. The chopper motor was below the infrared beam.

$t_{\omega'}$ at wave number ω' of a window under such conditions is derived in Appendix C with the assumptions that the rays are nearly normal to the window and that the indices of refraction of the air on either side are equal. Because the index of refraction of air at 1 atm and room temperature is only about 1.0003, the assumption of equality of the indices of refraction is justified despite the pressure difference across the window near the blackbody. The other window had a vacuum on both sides.

The index of refraction of synthetic sapphire, of which the windows were made, was obtained from Ref. (33). The reflectance R_m of an evaporated aluminum film such as used on M1 in Fig. 2 was taken from Ref. (34). The quantity $B_{\omega', c}$ was then calculated from the relation

$$B_{\omega', c} = R_m t^2_{\omega'} B^{\circ}_{\omega', bb} \tag{26}$$

where $B^{\circ}_{\omega', bb}$ is the spectral steradiancy of the blackbody. Equation (17) becomes for the present case

$$\mathfrak{F}_{e, c} = F_{\omega} \int_0^{\infty} B_{\omega', c} g(\omega' - \omega, \omega)\, d\omega' \tag{27}$$

where $\mathfrak{F}_{e, c}$ is the radiant flux through the exit slit of the monochromator during absolute intensity calibration.

The quantity actually measured during absolute intensity calibration was the voltage output V_c of the preamplifier. Let W_{ω} be the sensitivity of the detector-preamplifier system in terms of, say, volts per erg of radiant energy per second. Then, if the variation

of $B_{\omega', c}$ over the width of the slit function is neglected, Eq. (27) yields

$$\frac{V_c}{B_{\omega, c}} = W_\omega F_\omega \tag{28}$$

If the responses of both the detector and the preamplifier are linear, then the products $W_\omega F_\omega$ depend only on wave number and slit widths and are the sole results of the absolute intensity calibration.

If the far wall of the shock tube were cold and black, as assumed in Appendix A, then, when the shock tube is full of hot H_2O vapor, Eq. (17) gives

$$V_c = W_\omega F_\omega \int_0^\infty t_{\omega'} B^o_{\omega', g} \left(1 - e^{-P_{\omega'} \mathfrak{L} p_{H_2O}}\right) g(\omega' - \omega, \omega)\, d\omega' \tag{29}$$

where V_e is the voltage output of the preamplifier due to the infrared radiation from the hot H_2O vapor, and $t_{\omega'}$ has been inserted to account for the reflection losses of the window between the shock tube and the monochromator.

Unfortunately, in order to make absorption measurements, it was necessary to replace the cold, black far wall of the shock tube with an additional window as shown in Fig. 3. As a result, there were multiple reflections not only within each shock tube window but also between the shock tube windows. In Appendix D the steradiancy $B_{\omega'}$ of a near-normal ray just outside one of the shock tube windows is derived assuming no radiation incident on the other window from outside the shock tube. For H_2O vapor the steradiancy becomes

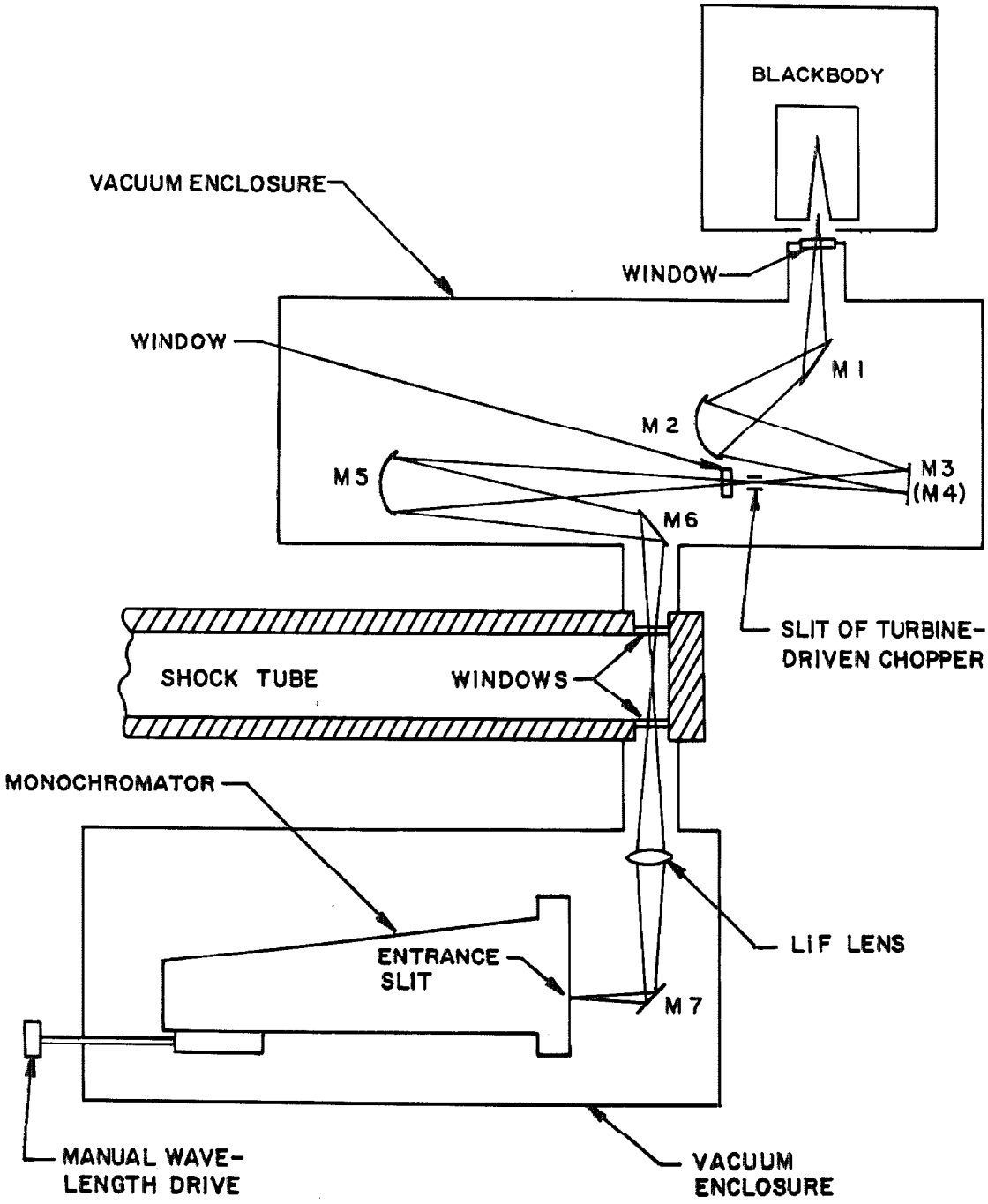

Fig. 3. Schematic diagram of blackbody infrared source and monochromator entrance optics arranged for runs (top view). Chopping the beam from the blackbody made possible simultaneous absorption and emission measurements in the shock tube.

$$\frac{B_{\omega'}}{B^{o}_{\omega', g}} = \frac{\left(1 - e^{-P_{\omega'} \mathfrak{L} p_{H_2O}}\right) t_{\omega'}}{1 - (1-t_{\omega'}) e^{-P_{\omega'} \mathfrak{L} p_{H_2O}}} \tag{30}$$

One additional correction is required; infrared radiation from the shock tube could be reflected successively by M6, M5, and the window between M5 and the chopper slit (see Fig. 3). The radiation reflected from the window could then be reflected by M5 and M6 and pass back through the shock tube and through the LiF lens to M7, which would reflect the radiation into the monochromator entrance slit. Because of the window between M5 and the chopper slit, the steradiancy of a ray between the lower shock tube window (in Fig. 3) and the LiF lens was increased by an amount $\delta B_{\omega'}$ given by

$$\frac{\delta B_{\omega'}}{B^{o}_{\omega', g}} = \frac{\left(1 - e^{-P_{\omega'} \mathfrak{L} p_{H_2O}}\right) t_{\omega'}}{1 - (1-t_{\omega'}) e^{-P_{\omega'} \mathfrak{L} p_{H_2O}}} R_m^4 (1-t_{\omega'}) t_{\omega'}^2 e^{-P_{\omega'} \mathfrak{L} p_{H_2O}} \tag{31}$$

where the value of R_m for M_5 and M_6 was taken equal to the value of R_m for rays with normal incidence. In deriving Eq. (31) multiple reflections between shock tube windows and the window near the chopper slit were neglected.

The total steradiancy $B_{\omega'} + \delta B_{\omega'}$ along a ray between the lower shock tube window (Fig. 3) and the LiF lens is obtained by adding Eqs. (30) and (31)

$$\frac{B_{\omega'} + \delta B_{\omega'}}{B^{o}_{\omega', g}} = \frac{\left(1-e^{-P_{\omega'}\mathfrak{L}p_{H_2O}}\right)t_{\omega'}}{1-(1-t_{\omega'})e^{-P_{\omega'}\mathfrak{L}p_{H_2O}}} \left[1 + R_m^4(1-t_{\omega'})t_{\omega'}^2 e^{-P_{\omega'}\mathfrak{L}p_{H_2O}}\right]$$

Of course, this applies only to rays that could be traced backwards to the window near the chopper slit; other rays when traced backwards terminated on room-temperature black surfaces because of the limited diameter of M5. For the latter rays Eq. (30) requires no modification.

In view of reflections from the three windows, Eq. (29) becomes

$$V_e = W_\omega F_\omega \int_0^\infty \frac{t_{\omega'} B^{o}_{\omega', g}\left[1-e^{-P_{\omega'}\mathfrak{L}p_{H_2O}}\right]\left[1+uR_m^4(1-t_{\omega'})t_{\omega'}^2 e^{-P_{\omega'}\mathfrak{L}p_{H_2O}}\right]}{1-(1-t_{\omega'})e^{-P_{\omega'}\mathfrak{L}p_{H_2O}}}$$

$$\times\, g(\omega' - \omega, \omega)\, d\omega'$$

where u is the average ratio of the solid angle of rays that could be traced backwards to the window near the chopper slit and traced forward to the monochromator prism, to the solid angle of <u>all</u> rays that could be traced forward to the monochromator prism. The quantity u had

a value of 0.977. The second term in the denominator is small compared to unity, as is the term in the numerator containing R_m^4. Consequently, little error results from taking both terms outside the integral sign and substituting $\tilde{P}_{\omega, ap}$ for $P_{\omega'}$, t_ω for $t_{\omega'}$, etc. Likewise, the variation of $t_{\omega'} B^o_{\omega', g}$ across the width of the slit function may be neglected. With the help of Eq. (20), V_e becomes

$$V_e = \frac{W_\omega F_\omega t_\omega B^o_{\omega, g} \left[1 + u R_m^4 (1 - t_\omega) t_\omega^2 e^{-\tilde{P}_{\omega, ap} \mathfrak{L} p_{H_2O}}\right] \left[1 - e^{-\tilde{P}_{\omega, ap} \mathfrak{L} p_{H_2O}}\right]}{1 - (1 - t_\omega) e^{-\tilde{P}_{\omega, ap} \mathfrak{L} p_{H_2O}}} \tag{32}$$

Equation (32) was used in all runs to find $\tilde{P}_{\omega, ap}$ from V_e, etc. The assumption of an infinite number of multiple reflections between shock tube windows made in deriving Eq. (32) was a good approximation because the diameter of the shock tube windows was much larger than the height of the entrance slit image in the shock tube. However, the change in the reflectivity $(1 - t_\omega)$ of the windows near their edges due to the cement on their backs was neglected.

From Eq. (1) the basic equation for absorption, neglecting multiple reflections, is

$$\frac{V_a}{V_{a,o}} = e^{-P_{\omega, ap} \mathcal{L} p_{H_2O}} \tag{33}$$

where the difference between L and $\mathcal{L}$ has been neglected, $V_{a,o}$ is the amplitude of the chopped signal at the output of the preamplifier with no H_2O in the shock tube, and V_a is the amplitude of the chopped signal with H_2O present in the shock tube. An analysis similar to that in Appendix D but for multiple reflections of the chopped infrared beam in the shock tube was performed, but the correction to Eq. (33) did not exceed 1% for the worst case and for most cases was much less. Such an analysis would be valid for a collimated chopped beam or for the central ray of an uncollimated beam normal to the windows, but, as is evident from Fig. 3, the beam was uncollimated, and all rays, except the central ray, had an angle of inclination to the windows. As a result, if the chopped beam underwent multiple reflections, it would soon reach a position where it could never reach the monochromator entrance slit. Therefore, Eq. (33) without any modification was used to find $P_{\omega, ap}$ for all runs.

III. EXPERIMENTAL FACILITIES

Every system used in Ref. (24) was either replaced or substantially modified. The experimental facilities will be described in detail below.

A. Shock Tube and Associated Measuring Apparatus

The shock tube was originally assembled by Lapp and is shown schematically in Fig. 4. The carbon steel driver was 188 cm long and had an inside diameter of 11.4 cm. It was evacuated with a Welch DuoSeal Cat. No. 1405 mechanical vacuum pump and was filled from commercial He bottles. The diaphragm consisted of from 3 to 5 sheets of 0.127 mm and 0.254 mm thick DuPont Mylar plastic which were burst by He pressure.

The driven section was 295 cm long and had a square cross section 8.25 cm by 8.25 cm inside. It was constructed from SAE 1040 seamless mechanical steel tubing. The far right-hand portion of the driven end is called the test section and is shown in Fig. 5. For flushing gas mixture through the driven end, a poppet valve shown in Fig. 5 was provided. The removable end plug containing the poppet valve was mild steel plated with electroless nickel. The valve body was brass, and the poppet itself was stainless steel. When closed, the end of the poppet was flush with the removable end plug. The ends of both the end plug and the poppet had one coat of DuPont No. 850-201 Teflon TFE-fluorocarbon resin primer and two coats of No. 851-205 Teflon TFE-fluorocarbon resin black enamel baked on to reduce adsorbed H_2O[35] and minimize reflected light. The central ray of the optical system passed 1 cm from the Teflon-coated surfaces. The two windows, like all other windows in the various optical systems used, were 0.32 cm thick Linde synthetic sapphire of superior internal quality. They were cemented in place with epoxy resin.

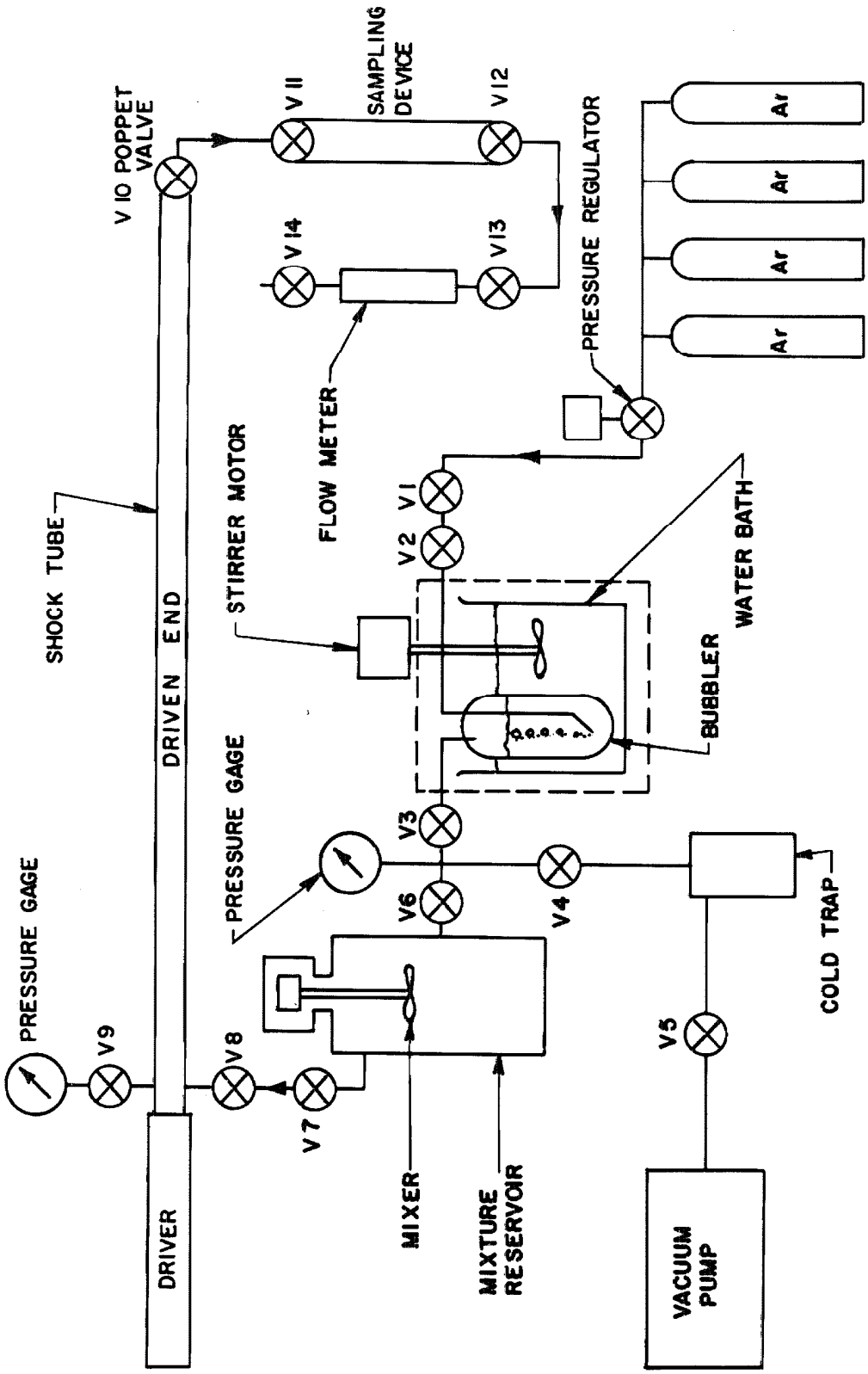

Fig. 4. Simplified schematic diagram of the shock tube and the gas-handling system. The Ar was saturated with H_2O in the bubbler, and the resulting mixture was flushed through the shock tube continuously for 3 hours prior to firing.

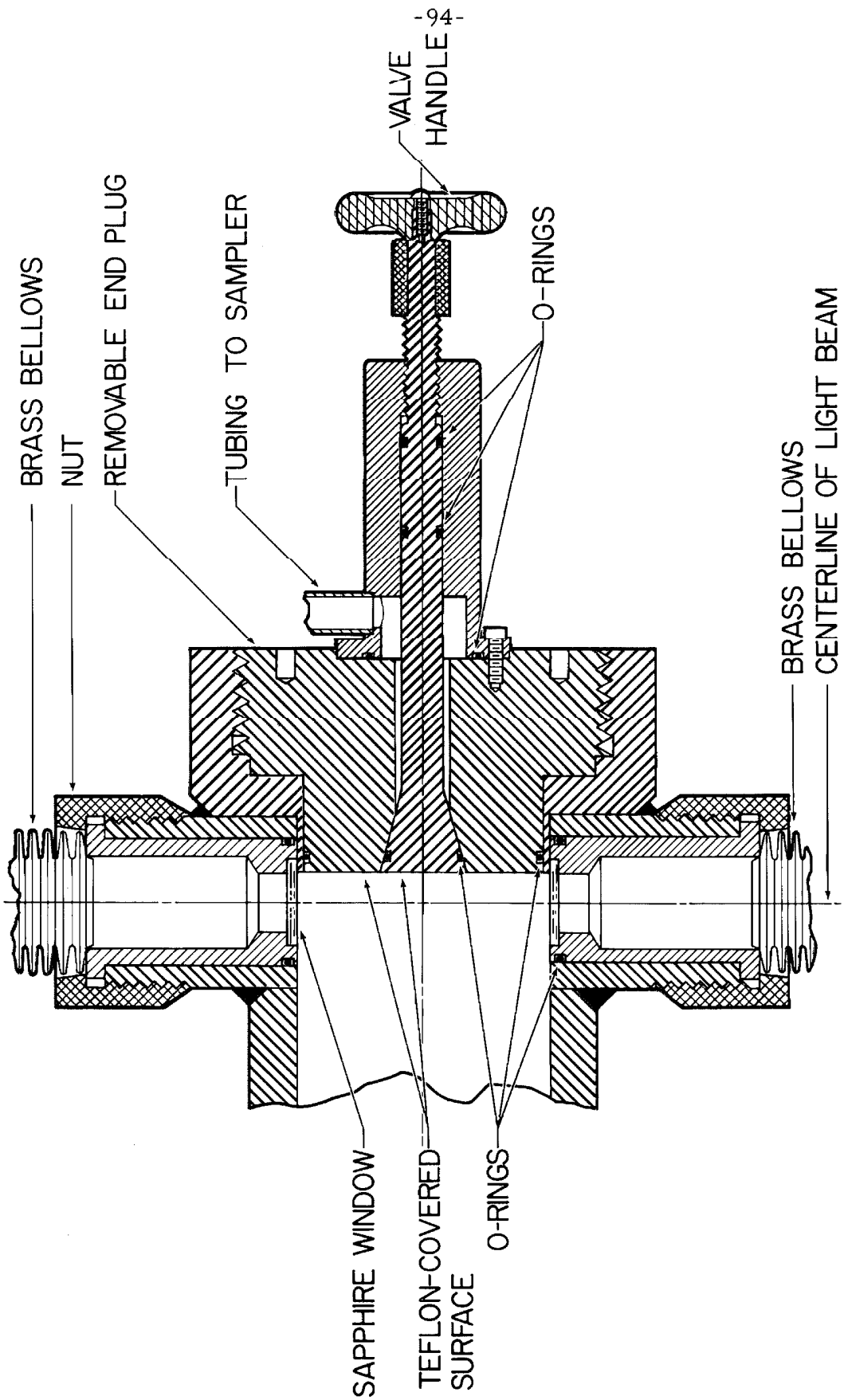

Fig. 5. Cross section of shock tube test section showing flush windows in sides and flush poppet valve at end. The valve was opened for flushing the shock tube with H_2O-Ar gas mixture but was closed before firing the shock tube (top view; half size).

The vacuum system to evacuate the driven end consisted of a Consolidated Vacuum Type MCF-60 oil diffusion pump and a Kinney Model KC-8 mechanical vacuum pump. Circle Seal 9200 series plug shutoff valves were used here and in most other cases in the experiment where a shutoff valve was required. The vacuum was measured with a Consolidated Vacuum Type PHG-09 Philips gauge and Consolidated Vacuum Type GP-140 Pirani Gauge. The leak rate of the driven end of the shock tube never exceeded 5 μHg per hr.

Shock wave velocity was measured by the system shown in Fig. 6, which was based on detection of the change of resistance of thin-film heat-transfer gages at the time of shock wave passage. The thin film gages were made by sputtering and baking platinum on to a block of Pyrex glass masked off so that only a thin strip of platinum was produced. Each block was cemented into a brass holder with epoxy resin, and the holder was inserted into the side of the shock tube and sealed with an O-ring. The entire assembly was flush with the inside of the shock tube, and each gage had a resistance of about 70 ohms. The spacing between the two gages was measured with a vernier caliper and was 30.45 cm. Direct current for the thin-film gages was supplied by the battery circuits described in Ref. (36). The output of the thin-film gages went to a two-position selector switch. When set on shock velocity, the switch connected the upstream (or left) gage to the "start" amplifier and the downstream gage to the "stop" amplifier.

The "start" and "stop" amplifiers were Acton Laboratories Type 500A amplifiers modified as shown in Fig. 7 to eliminate the

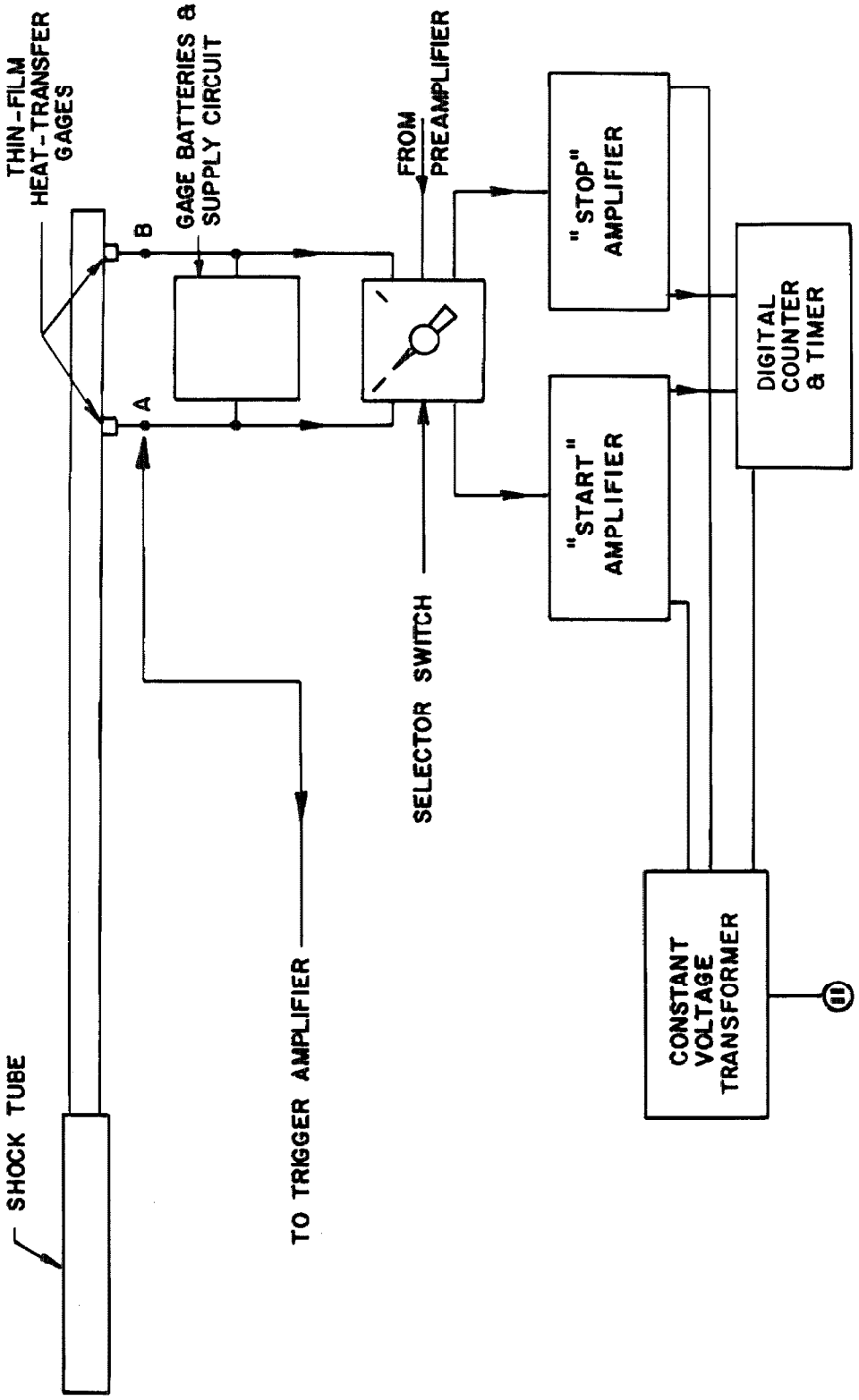

Fig. 6. Block diagram of circuit for measuring shock wave transit time between gages A and B. In addition, by resetting the selector switch to connect the preamplifier (not shown) to the "start" amplifier, it was possible to measure the frequency of the turbine-driven chopper.

V2
6CB6

(V1 REMOVED FROM AMPLIFIER)

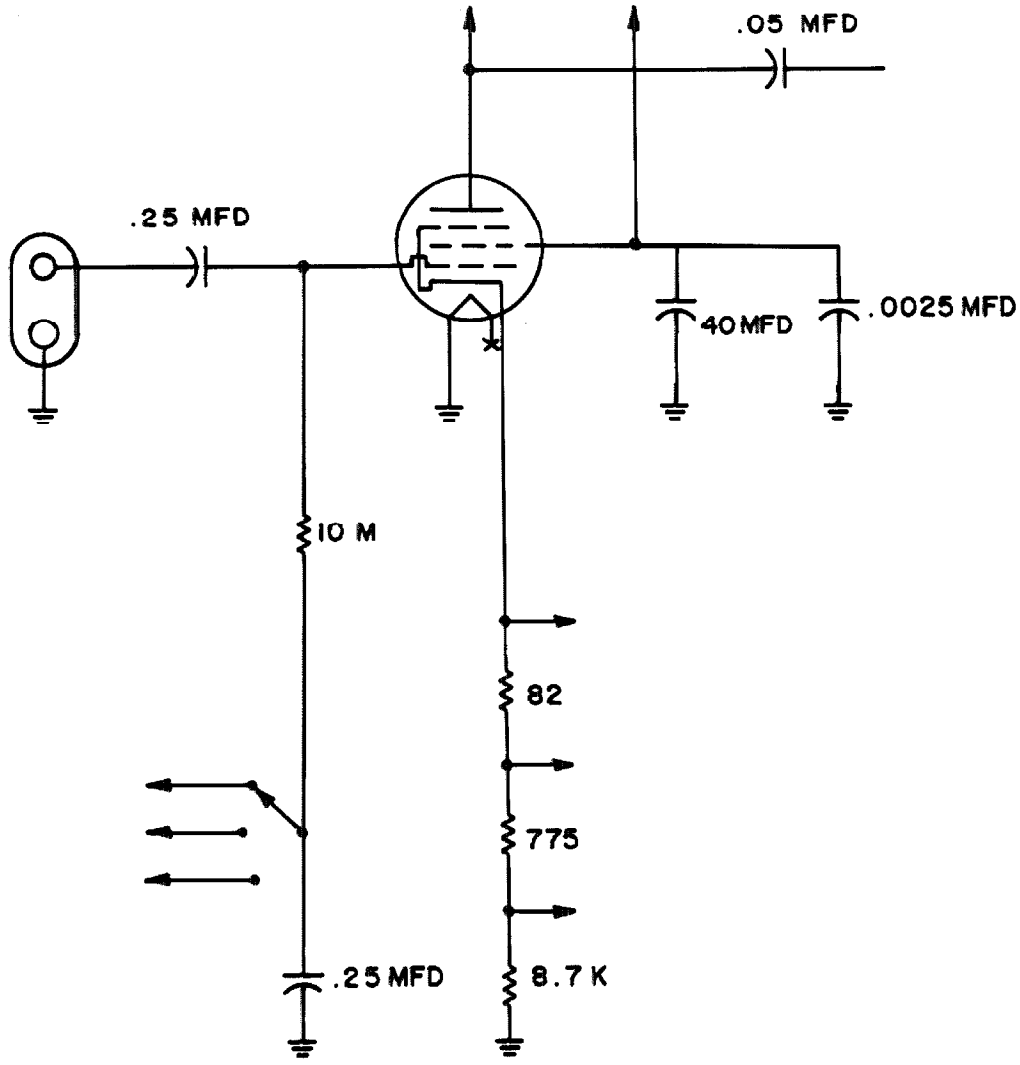

Fig. 7. Schematic diagram of modified input to Acton Type 500-A amplifier to minimize noise. The unnecessary first stage of the amplifier was removed.

noise from the high impedance input stage not needed for a thin-film gage. In addition, C26 was removed and a 22,000 ohm resistor installed in parallel with the output. A Sola constant voltage transformer was installed in the power line to minimize noise in the amplifiers due to line voltage fluctuations. Each amplifier was set for a gain of 1000 and connected to the "start" and "stop" channels, respectively, of a Berkeley Model 7360 Universal Eput and Timer which measured the time required for the shock wave to pass from the upstream thin-film gage to the downstream thin-film gage.

The temperature of the shock tube was measured with a mercury-in-glass thermometer placed against the test section. The thermal resistance between the thermometer and the test section was reduced with Apiezon Q Sealing Compound.

B. Optical System

The three different arrangements of the optical system are described in this section. They are the configurations for shock tube runs, absolute intensity calibrations, and slit function measurements.

The arrangement for shock tube runs is shown in Figs. 3, 8, and 9. To minimize absorption by atmospheric H_2O and CO_2 along the light path, the optics were enclosed in two vacuum enclosures, shown in Fig. 3, consisting of welded aluminum boxes with 1.27 cm thick walls and Lucite covers. The two boxes were evacuated to 65 μHg or less by a common Welch DuoSeal Cat. No. 1402 mechanical vacuum pump.

Infrared radiation was produced by an Infrared Industries

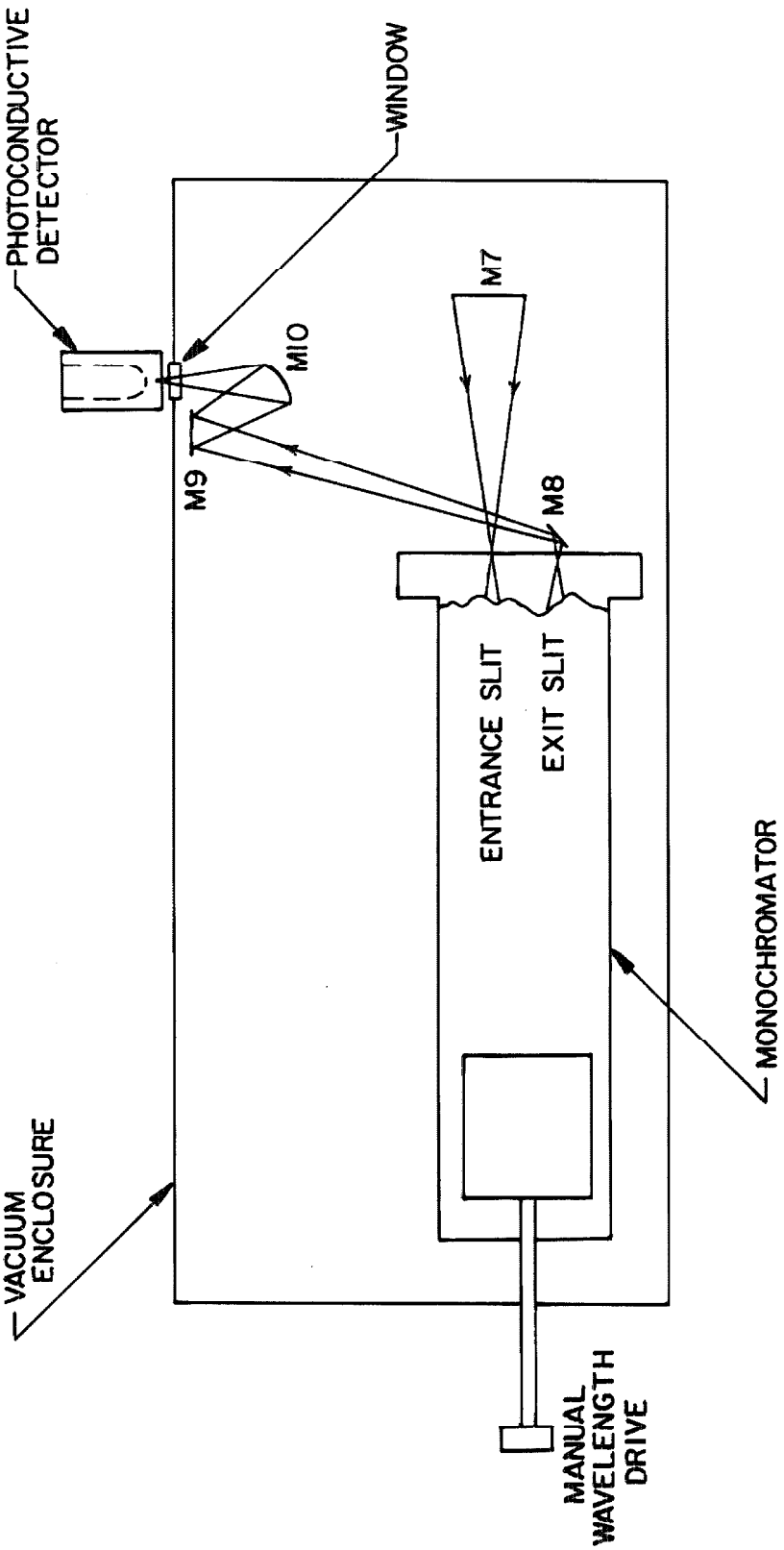

Fig. 8. Schematic diagram of monochromator exit optics and detector (side view). Infrared from the exit slit was focused on a liquid-N_2-cooled gold-doped-germanium detector.

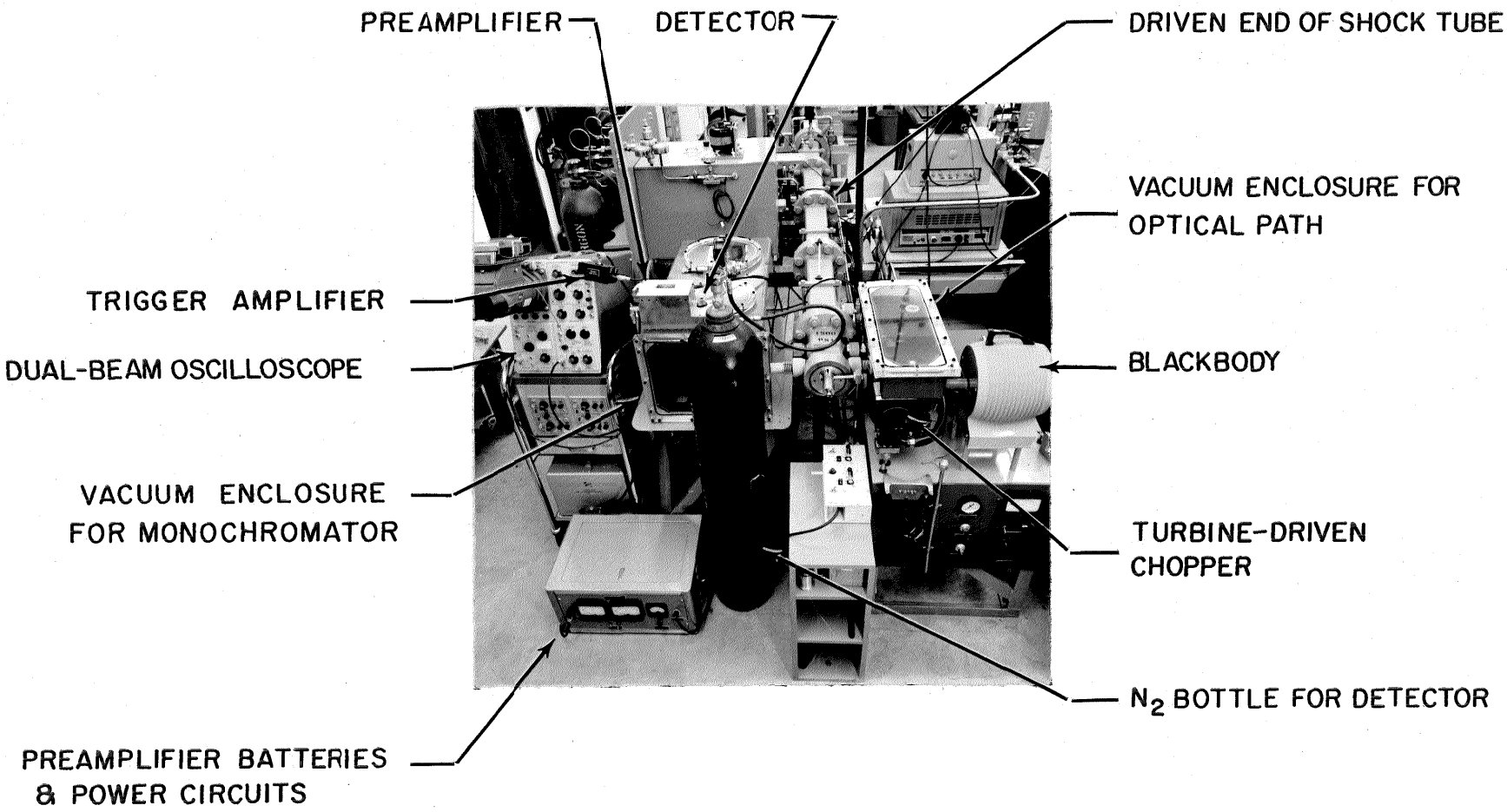

Fig. 9. Photo of the optical arrangement used for shock tube runs. Infrared radiation from the blackbody was chopped by the turbine-driven chopper and focused on the center line of the shock tube. A fraction of this infrared and also infrared emission from inside the shock tube was focused on the monochromator, was dispersed, and was then focused on the detector.

Model 406 Blackbody Radiation Source consisting of a heated, insulated cylinder of oxidized stainless steel with a 20^{o} conical hole part way into one end. The cylinder was heated by alternating current from a solid-state feedback controller which kept the temperature at about 1260 ^{o}K with no more than 2 ^{o}K drift during a run.

The radiation from the blackbody passed through a sapphire window and was reflected from M1 to M2, which focused it on the slit of a turbine-driven chopper located below the vacuum enclosure. The light path between M2 and the slit was reversed by means of a flat mirror M3 and another flat mirror M4 below M3. The chopped beam then passed through a sapphire window back into the vacuum enclosure and to M5, which focused it on the center of the shock tube test section with the help of M6. An LiF lens then focused the beam on the entrance slit of a Beckman IR2 monochromator.

The Beckman IR2 monochromator is a single-pass instrument employing a Littrow mounting. The instrument used had a mask just in front of the entrance slit to restrict the height of the beam entering the instrument and had an auxiliary fixed slit just behind the furnished entrance slit to restrict the entrance slit opening to a maximum of 1 mm, corresponding to the width of the image of the chopper slit. This was necessary in order to have the same $g(\omega' - \omega, \omega)$ for both emission and absorption measurements. An LiF prism was used in the IR2, and wavelength adjustment was accomplished by means of a right-angle gear box, universal joints, a Consolidated Vacuum rotary vacuum seal, and a knob, as indicated schematically in Figs.3 and 8.

Referring to Fig. 8, the beam from the exit slit was directed by M8 and M9 on to M10, which focused it through a sapphire window on to the detector. A photo of the optical arrangement used for shock tube runs is given in Fig. 9.

The turbine-driven chopper mentioned above warrants further description, so a cross section is given in Fig. 10. The basic unit was constructed by Hooker[37] by modifying an AiResearch aircraft turboblower. A single-stage radial-inflow turbine on one end of the shaft drove a 7 cm diameter aluminum alloy wheel on the other end, the shaft being mounted on precision ball bearings. The wheel had 90 slots cut in its circumference to chop the infrared beam and was enclosed in a steel housing in case it failed at high speed. The beam from M3 passed through a sapphire window, was deflected by M4, passed through the chopping wheel, and came to a focus at a single fixed slit the same size as the slots in the wheel. The beam then passed through another sapphire window to M5.

The turbine was driven from a shop air line of about 8 atm pressure through the turbine air supply system shown in Fig. 11. The air passed through a coarse filter and trap to remove solids and liquids, respectively, and then through a silica gel dryer to a Norgren Type 11-008-009 dome-loaded pressure regulator to provide constant turbine speed. The dome was loaded by a Norgren Type 11-018 precision pressure regulator acting as a pilot. Control of turbine speed was achieved with two Hoke throttle valves in parallel. The flow of dry air then went to the plenum chamber shown in Fig. 10 and to the

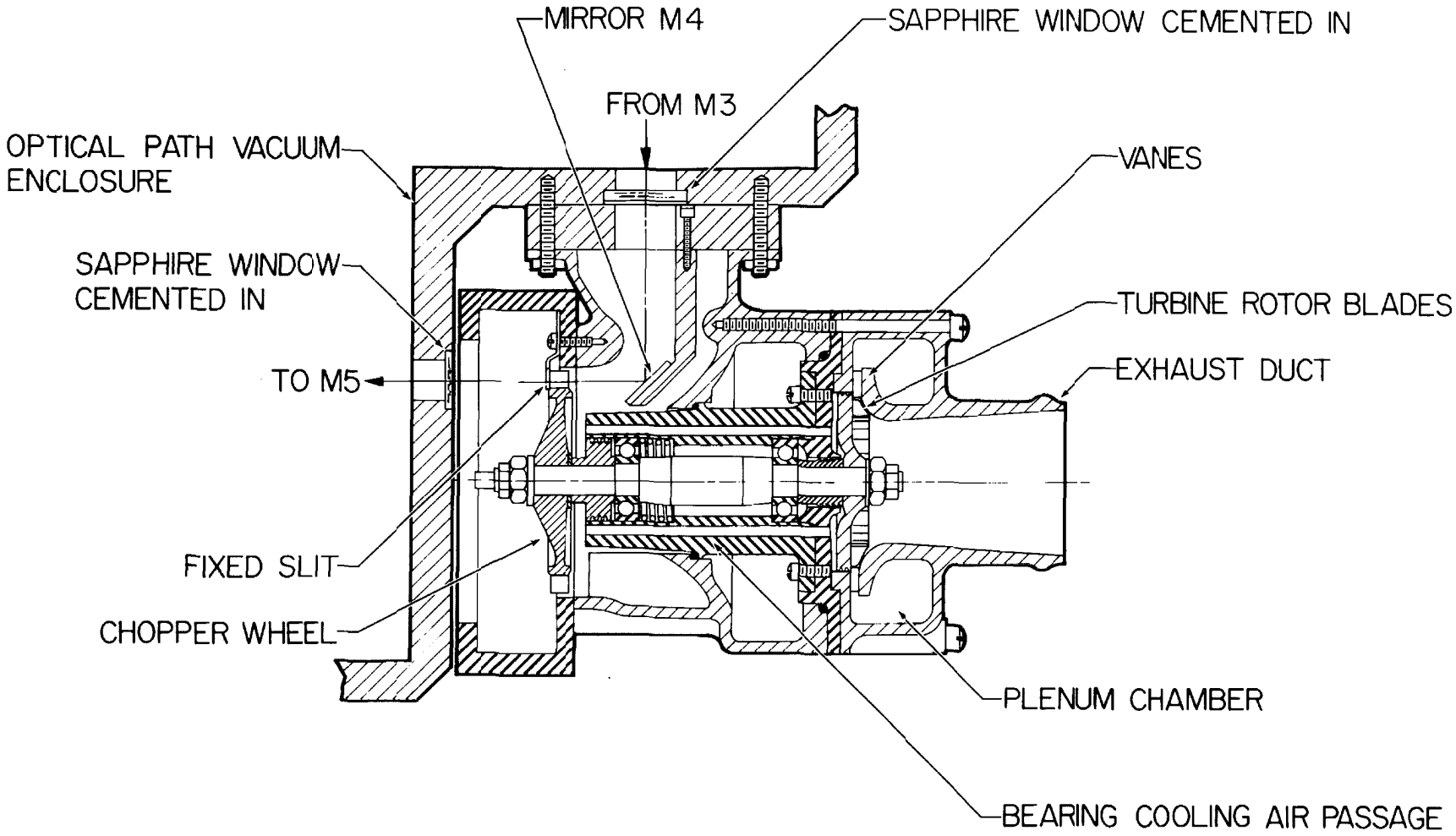

Fig. 10. Cross section of turbine-driven chopper showing 90-slot aluminum alloy chopper wheel, which interrupted (or chopped) the infrared radiation from mirror M3 at a 60 kc rate. The single-stage radial-inflow turbine was driven at 40,000 rpm by dry compressed air from the plenum chamber (side view; half size).

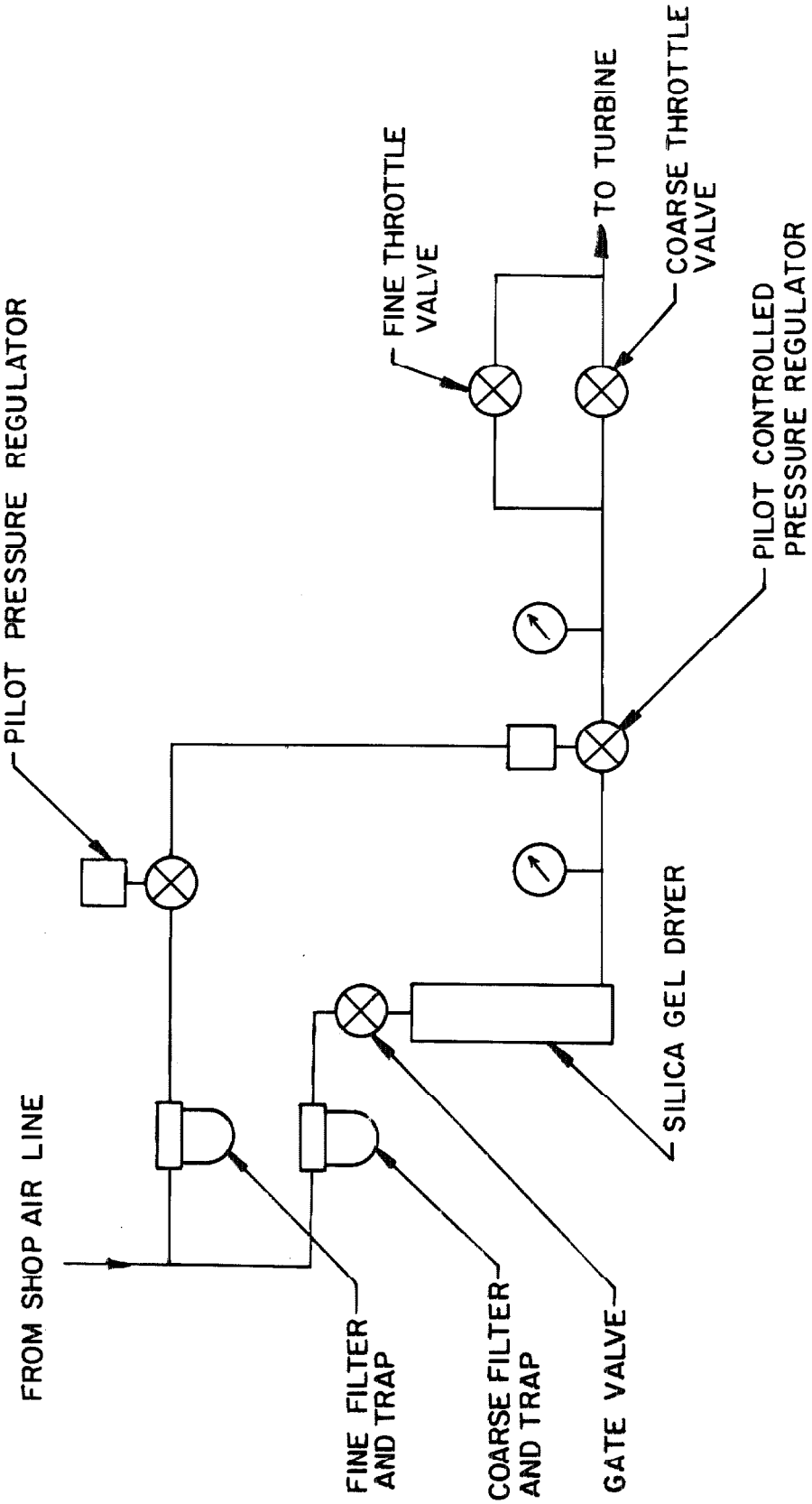

Fig. 11. Schematic diagram of turbine air supply system, which furnished close automatic regulation of turbine speed.

turbine inlet vanes. It there split into two streams, the principal stream flowing through the turbine rotor and out the exhaust to the atmosphere, and the other smaller stream flowing through the bearing holes, around the chopper wheel, and out the gap between the steel housing and the vacuum enclosure. The smaller stream of dry air thereby flushed atmospheric water vapor from the optical path.

The rotating assembly was dynamically balanced and run at about 40,000 rpm to provide 60 ± 0.9 kc chopping frequency.

An important factor in the success of the present experiments was the mechanical design of the optical system. All mirrors were secured with a threaded ring or epoxy cement, and practically all components were fitted with alignment pins in reamed holes or shoulder cap screws in precision slots. To prevent vibration from the diaphragm burst misaligning the optics, it was found necessary to mount both vacuum enclosures on steel tables fastened to the concrete floor and connect the vacuum enclosures to the shock tube test section by brass bellows, as shown in Fig. 5. The inside of both vacuum enclosures was lacquered dull black to minimize stray infrared radiation.

Equally important was the optical alignment procedure, which utilized a number of insertable alignment targets, each consisting of an India ink cross on frosted glass or on a block painted flat white. To find the proper distance between the monochromator entrance slit and M7, the monochromator was moved back and forth on a slide until the image of the chopper slit came to a focus on the plane of the entrance slit, as determined by eye with visible light. Unfortunately,

the focal length of the LiF lens in Fig. 3 varied with wave number, so the monochromator was then slid to a new position calculated to bring the image of the chopper slit into the plane of the entrance slit at 3704 cm^{-1}. In this calculation the index of refraction of vacuum grown LiF determined by Tilton[38] was used. After alignment it was found that the signal due to the chopped beam was independent of the degree of vacuum in either vacuum enclosure provided that air was transparent at the set wave number, thus indicating that the system was not misaligned by atmospheric pressure on the vacuum enclosures.

If the turbine-driven chopper did not shut out all infrared from the blackbody when the chopper was in its closed position, there would be an error in emission measurements. To investigate this, a second chopper was temporarily placed between the turbine-driven chopper slit and M5. With the blackbody and second chopper operating, the turbine shaft was then rotated slowly by hand, and it was found that the turbine-driven chopper did indeed shut out all infrared from the blackbody.

The arrangement for absolute intensity calibration is shown in Figs. 2 and 12 and was discussed briefly in Section IIE. The manufacturer specified that the blackbody had an emissivity of 0.99 ± 0.01, and this was checked by comparing the reading from a recently-calibrated Leeds and Northrup optical pyrometer aimed directly at the blackbody with the output of a platinum/platinum-10% rhodium thermocouple installed in the stainless steel cylinder of the blackbody. The cold junction of the thermocouple was put in an ice bath in a Dewar

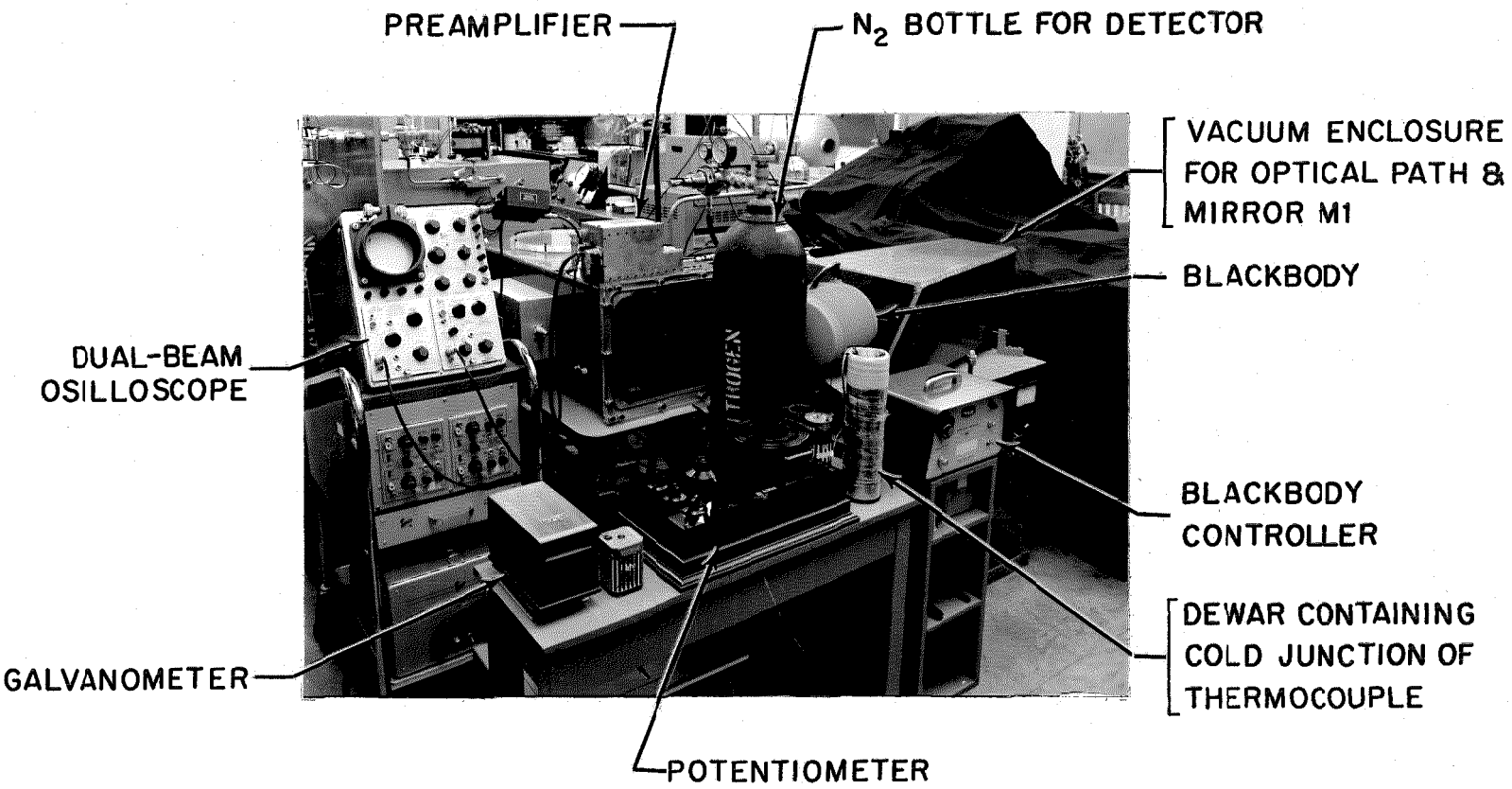

Fig. 12. Photo of the arrangement used for absolute intensity calibration of the optical and electronic system. The standard is a blackbody containing a thermocouple.

and the output was read on a Leeds and Northrup Type K potentiometer with Leeds and Northrup Cat. No. 2420D galvanometer as shown in Fig. 12. The maximum rated aperture of the blackbody was 1.52 cm, but no stop was used to reduce the 2.54 cm diameter of the hole. However, the region of the blackbody hole actually used for absolute intensity calibration had a maximum dimension less than 1.52 cm.

From the blackbody the infrared radiation passed through a sapphire window into the vacuum enclosure made of welded 1.27 cm aluminum plates, as shown in Figs. 2 and 12. The enclosure was open to the shock tube, and the two were pumped to 75 μHg or less during calibration. Mirror M1 was front-surfaced aluminum on glass and was kept in a vacuum when not in use to minimize oxidation of the aluminum.

The condition of the mirror was checked by aiming the optical pyrometer at the image of the blackbody seen in the mirror and measuring the brightness temperature of the image. The pyrometer operated at 15,000 cm^{-1}. At that wave number the calculated value of $t_\omega R_m$ of the sapphire window and the mirror, using values from the literature[33, 34], was 0.776 (see Section IIE for the method used). Comparing the measured steradiancy of the image with the blackbody steradiancy corresponding to the blackbody temperature, the measured $t_\omega R_m$ was 0.790, which agreed with the calculated value within the experimental error.

The chopper consisted of a 3450 rpm shaded-pole motor with a Micarta hub attached to it and a two-bladed aluminum chopper wheel attached to the hub. The Micarta hub reduced the heat transfer from the hot motor to the chopper wheel. As a further precaution to cool

the chopper wheel and thereby minimize infrared radiation from it, the side facing M1 was polished, and the side facing the shock tube was lacquered dull black. The entire inside of the vacuum enclosure was also lacquered dull black to minimize stray infrared.

In aligning M1 it was found that if alignment was attained without a vacuum in the vacuum enclosure and a vacuum then applied, misalignment would result due to the distortion of the vacuum enclosure by atmospheric pressure. Alignment with a vacuum applied was obtained by a trial and error process.

Measurement of the slit function of the IR2 met with difficulty. Preliminary work showed that of the sources of infrared spectral lines available in the laboratory, only a Central Scientific No. 87215 He Geissler tube had a strong line at a wave number less than 5000 cm^{-1}. When this tube was used in place of the blackbody in Fig. 3 with the rest of the optical and electronic systems unchanged, the strong He line at 4859 cm^{-1} was not even detectable due to the noise from the detector, indicating a need to average the signal over a longer time. This was accomplished with the completely different detection and electronic system shown in Figs. 13 and 14.

Basically, the final arrangement for slit function measurement involved the He Geissler tube, a 10 cps Beckman IR2 chopper and synchronous rectifier, the turbine-driven chopper in a static condition with the slit and a slot lined up to pass infrared, the existing run optics and monochromator, a PbS detector, and a tuned 10 cps Beckman IR2 amplifier. The Geissler tube was supplied with 2600 v AC

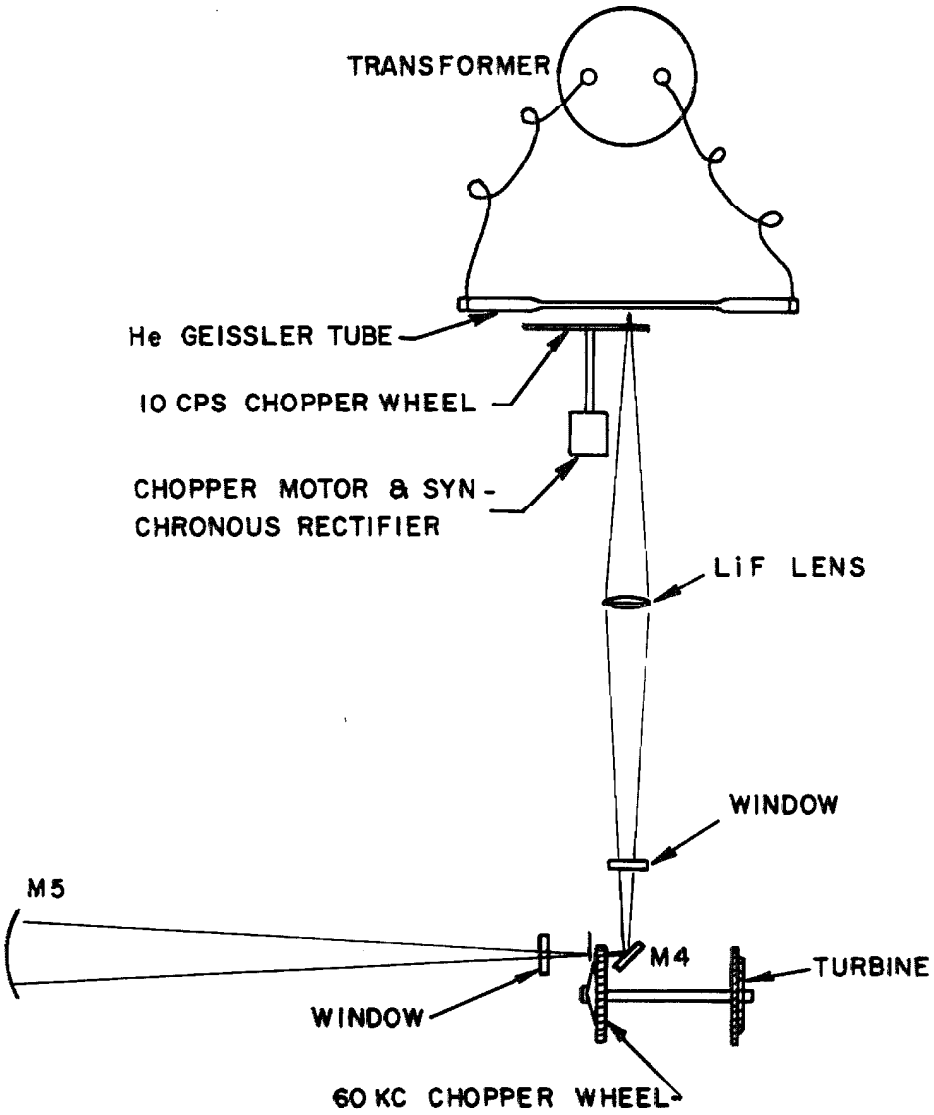

Fig. 13. Schematic diagram of Geissler tube, 10 cps chopper, and optics used for slit function measurements (side view). The turbine-driven chopper was not used and was positioned so the maximum amount of infrared passed through its slit to the monochromator.

Fig. 14. Photo of the arrangement used for measuring the slit function of the IR2 monochromator utilizing monochromatic radiation from a He Geissler tube.

from a Central Scientific No. 87208 transformer, which in turn was supplied 60 vac from an adjustable autotransformer. Radiation from the Geissler tube passed through the 10 cps chopper and was focused by an LiF lens on to the plane of the turbine-driven chopper slit. The beam then traversed the existing run optics and monochromator and was focused on an uncooled PbS detector of unknown origin. The monochromator vacuum enclosure was evacuated, but the vacuum enclosure containing M1, M2, M3, M5, and M6 was open to the atmosphere.

Lead sulfide detectors generally have flat spectral response to infrared of wave numbers near the 4859 cm^{-1} of the He line [39]. The output from the detector was amplified by the IR2 amplifier and applied to the synchronous rectifier on the same shaft as the 10 cps chopper. This gave a direct current proportional to infrared intensity, which was averaged over 32 sec by an IR2 amplifier circuit and then was applied to a 0-25 μamp Simpson Model 27 meter.

C. Infrared Detection Electronics for Runs

A block diagram of the circuits for detecting and measuring infrared is given in Fig. 15. The signal from a photoconductive detector was amplified by a preamplifier with two outputs. One output was applied directly to the upper beam of a dual-beam oscilloscope, whereas the other was filtered before application to the lower beam in order to eliminate the step function corresponding to infrared emission from the shock-heated H_2O.

The detector was a Westinghouse Type 812 gold-doped ger-

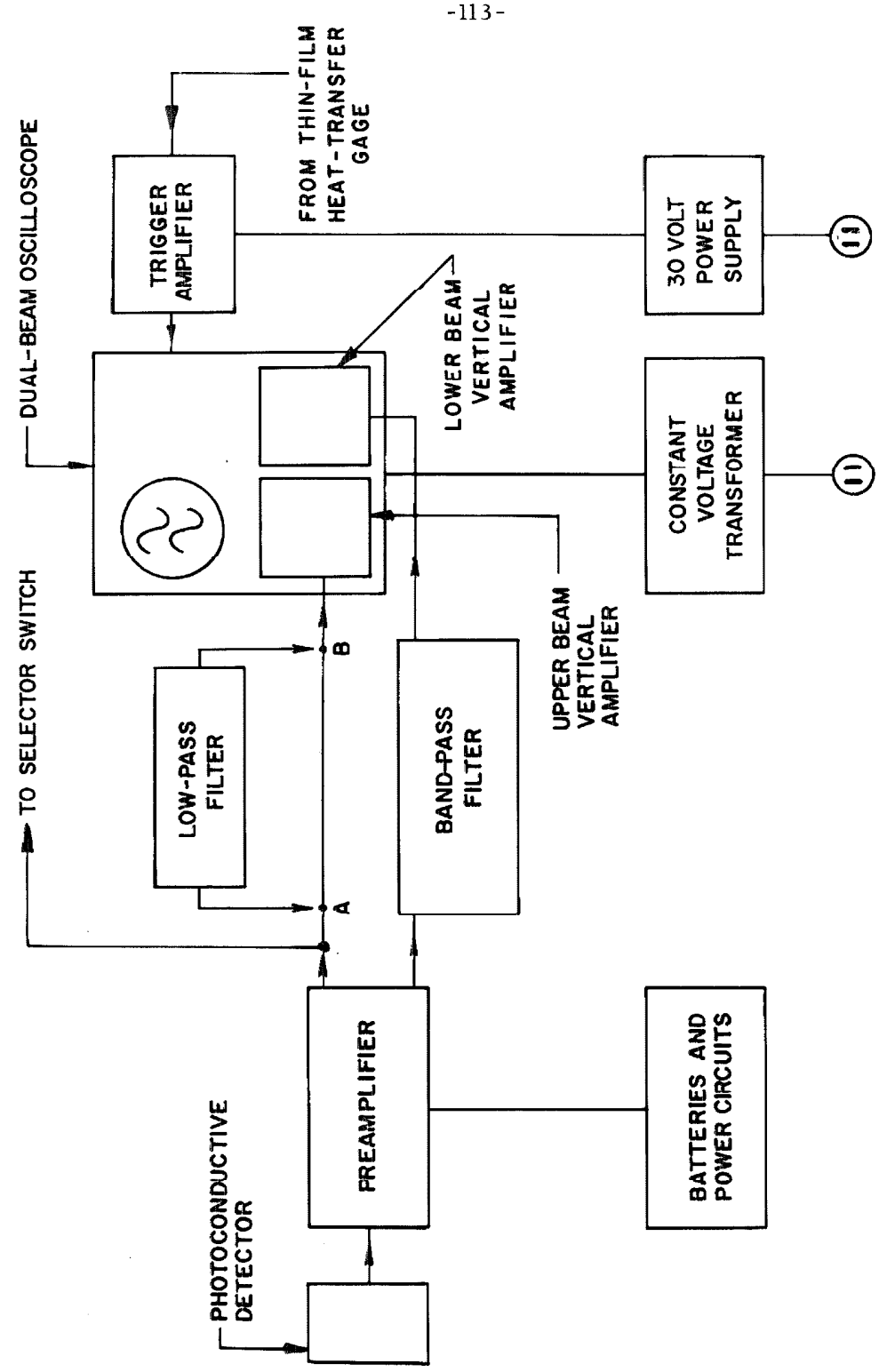

Fig. 15. Block diagram of circuits for measuring infrared radiation. The preamplifier provided two output channels. The upper channel was used primarily for infrared emission measurements. Use of the lower channel for absorption measurements was facilitated by the band-pass filter, which passed only the 60 kc absorption signal.

manium photoconductive cell with a maximum specified time constant of 0.5 μsec and slowly varying spectral sensitivity from 1200 cm^{-1} to 5500 cm^{-1}. It was equipped with a Dewar for cooling with liquid nitrogen and a sapphire window. In order to reduce bubble noise, the inside of the Dewar was packed with 1 cm^3 of powdered tungsten and a 0.5 cm plug of copper wool. To prevent atmospheric condensation on the window and terminals, three jets of dry N_2 gas were directed at the window and the two terminals respectively.

The preamplifier was specifically designed to operate with the high impedance detector, and its schematic diagram is shown in Fig. 16. Terminal 2 at the bottom provided filtered bias current for the detector. The signal from the detector was applied to an anode follower (6CB6) the output of which was applied to a negative-feedback amplifier with a gain of 10. In the negative-feedback amplifier the two 6AK5's were voltage amplifiers, and half a 6CG7 was a cathode follower (the upper one in the diagram). The negative feedback was obtained from the output of the upper cathode follower and passed through a phase-shifting circuit which improved the stability of the amplifier. The output of the upper cathode follower not only was applied directly to the upper beam vertical amplifier of the oscilloscope and to the feedback circuit but also was applied to the grid of a second cathode follower in the lower right of Fig. 16. This cathode follower provided an isolated output for the band-pass filter.

Among the design objectives for the preamplifier were getting the preamplifier noise level below the detector noise level and minimizing microphonic response. The former was accomplished by

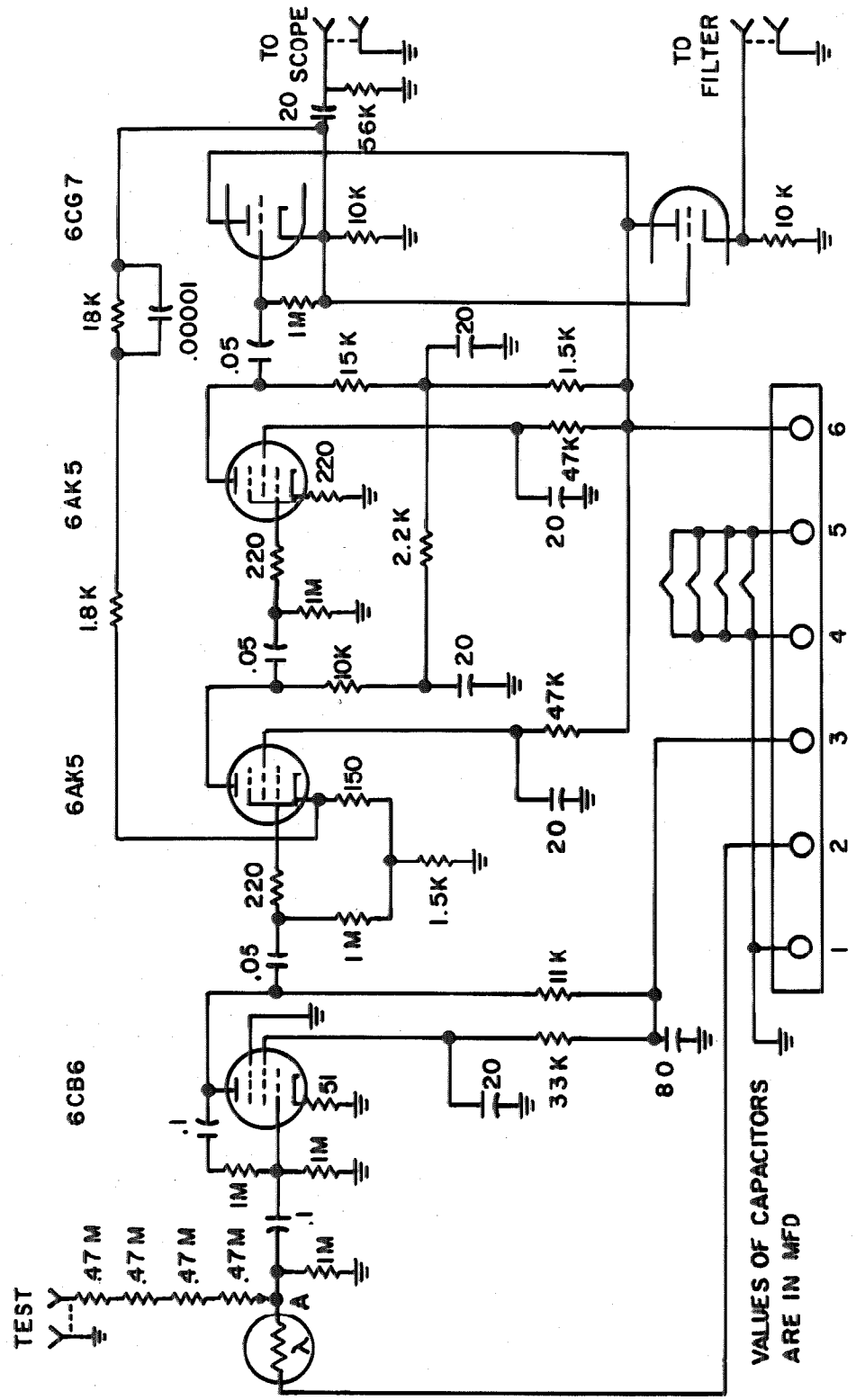

Fig. 16. Schematic diagram of photoconductive detector and preamplifier circuits. Due to negative feedbacks, the preamplifier had very stable gain. The battery and power circuits are given in Fig. 17.

using Corning tin oxide film resistors in the detector bias circuit, anode follower, and input to the first 6AK5, while the latter was achieved by building the preamplifier on a heavy length of aluminum channel and mounting this on four Lord rubber shock mounts.

The preamplifier battery and power circuits are shown in Fig. 17. Bias current for the detector was furnished by a 67.5 v dry battery and was measured by a 0-25 μamp meter. Adjustment to 15 μamp was accomplished with a carbon rheostat. A 225 v bank of dry batteries supplied plate and screen voltages for the preamplifier, while a 6 v storage battery furnished heater voltage.

Both the frequency response and linearity of the unfiltered preamplifier channel with output from the upper cathode follower in Fig. 16 were investigated. This was achieved by disconnecting the detector at point A and connecting four 470,000 ohm resistors and an oscillator in series with it. The band pass of the preamplifier extended from 150 kc to far enough below 20 cps that a more-or-less square 115 cps wave form could be amplified with negligible distortion of the top and bottom of the wave form (see Fig. 18). The rise time was 4 μsec. The channel was linear up to 35 v peak-to-peak output. Due to the negative feedbacks applied to all tubes, the gain was constant over wide ranges of plate and heater voltages.

In making absorption measurements the ratio of signal amplitudes with and without H_2O in the optical path varied from 0.72 to 1.00. From Eq. (33) it is then clear that any small errors in signal amplitude could cause large errors in $P_{\omega, ap}$. Significantly, it had been observed that a dual-beam oscilloscope of the type used had up to 6%

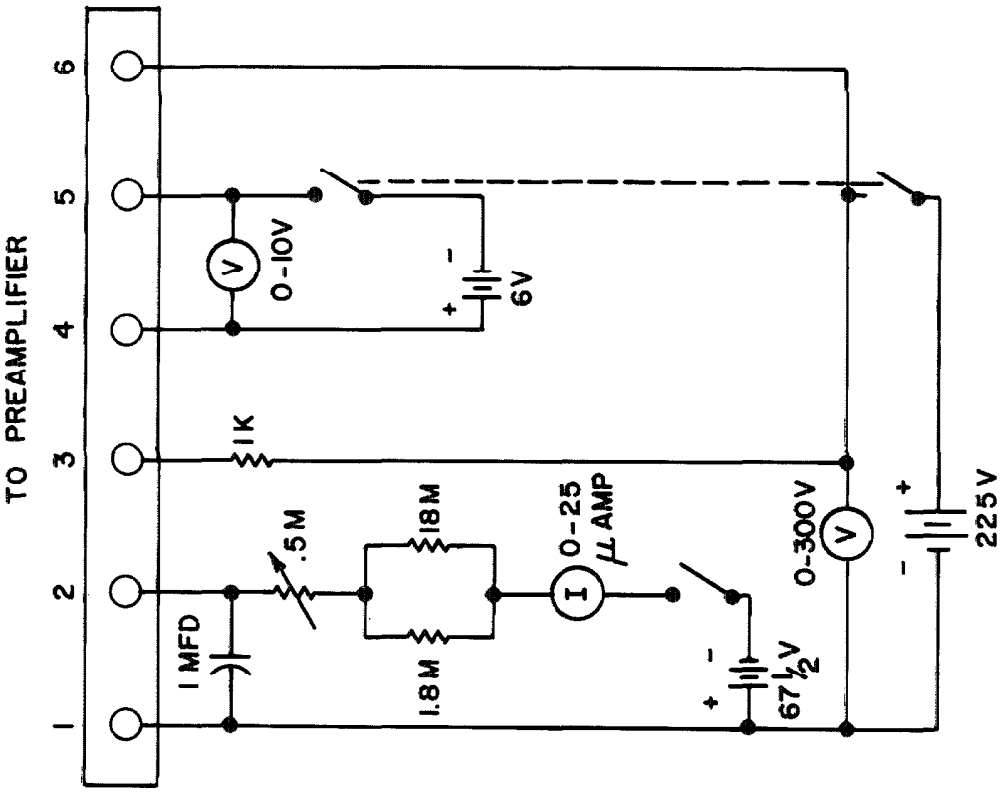

Fig. 17. Schematic diagram of battery and power circuits for the preamplifier in Fig. 16. The rheostat was provided for adjusting the detector bias current.

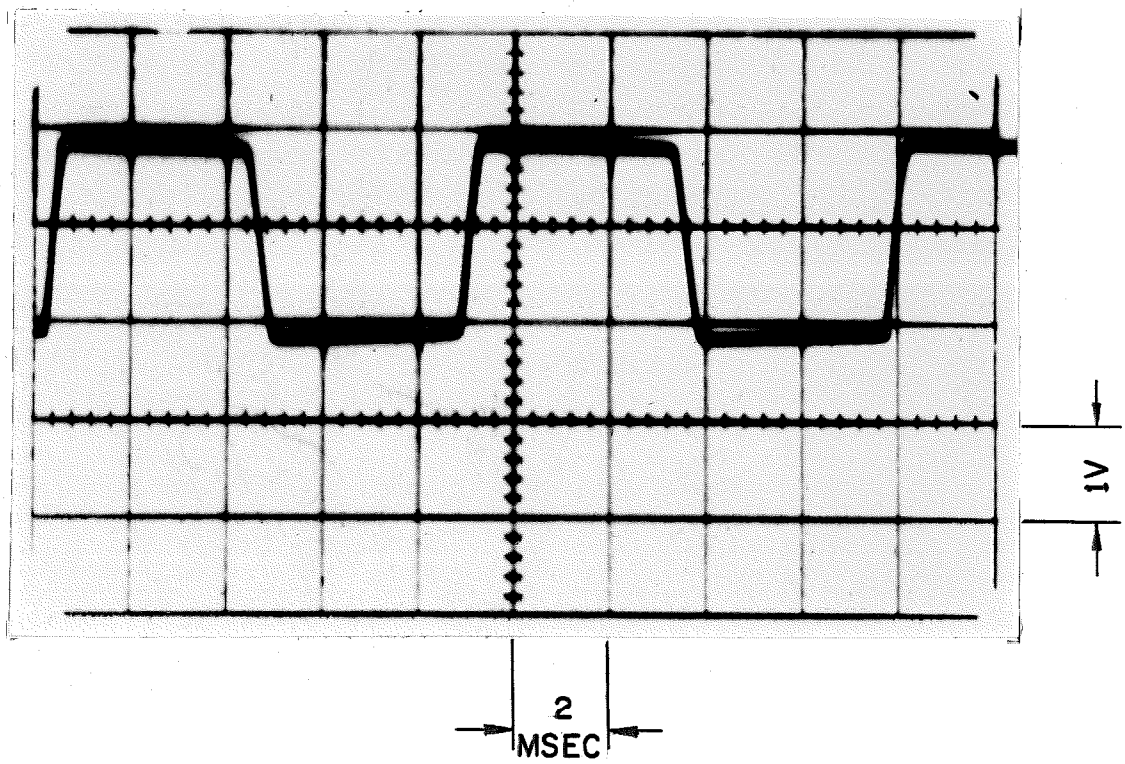

Fig. 18. Oscillogram of signal from chopped infrared radiation during absolute intensity calibration. Only the unfiltered beam was used.

nonlinearity in the vertical direction[24]. All absorption measurements were made at 60 kc, but the emission of hot H_2O caused a step function to be superimposed on the 60 kc wave form. If this step function could be filtered out, then all of the 60 kc wave form would have the same centerline on the face of the oscilloscope, and the remaining nonlinearity, if any, would depend only on the 60 kc amplitude and could be calibrated.

The desired filtering was accomplished with the band-pass filter circuit shown in Fig. 19A with inductances hand wound on hollow plastic forms. Originally the filter was designed to pass 40 kc to 60 kc, but it had such a high Q that it "rang" when subjected to a step function. Consequently, 100 ohm resistors were inserted in series with the two inductances. This changed the pass band to 50 kc-70 kc. The rheostat was included to obtain an impedance match between the lower cathode follower in Fig. 16 and the filter; without a match the filter also "rang." An additional advantage of the band-pass filter was that it filtered out considerable detector noise.

During certain absolute intensity calibrations there was excessive noise from the detector in the unfiltered channel. In order to eliminate this difficulty, a low-pass filter was inserted between points A and B in Fig. 15. The circuit of this filter, shown in Fig. 19B, was designed so that it caused negligible attenuation at 115 cps.

The Tektronix Type 551 dual-beam oscilloscope (Fig. 15) had Type D and B plug-in amplifiers for the lower and upper beams, respectively. The vertical sensitivity varied with line voltage, which was

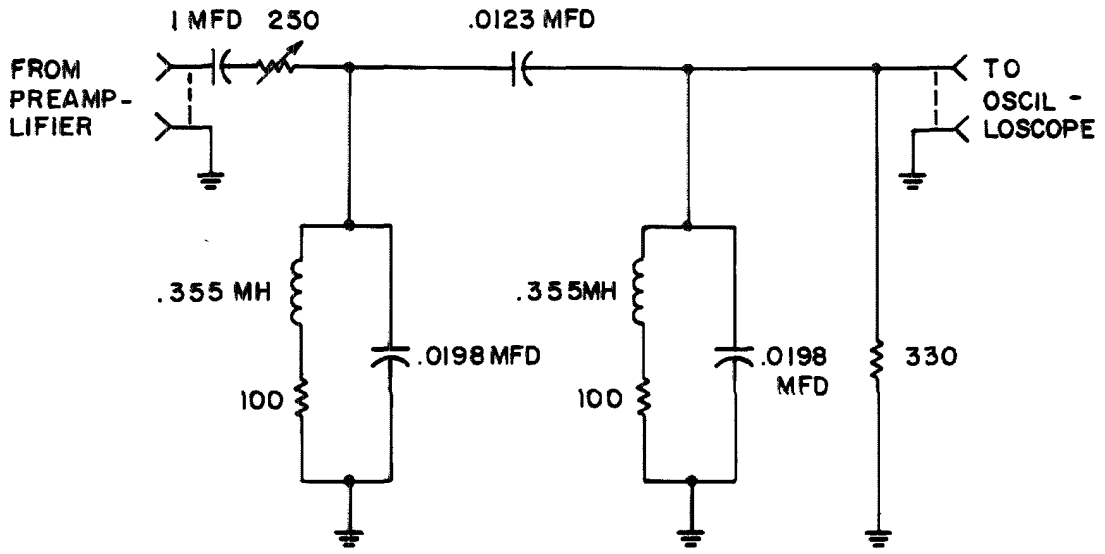

Fig. 19A. Schematic diagram of band-pass filter used to reject all signals except 60 kc.

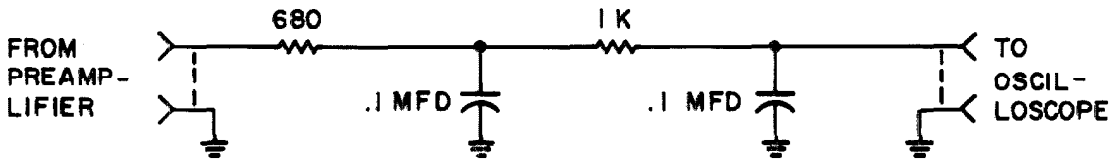

Fig. 19B. Schematic diagram of low-pass filter used to minimize noise in certain absolute intensity calibrations.

stabilized with a Sola constant voltage transformer. The linearity of the filtered preamplifier channel and the vertical linearity of the lower beam of the oscilloscope were collectively checked by attaching an oscillator and precision voltage divider to the preamplifier input and photographing the wave form on the oscilloscope for different settings of the voltage divider. The peak-to-peak amplitude measured to the outside edges of the traces was then determined on an optical comparitor. When an allowance was made for the width of the trace, the system response was found to be linear within the accuracy of the measurements.

The oscilloscope was triggered by an amplified signal from a thin-film gage. As shown in Figs. 6 and 15, the input of the transistorized trigger amplifier[36] was connected at either point A or B, and the output was connected to the oscilloscope. A Quan-Tech Laboratories Model 170-B dc power supply was used for the trigger amplifier.

To measure the chopping frequency of the turbine-driven chopper, the unfiltered preamplifier output was connected to the selector switch in Fig. 6. When the selector switch was set on "turbine," the preamplifier output was applied to the "start" amplifier, and the "stop" amplifier input was terminated in a resistor. The digital counter was then set to measure the frequency on the "start" channel.

D. Gas Handling System

Watson[40] and others found that the usual methods of preparing gas mixtures and filling shock tubes were not applicable to H_2O-Ar gas mixtures due to strong adsorption of the H_2O molecules on the

metal or glass walls of shock tubes; if an H_2O-Ar mixture is simply bled into the driven end of a shock tube, the H_2O will be preferentially adsorbed on the walls. Timnat[24] found indications that this effect was aggravated if the H_2O-Ar mixture was near saturation. Watson solved the problem by continuously bubbling cold Ar through cold H_2O, allowing the flowing mixture to come to room temperature, and then continuously flushing the driven end of the shock tube with it. Timnat continuously bubbled room temperature Ar through room temperature H_2O, throttled the mixture, and continuously flushed the driven end with it. Thus, in both cases an unsaturated mixture was flushed through the shock tube for a period of time sufficient to attain an equilibrium amount of H_2O adsorption on the walls. A modification of Timnat's procedure was developed for the present experiments.

The gas-handling system used in the present work is shown in the simplified schematic diagram of Fig. 4. Basically the Ar was saturated with water in a bubbler, stored, mixed, and allowed to come to room temperature in a reservoir, throttled to a lower pressure, and flushed through the driven end of the shock tube. For shock tube runs Linde 0.99995 pure Ar from four 135 atm commercial bottles (of which several are shown in Fig. 20) flowed into a galvanized manifold and then to a two-stage pressure regulating valve with stainless steel diaphragm, which reduced the pressure to 3.2 atm absolute - 5.4 atm absolute. The Ar then went through shutoff valve V1 and throttling valve V2 to the glass bubbler.

The glass bubbler was suspended in a stirred water bath in a

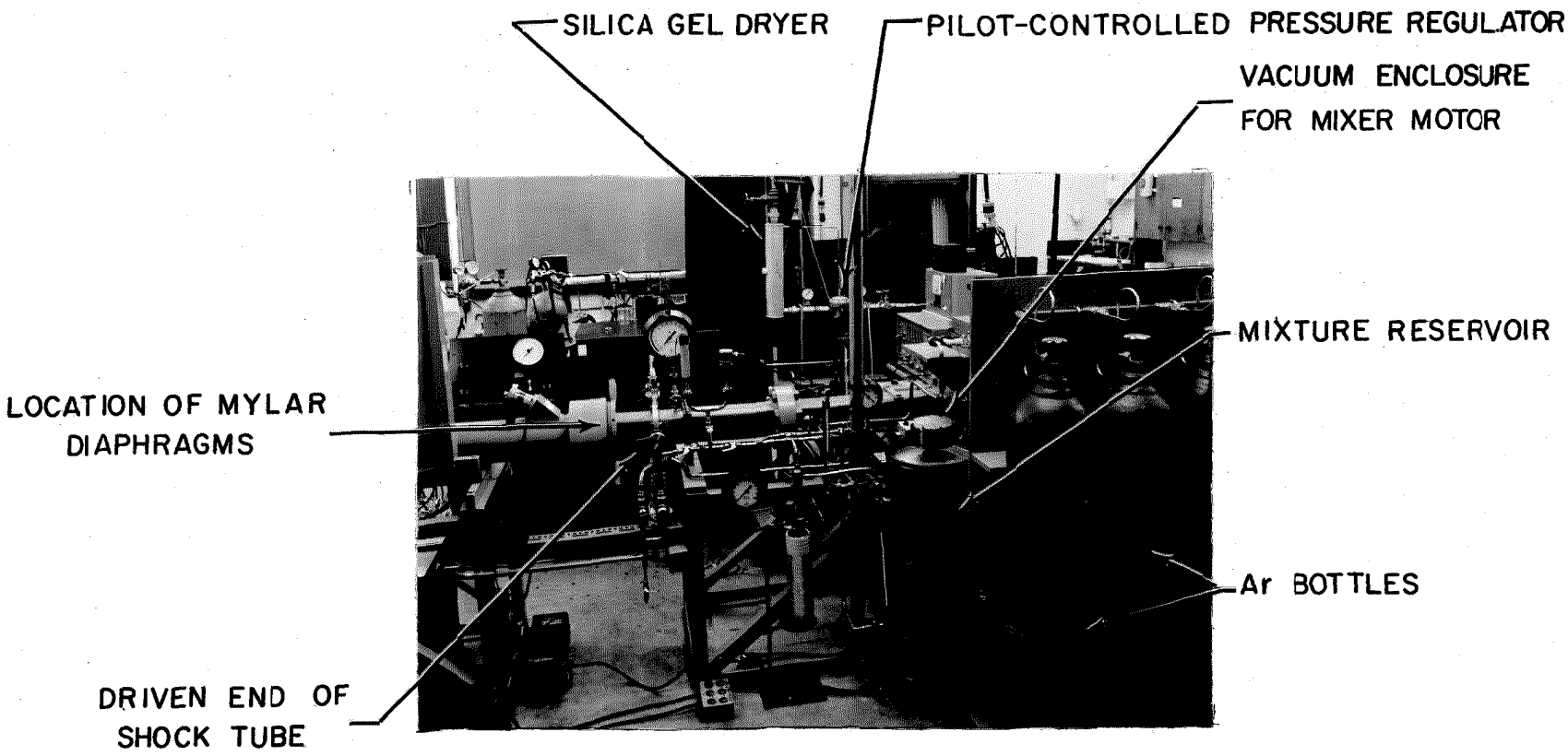

Fig. 20. Photo of shock tube, mixture reservoir, and turbine air supply system. The insulated enclosure containing the water bath and the bubbler is hidden behind the Ar tanks.

Pyrex jar which rested on a plywood box lined with fiber insulation board. The bubbler itself utilized a fine fritted glass plate to disperse the Ar in the distilled water. Due to evaporation, the entire bath was always slightly below room temperature, both temperatures being measured with mercury-in-glass thermometers. The bubbler was connected to the copper tubing used in most of the rest of the system by glass O-ring joints with Viton A O-rings in series with Kovar seals.

The saturated Ar next flowed past a Bourdon-tube pressure gage to the mixture reservoir, which consisted of a 57 lt galvanized iron tank at ambient temperature. The tank had an auxiliary vacuum-tight housing shown in Fig. 20 screwed into the top to accommodate a 3450 rpm shaded-pole motor which drove a folding Nylon propeller through a long shaft. The rotating propeller eliminated inhomogeneities, if any, in the gas mixture.

The gas mixture then flowed through throttle valve V7 and shutoff valve V8 into the driven end of the shock tube, where its pressure was indicated by a second Bourdon-tube gage. Both Bourdon-tube gages read pressure relative to ambient pressure and were calibrated on a dead-weight tester. The pressure of the ambient atmosphere was read on a mercury-in-glass barometer, and the reading corrected for the temperature of the barometer. The gas mixture flowed the entire length of the driven end and out the poppet valve V10.

The gas mixture next entered the sampling device, which was connected at either end to the rest of the system by means of Veeco Vacuum flanges sealed with O-rings and which could be readily dis-

connected. The sampling device consisted essentially of two Circle Seal 9300 series 3-way plug valves bored out to receive two lengths of stainless steel tubing soldered in between them. Extra holes were drilled in the two 3-way valve centers to prevent gas being trapped in the existing holes and seeping slowly out. One length of tubing had one coat of Teflon primer and two coats of Teflon black enamel baked on the inside, and the other was bare. The tube coated with Teflon, which minimized adsorption of water vapor, was used to collect the gas sample, whereas the other was used as a bypass.

From the sampling device the flow went through shutoff valve V13, a flowmeter, and throttle valve V14. Since all shock tube runs were made with the driven pressure more than 1 atm absolute, the expended mixture was throttled through V14 into the atmosphere.

E. Gas Chromatograph

Gas chromatography is a method of analysis in which a flow of carrier gas promotes the separation of gases or vapors by differential migration from a narrow initial zone in a porous sorptive medium. The subdivision of chromatography used in this study was gas-liquid partition chromatography, wherein the porous sorptive medium consists of a loosely packed inert solid coated with a low vapor pressure material such as a high boiling point wax, grease, or liquid. The gases or vapors being analyzed will each have a specific distribution between the two phases according to their respective solubilities in the wax, grease, or liquid, and, consequently, the times for each to pass through the column of porous sorptive medium will, in general, be

different.

Timnat[24] separated Ar and H_2O using a column of 10% Carbowax 1540 on T-6 Teflon (supplied by Beckman Instruments) packed in a 120 cm length of 0.63 cm od stainless steel tubing. He used a commercial chromatograph and He carrier gas. Unfortunately, the commercial chromatograph was neither available nor reliable enough for the present experiments, so a special chromatograph was built just to separate H_2O-Ar mixtures, using Timnat's column and He carrier gas.

The general arrangement is shown in Figs. 21 and 22. A commercial 135 atm He tank supplied He carrier gas through a pressure regulator that reduced the pressure to 3.8 atm absolute. It then flowed through a glass trap to remove solid contaminants and a Brooks Sho-Rate flowmeter with an R-2-15-AA-CO tube and a glass ball. From there a 0.32 cm od copper tube took the He to two reference filaments in a massive brass block. The flow then went to the sampling device, through the column, and to two sensing filaments. Both reference and sensing filaments were Loenco 70 ohm heated-tungsten thermal-conductivity detectors which could sense when Ar or H_2O from the sampling device passed through the sensing side of the brass block because of the change of thermal conductivity of the gas mixture causing changes in temperature and resistance of the filaments. From the sensing elements the gas mixture flowed through a Nupro B-2S needle valve to the atmosphere.

In operation the 3-way valves were set so the He flow was

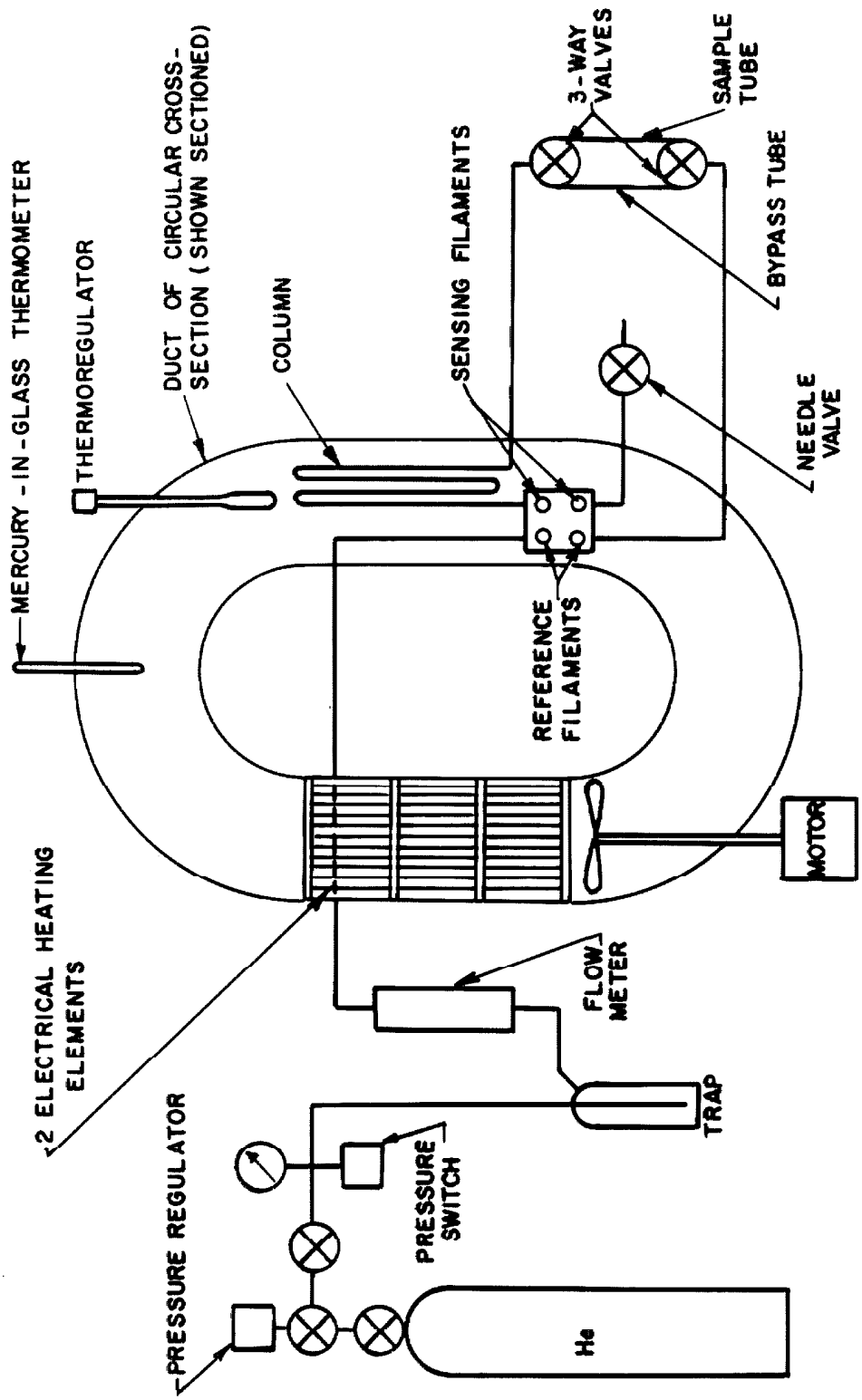

Fig. 21. Schematic diagram of gas chromatograph oven and piping. The insulated oven enclosure was omitted from the diagram in the interest of simplicity.

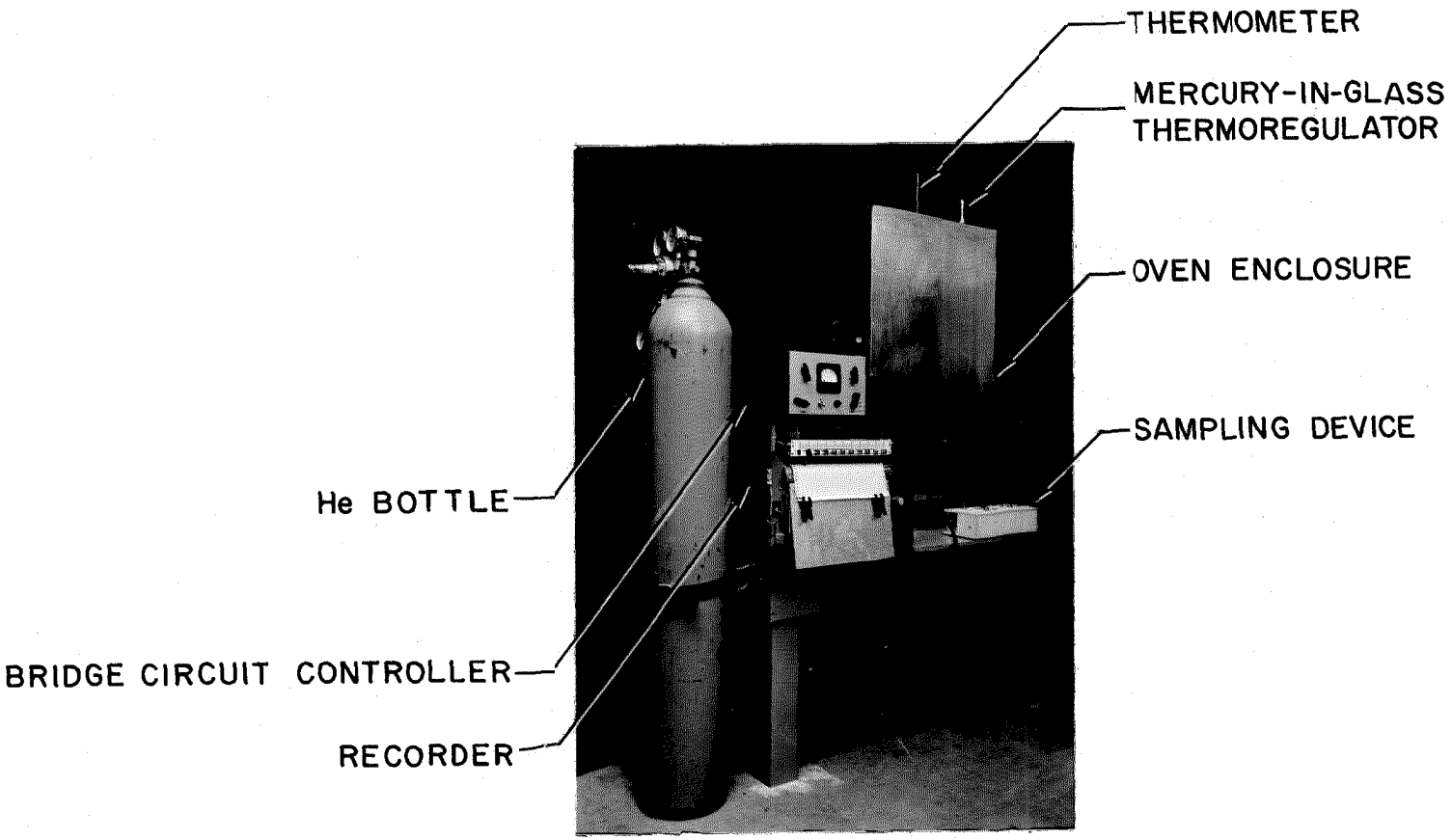

Fig. 22. Photo of gas chromatograph used to measure concentration of water vapor in the argon/water vapor mixture in the driven end of the shock tube.

through the bypass tube. After all foreign gases had been flushed from the system, the lower 3-way valve was turned, followed 5 sec later by the upper 3-way valve, thus diverting the He carrier flow through the sample tube and carrying the H_2O-Ar sample into the column. Since the times for the H_2O and Ar to pass through the column were different, the amount of H_2O could be determined from the change of resistance of the sensing filaments, as delineated in Section IVC below.

The column and the filament block were kept at a constant temperature of 373 ^{o}K by an oven based on the principle of forced recirculation of hot air in a loop of duct. The duct, shown in Fig. 21, consisted of 12.7 cm diameter stove pipe. The air was blown by a motor-driven fan through an assembly of parallel nichrome-wire electrical heating elements, past a mercury-in-glass thermometer, past a Precision Scientific Cat. No. 2537 mercury-in-glass thermoregulator, the column, and the filament block, back to the fan. The duct was contained in an aluminum case shown in Fig. 22 and insulated with fiberglass.

The heating element assembly (Fig. 21) actually contained two heating elements, one of which was on all the time. A schematic diagram of the power circuit is given in Fig. 23 with the continuous heater on the left. The other heater was controlled by the previously-mentioned mercury-in-glass thermoregulator.

The four heated tungsten filaments were each in a different arm of a Wheatstone bridge, as shown in Fig. 24. The purpose of the

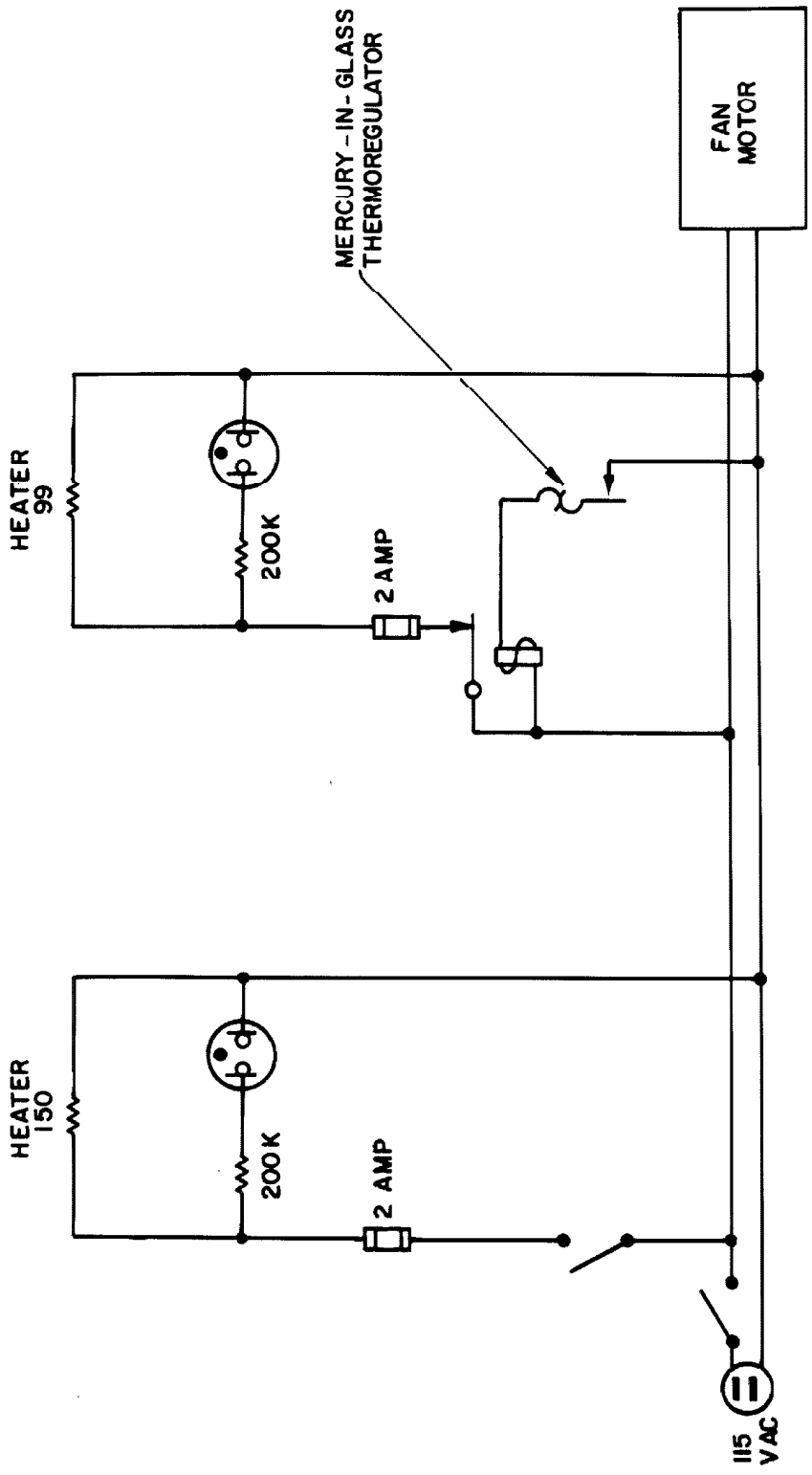

Fig. 23. Schematic diagram of gas chromatograph power circuit used to heat the air in the duct in the oven. The 150Ω heater was on continuously, but the 99Ω heater was turned on intermittently by the mercury-in-glass thermoregulator.

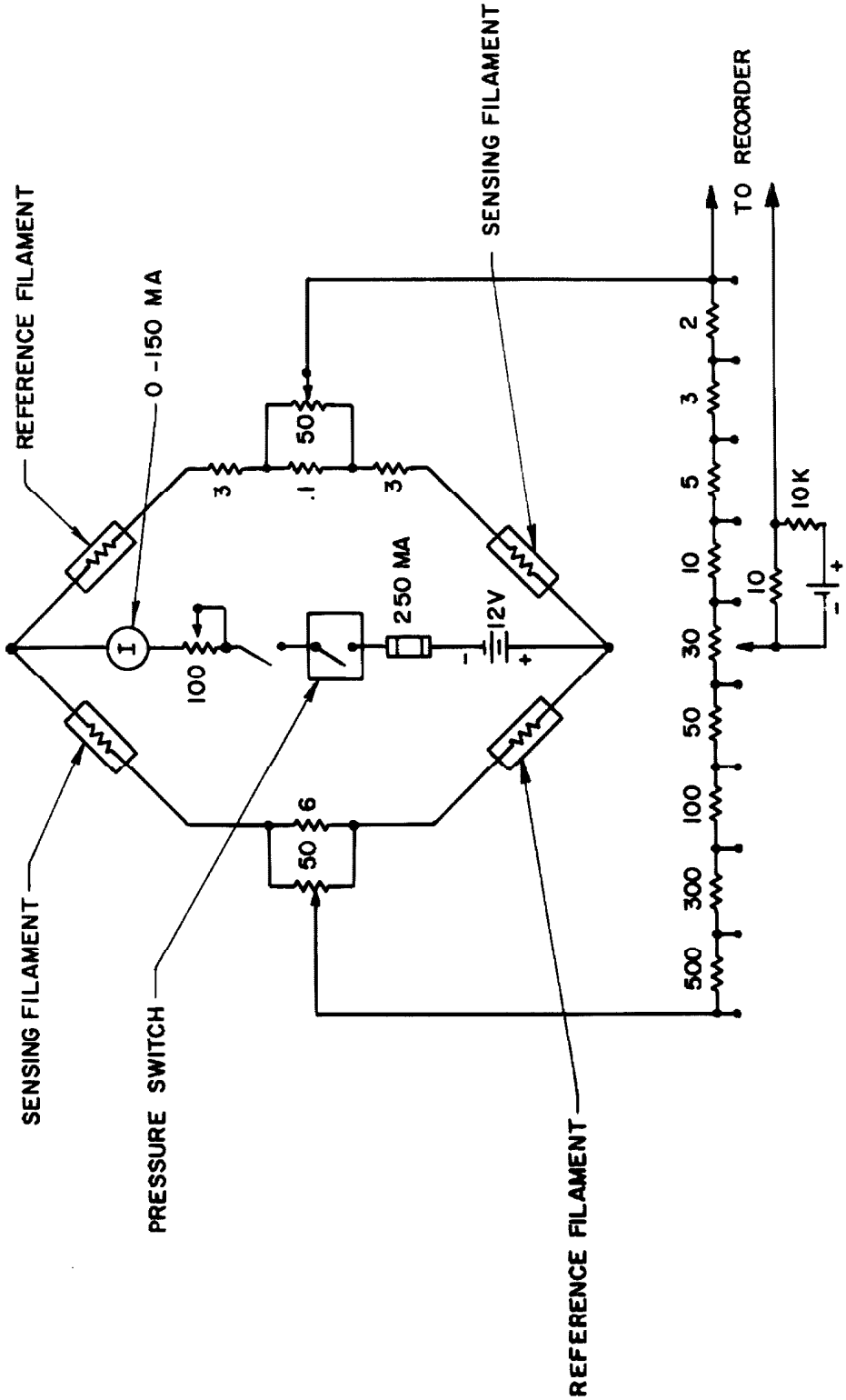

Fig. 24. Schematic diagram of gas chromatograph Wheatstone bridge circuit used to detect changes in thermal conductivity of the gas mixture passing the sensing filaments. All filaments were heated, and the reference filaments were in a flow of pure He.

reference filaments was to keep the output of the bridge essentially zero despite small changes in the carrier gas flow rate or the filament block temperature. Power was supplied by a 12 v storage battery, which was disconnected by a pressure switch (Figs. 21 and 24) in case of an inadvertent decrease of He pressure. The current to the bridge was controlled by a potentiometer and measured by a Simpson Model 27 meter.

Balance of the bridge was obtained initially by coarse and fine zero adjustments by means of potentiometers on either side of the bridge. The subsequent unbalance was applied to an attenuator consisting of nine precision resistors. The output of the attenuator was applied to a Brown 153X 12V-X-30 0-15 mv recorder after being biased 1.35 mv by a mercury cell. Consequently, any change in output of the recorder was proportional to the change in thermal conductivity of the gas mixture passing the sensing filaments.

IV. EXPERIMENTAL PROCEDURE

The various shock tube runs were divided into two groups: simultaneous emission and absorption measurements at an average temperature of 1000 ^{o}K, and emission measurements at an average temperature of 1933 ^{o}K. However, the preliminary procedures for the two groups were essentially the same and are discussed first.

A. Optical Preliminaries

The points used to obtain the wave number calibration of the monochromator are listed in Table I.

TABLE I. WAVE NUMBER CALIBRATION POINTS USED TO CALIBRATE THE MONOCHROMATOR

Substance	Wave number, cm^{-1}	Entrance and exit slit widths, mm	Reference
He	4859	0.35	41
1, 2, 4 trichlorobenzene	4645	1.0	42
1, 2, 4 trichlorobenzene	4103	1.0	42
quartz	3656	1.0	42
1, 2, 4 trichlorobenzene	3083	1.0	42
polystyrene	3028	1.0	42
polystyrene	2922	1.0	42
1, 2, 4 trichlorobenzene	2812	1.0	42
1, 2, 4 trichlorobenzene	2698	1.0	42
CO_2	2353	1.0	43

All wave number settings were approached from higher wave numbers, but otherwise the procedures varied as outlined below.

The He singlet was observed in emission with the arrangement used for slit function measurements.

The quartz and polystyrene calibrations were made in absorption with 2.5 cm of quartz or 0.05 mm of polystyrene in the optical path, respectively. Otherwise the arrangement was the same as for shock tube runs. The absorption in quartz was due to occluded H_2O [42].

The 1, 2, 4 trichlorobenzene calibration was performed by injecting 1, 2, 4 trichlorobenzene into a cell between two sapphire windows 0.4 mm apart. The cell was placed against the window adjacent

to the turbine-driven chopper slit and was observed in absorption with the arrangement used for shock tube runs, but with the vacuum enclosure containing M1, M2, M3, M5, and M6 open to the atmosphere.

Atmospheric CO_2 was observed in absorption with the same arrangement used for shock tube runs but with both vacuum enclosures open to the atmosphere.

The dial of the monochromator had once been properly calibrated in microns for an NaCl prism. A plot of calibration point wavelengths versus dial readings yielded a straight line within the limits of experimental error.

The transmitted infrared intensity vanished at the 2353 cm^{-1}, 2922 cm^{-1}, and 3083 cm^{-1} wave number calibration points, indicating that stray infrared was not being received by the detector.

The apparatus for slit function measurement has been described. The 120 cps output of the Geissler tube was found to be quite stable, and the 120 cps superimposed on the 10 cps chopper frequency caused no difficulty. However, noise from the PbS detector, which appeared to be typical, made it necessary to average the reading of the amplifier output meter by eye for a period of several minutes. In the slit function measurement with 0.35 mm slits, the extreme-to-extreme value of the noise was 0.4 times the magnitude of the maximum signal. The results of the slit function measurements are shown in Fig. 25 for the He 4859 cm^{-1} singlet. The slit function for 0.35 mm slits agreed quite well with the ideal slit function in Fig. 1A, but the slit function for 1.0 and 2.8 mm slits deviated somewhat from the ideal slit function in Fig. 1B.

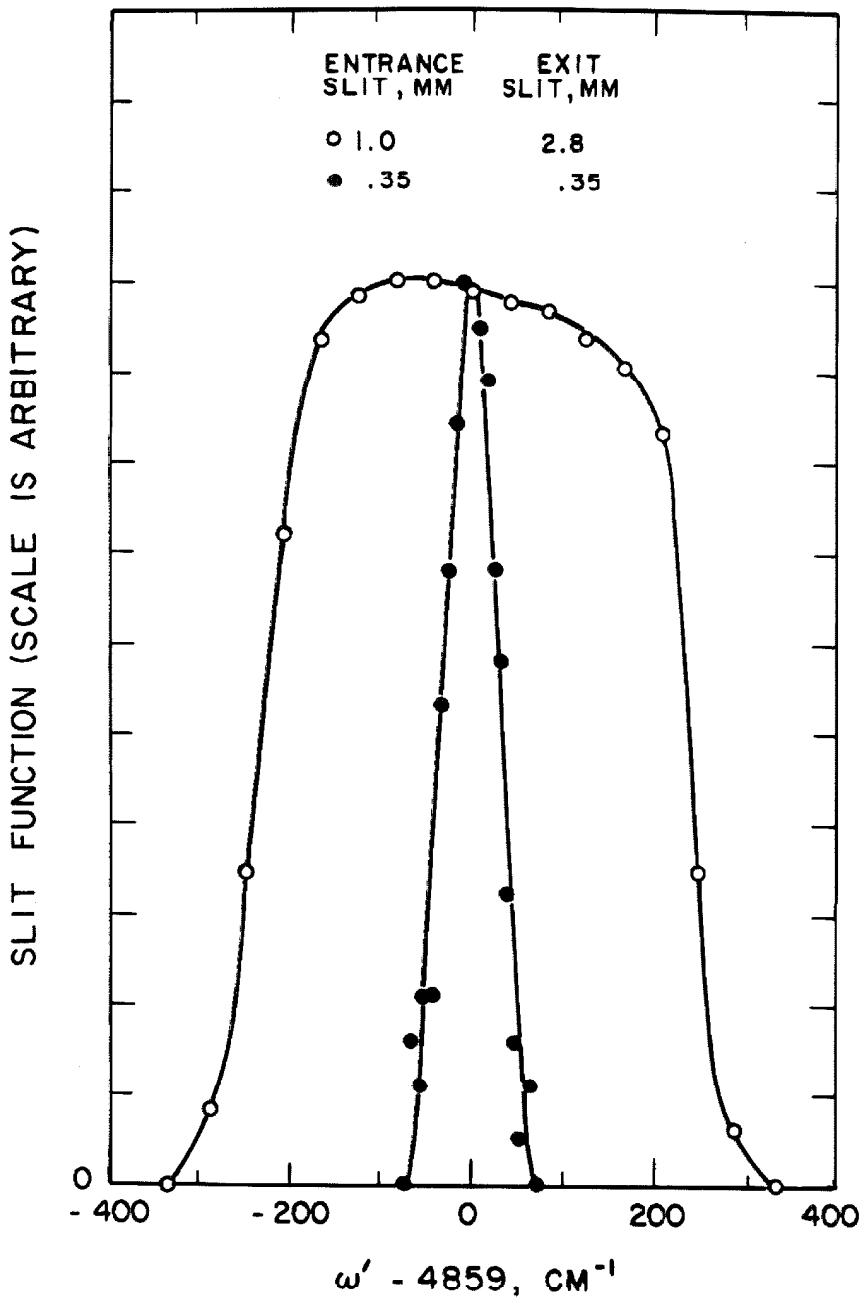

Fig. 25. Graph of slit functions of IR2 monochromator modified so that the maximum entrance slit opening was 1 mm. For convenience in plotting, the slit functions were normalized to have the same maximum value. Both were measured with the He line at 2859 cm^{-1}.

Absolute intensity calibration was carried out for every combination of ω and slit setting used for shock tube runs. First the linearity of the gold-doped germanium detector was investigated at 3704 cm^{-1} by varying the blackbody temperature from 806 ^{o}K to 1273 ^{o}K (its maximum). The temperature-E. M. F. function of the thermocouple was obtained from Ref. (41), and the blackbody steradiancy was then obtained from Ref. (44). The response of the detector was found to be linear over the range investigated to within the experimental error.

In contrast, all intensity calibrations for shock tube runs were performed with the blackbody at constant temperatures near 1260 ^{o}K. After the blackbody had reached an equilibrium temperature, the amplitude of the signal (Fig. 18) was read by eye by first centering the wave form horizontally on the graticule and then lining up the bottom of the wave form with a graticule line. The thermocouple potentiometer was then read to an accuracy corresponding to better than ± 1 ^{o}K, and the wave number setting ω of the monochromator was readjusted for the next calibration point. Before every second calibration point, the thermocouple potentiometer was restandardized.

After all points had been recorded, a value of the product $W_{\omega}F_{\omega}$ was calculated by Eqs. (26) and (28) for each calibration point. These absolute intensity calibrations were carried out before and after each of the two groups of shock tube runs, and the results compared. A typical difference of 2% was found but was not considered important because no attempt was made in emission measurements to correct

for the nonlinear response of the oscilloscope in the vertical direction, which may have amounted to 6%[24].

One absolute intensity calibration was performed at 3571 cm^{-1} with a Corning No. 2600 filter mounted in the light path adjacent to the LiF lens in Fig. 2. This filter had a relatively constant attenuation of about 0.039 near 3571 cm^{-1}, and its use is described further in Section IVE.

B. Preparation of the Gas Mixture

Care was exercised in the preparation of the gas mixture to eliminate as much air and CO_2 from the mixture as possible. First the bubbler in Fig. 4 was replaced by a length of glass tubing and the system pumped down to 50 μHg up to the Ar bottle valves. Valve V1 was then closed, and the Ar bottle valves opened, filling all piping up to V1 with Ar. The bubbler was then partially filled with distilled H_2O and reinstalled. It was next pumped down for 10 min via V4, the liquid nitrogen trap, and V5, causing air between V1 and the fritted glass of the bubbler to bubble up through the water and also causing the water in the bubbler to boil.

After removing the H_2O from the bath, a small Ar flow through V1 and V2 was established, and the side of the bubbler was heated with a Tirrill burner while V4 was throttled to maintain 0.33-0.50 atm absolute pressure in the bubbler. Consequently, boiling took place at 345 ^{o}K - 355 ^{o}K, expelling dissolved CO_2 from the H_2O. After 15 min the boiling was stopped, and the H_2O bath refilled. Some additional Ar was flushed through the bubbler to get rid of any remaining traces

of air, and the mixture reservoir was pumped to 20 μ Hg and filled with Ar-H_2O mixture to 1.25 times the desired shock-tube driven-end pressure.

C. Concentration Analysis

Mixtures of from 1.2% to about 90% H_2O in Ar were analyzed with the gas chromatograph. In all cases a sample was collected in the sampling device (Fig. 21) by connecting it to a gas system, allowing a sample to diffuse into or flow through the sample tube, and then trapping the sample by turning one or both of the 3-way valves. The sampling device was then disconnected from the gas system and reconnected as shown in Fig. 21. A flow of 100 cm^3 (STP)/min of He was then maintained through the bypass tube and the chromatograph for two hours to flush out all air. The chromatograph bridge zero was next recorded, and the lower 3-way valve turned. About 5 sec later the upper 3-way valve was turned, so that the sample was flushed into the column. The Ar peak (Fig. 26) was recorded, followed by the H_2O peak. In some cases it was necessary to change the attenuator setting between the two peaks. The total area of the H_2O peak was measured with a Crosby Steam Gage and Valve Co. planimeter.

No attempt was made to measure Ar concentration because in the case of most interest the Ar concentration was so high that it not only changed the bridge current when it passed the sensing filaments but also changed the flow rate of the chromatograph when it passed through the needle valve. Consequently, any results would probably have been nonlinear and dependent on the condition of the storage

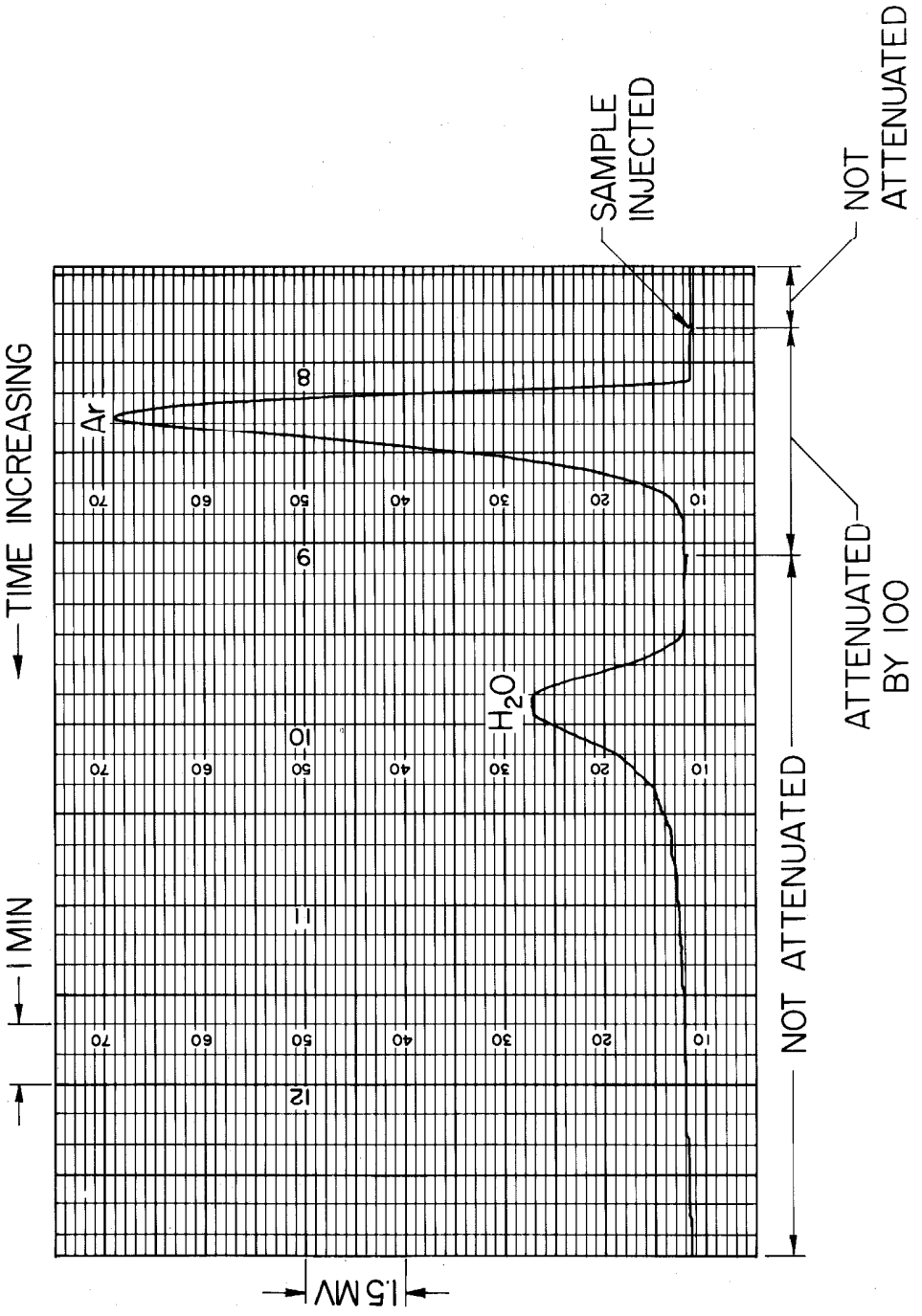

Fig. 26. Typical recorder record from gas chromatograph analysis of H_2O-Ar gas sample taken from shock tube (half size). The two peaks were due to Ar and H_2O respectively. The concentration of H_2O in the sample was proportional to the area under the H_2O peak.

battery. Fortunately, all of the Ar was out of the chromatograph before the H_2O passed the sensing filaments; hence the only effect was to broaden the H_2O peak, leaving the area unchanged.

Calibration samples were obtained by connecting the sampling device between V3 and the tubing junction (Fig. 4) after CO_2 and air had been eliminated from the bubbler and adjacent tubing, and the amount of Ar had been minimized. The sampling device was pumped down and V3 opened to allow H_2O vapor to diffuse into the sample tube. In many cases ice or dry ice was placed in the box containing the water bath and bubbler to reduce the temperature and the H_2O vapor pressure. The amount of H_2O vapor above the H_2O in the bubbler was obtained from the temperature of the water bath and vapor pressure data[41]. After a period of time the sample was isolated in the sampling device by turning a 3-way valve, and the sample was analyzed on the gas chromatograph. From the results of the analysis it was found that roughly 3 hr was necessary to fill the sample tube by diffusion. With little Ar present the area of the H_2O peak was directly proportional to the H_2O concentration to within 2%, but with sizeable amounts of Ar present the accuracy was only about 5%.

After having shown that the bubbler saturated the Ar with H_2O, the adsorption of H_2O on the walls of the shock tube was investigated. The mixture from the mixture reservoir was throttled by V7 to 0.8 of reservoir pressure, thereby making the mixture 0.8 saturated. The pressure in the shock tube was maintained at 2.7 atm absolute, and a continuous steady flow maintained to change the mixture in the shock tube once every 5 min. The sampling device was connected as shown

in Fig. 4, and a sample taken while the mixture was flowing through the system. A flushing time of 3 hr was found necessary for the H_2O thickness on the shock tube walls to closely approach equilibrium.

During shock tube runs the mixture in the shock tube was stagnant for a short period just before firing the shock tube. To see what effect this had, a sample was taken after the shock tube had been flushed 3 hr and then remained stagnant 5 min. It was found that there was 7% less H_2O than obtained without the stagnant period, but this was based on a single measurement so is not considered very reliable. In shock tube runs the stagnant time never exceeded 1 min 54 sec.

Unfortunately, the chromatograph recorder developed a defect at the beginning of the shock tube runs, so the chromatograph was not used. Instead, the H_2O partial pressure in the shock tube after flushing it 3 hr was assumed to be

$$p_{H_2O} = p_{H_2O,\,sat} \frac{p_{st}}{p_r} \tag{34}$$

where $p_{H_2O,\,sat}$ was the vapor pressure of water at the temperature of the H_2O bath (Fig. 4), p_{st} was the initial absolute pressure in the driven end of the shock tube, and p_r was the absolute pressure in the mixture reservoir. From data obtained while the gas chromatograph was operating, Eq. (34) appeared to fit the measured data very accurately.

D. Preparation and Filling of the Shock Tube

The inside of the driven end was sand blasted after fabrication,

and it was also cleaned with steel wool and acetone before assembly for the present experiments. Before each shock tube run it was blown out with dry N_2 and pumped to 50 μHg. Further pumping was deemed undesirable because it would only remove more H_2O adsorbed on the walls. A continuous flow of H_2O-Ar mixture was established through the driven end and controlled by the pressure regulating valve (Fig. 4) and throttle valves V7 and V14. The driven end absolute pressure was maintained at 0.8 of the reservoir pressure, and the flow was sufficient to change the mixture in the shock tube every 5 min. After flushing for 3 hr a sample was taken, and V8 and V10 were closed. The pressure was read, V9 closed, and the shock tube fired.

E. Precautionary Runs

If infrared emitted by the hot H_2O in the shock tube was reflected by M6 and M5 (Fig. 3), passed through the window (Fig. 3 and 10), reflected from the aluminum between the 90 slots of the chopper wheel (Fig. 10), returned via M5 and M6 to the shock tube, and continued to the monochromator entrance slit, serious errors in absorption measurements would result because the spurious infrared would have the same modulation frequency as the beam from the blackbody. Several shock tube runs were made to investigate this with the blackbody at room temperature but the turbine-driven chopper running, and the effect was finally made negligible by caustic etching and black anodizing the chopper wheel (Fig. 10).

If the Ar contained impurities, these could contribute to the infrared emission and absorption of the H_2O-Ar mixture. To investi-

gate this, sixteen shock tube runs were made on Ar with no H_2O added. No emission or absorption in the entire wave number range used for the later H_2O shock tube runs was noted.

Unfortunately, the maximum steradiancy of the blackbody was much less than the H_2O steradiancy in the group of shock tube runs with temperatures averaging 1933 ^{o}K. Consequently, there was no direct method for checking the linearity of the gold-doped germanium detector at the steradiancies obtained from the 1933 ^{o}K group of runs. However, an indirect method was devised and carried out at 3571 cm^{-1}. First, absolute intensity calibrations were performed with and without a Corning No. 2600 filter mounted in the light path adjacent to the LiF lens in Fig. 2. Second, shock tube runs on H_2O-Ar mixtures were performed with and without the filter. If any simple sort of nonlinearity in the detector existed, the absorption coefficients calculated from the two shock tube runs and their respective intensity calibrations should have disagreed, but in fact they agreed within 15%, which was about the magnitude of experimental scatter of absorption coefficients obtained from shock tube runs.

F. Simultaneous Determination of Absorption and Emission from H_2O

Simultaneous H_2O absorption and emission measurements were performed in the shock tube at an average temperature of 1000 ^{o}K. All measurements were made with a 1 mm entrance slit and a 2.8 mm exit slit, but the wave number setting was changed for each shock tube run in order to cover the group of overlapping H_2O bands of interest. Due

to the manner of variation of $\delta_1\omega$ with wave number and other factors, it was found appropriate to make the wave number settings at equally spaced wavelengths instead of equally spaced wave numbers and with such an increment between settings that slit functions for the different settings substantially overlapped.

Three oscillograms were recorded for each shock tube run, as exhibited in Fig. 27. The first (upper) oscillogram was taken after the shock tube had been flushed for 3 hr and the chopping frequency adjusted to 60 kc but before the bursting of the diaphragm. Consequently, the chopped infrared beam was attenuated by the room-temperature H_2O in the shock tube. Just before firing the shock tube, the chopping frequency was readjusted to 60 kc. The sweeps shown in the second oscillogram were triggered by the incident shock wave and show conditions before arrival of the incident shock wave, after arrival of the incident shock wave, and after arrival of the reflected shock wave, in that order. The incident shock wave did not produce much emission, but the reflected shock wave did, as indicated by the change in level of the lowest points of the unfiltered beam. Since the amplitudes in the first oscillogram and before the incident shock wave in the second oscillogram were the same, it is clear that firing the shock tube did not misalign the optics.

After firing the shock tube the diaphragm was replaced, and the driven end evacuated to 50 μ Hg. The chopping frequency was readjusted to 60 kc, and the third (bottom) oscillogram was taken. By comparing the amplitudes of the lower traces in the second and third

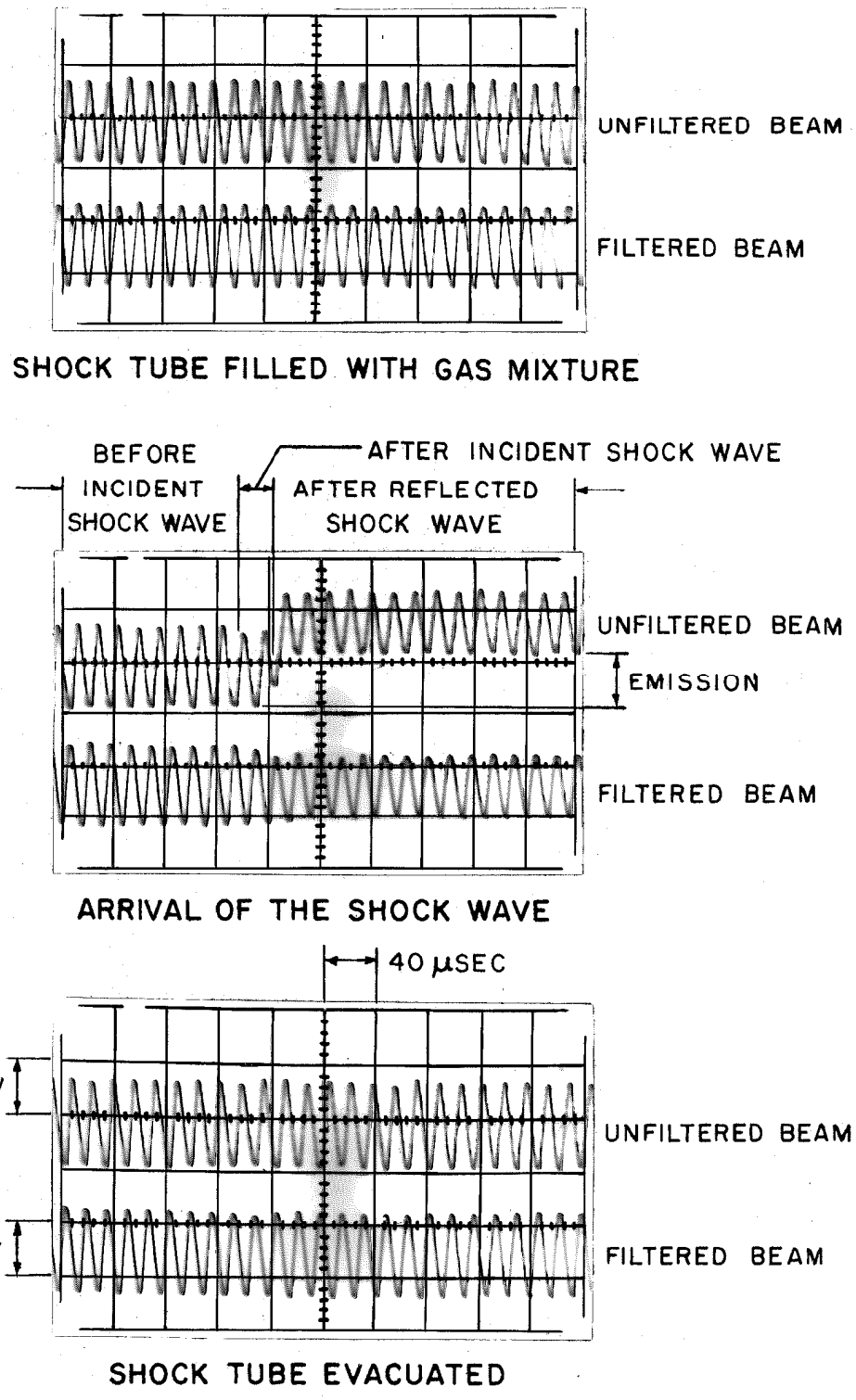

Fig. 27. Sequence of three oscillograms for a typical run where both H_2O emission and H_2O absorption were recorded. The 60 kc wave was produced by chopped infrared radiation transmitted through the shock tube. The graticule was enhanced with a pen.

oscillograms, the attenuation of the chopped infrared beam was ascertained.

G. Determination of H_2O Emission Only

Two attempts to measure absorption of H_2O at temperatures of the order of 2000 ^{o}K were unsuccessful due to excessive noise in the filtered trace. This noise was the fraction of the noise associated with the large emission that was not removed by the band-pass filter and was probably due either to slight inhomogeneities in the H_2O-Ar mixture or to the random distribution in time of detected infrared quanta. Consequently, only emission measurements were subsequently made near 2000 ^{o}K. The blackbody and the turbine-driven chopper were shut off, and only the upper beam of the oscilloscope was used. A typical oscillogram is given in Fig. 28. Most of the runs were made with 1.0 mm entrance slit and 2.8 mm exit slit, and the slit functions for this series of runs overlapped substantially.

V. EXPERIMENTAL RESULTS

In this section the experimental spectral absorption coefficients are calculated and presented. The integrated absorption coefficients are determined, and the accuracy is discussed.

A. Conditions behind the Reflected Shock

Data from each shock tube run included initial temperature, initial pressure, fraction of H_2O in the H_2O-Ar mixture, and incident shock velocity. One-dimensional flow of an ideal gas with variable

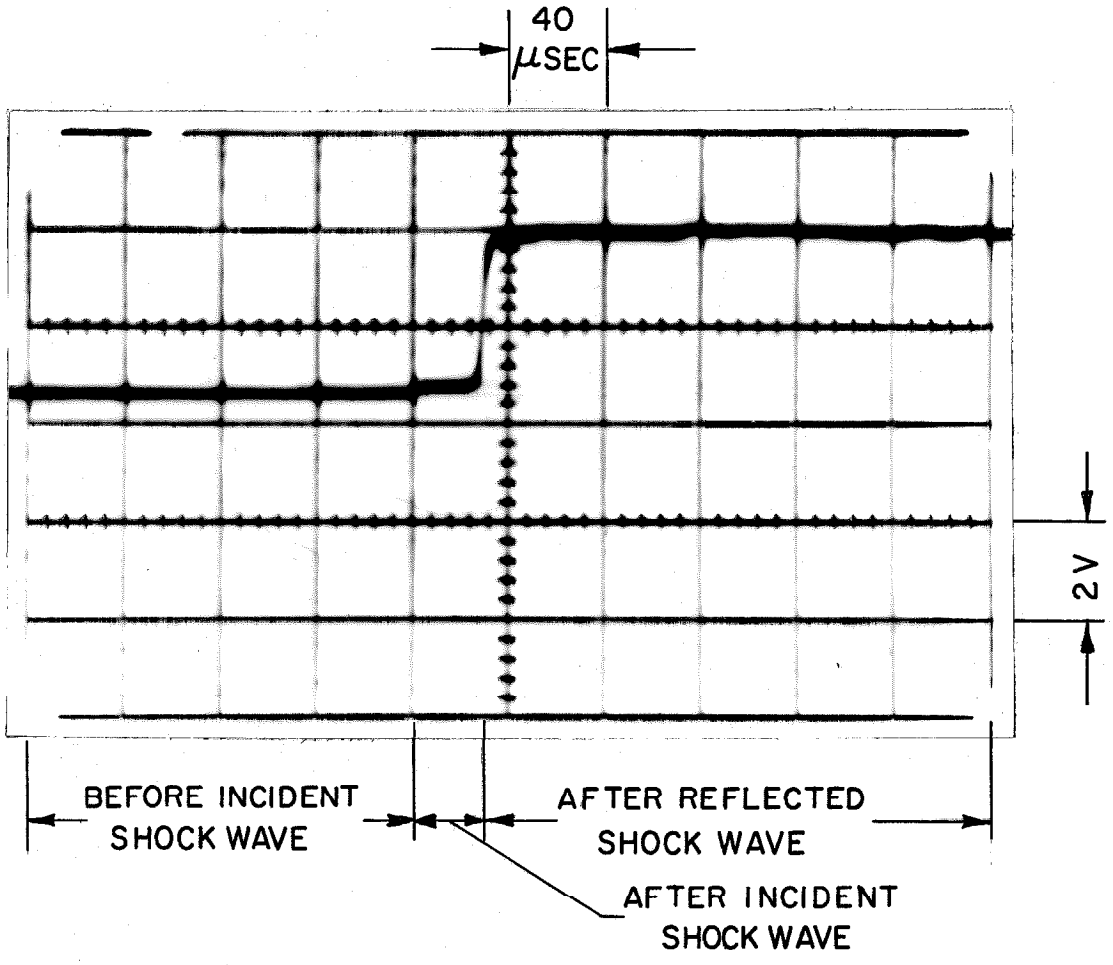

Fig. 28. Typical oscillogram (run 71) where only H_2O emission was recorded. Only the unfiltered beam was used.

specific heat was assumed, and the momentum, energy, and continuity equations were solved for the incident shock wave. This procedure gave a finite gas mixture velocity with respect to the shock tube. Assuming the reflected shock wave brought the mixture to rest, the momentum, energy, and continuity equations were solved for the reflected shock wave. These calculations were performed at the Aerospace Corporation on an IBM 7090 digital computer assuming no chemical reactions.

The method of calculating the H_2O enthalpies used is given in Ref. (45). To check it, the H_2O enthalpy differences

$$\Delta H \equiv H_T - H_{298.16} \tag{35}$$

where H_T is the enthalpy at temperature T and $H_{298.16}$ is the enthalpy at $298.16\ ^{o}K$, were calculated from enthalpies given in Refs. (45) - (50) and compared. The values of ΔH from Refs. (46) - (50) did not differ from ΔH of Ref. (45) by more than 0.6% for temperatures from $1000\ ^{o}K$ to $2200\ ^{o}K$.

The results of the reflected shock calculations are given in Table II along with the wave number settings of the monochromator and the effective band widths.

TABLE II. REFLECTED SHOCK WAVE CALCULATIONS FOR SHOCK TUBE RUNS, ASSUMING NO CHEMICAL REACTION. THE WAVE NUMBER SETTINGS OF THE MONOCHROMATOR AND THE EFFECTIVE BAND WIDTHS ARE ALSO GIVEN SO THAT RUNS MAY BE IDENTIFIED WITH POINTS IN FIGS. 29 AND 30.

Run no.	Initial pressure, atm	Initial temperature, °K	Incident shock velocity, mm/μsec	Pressure behind reflected shock, atm	Partial pressure of H_2O behind reflected shock, atm	Temperature behind reflected shock, °K	Wave number, cm^{-1}	Effective band width at $3704\ cm^{-1}$, cm^{-1}
43	2.71	304.4	0.632	36.9	0.436	985	3704	206
44	2.71	304.2	0.633	37.2	0.433	988	3846	206
45	2.71	304.2	0.648	40.0	0.468	1029	3571	206
46	2.72	304.5	0.627	36.0	0.432	971	4000	206
47	2.71	304.4	0.651	40.6	0.490	1038	3448	206
48	2.73	303.6	0.646	40.1	0.482	1023	4167	206
49	2.72	303.8	0.641	38.8	0.468	1009	3333	206
50	2.73	303.8	0.649	40.7	0.486	1032	3226	206
51	2.73	304.4	0.623	35.4	0.426	960	3125	206
52	1.25	303.3	0.926	52.1	1.22	1931	3571	206
55	1.24	303.8	0.934	52.9	1.27	1961	3846	206
56	1.24	303.2	0.946	54.9	1.27	2009	4000	206
57	1.24	305.2	0.934	52.5	1.31	1959	3448	206
58	1.24	303.8	0.912	49.6	1.26	1874	4167	206

TABLE II (Continued)

Run no.	Initial pressure, atm	Initial temperature, ^{o}K	Incident shock velocity, mm/μsec	Pressure behind reflected shock, atm	Partial pressure of H_2O behind reflected shock, atm	Temperature behind reflected shock, ^{o}K	Wave number, cm^{-1}	Effective band width at 3704 cm^{-1}, cm^{-1}
59	1.25	304.2	0.912	49.8	1.27	1873	3333	206
60	1.24	304.8	0.949	55.0	1.42	2014	4348	206
61	1.24	304.1	0.926	51.6	1.35	1924	3226	206
62	1.24	302.9	0.920	51.0	1.23	1907	4545	206
63	1.24	302.8	0.912	49.9	1.23	1875	3125	206
65	1.24	302.3	0.917	50.7	1.24	1894	3030	206
66	1.24	301.2	0.928	52.7	1.10	1945	2941	206
67	1.24	301.8	0.943	54.9	1.19	2001	2857	206
68	1.24	303.0	0.940	54.2	1.23	1987	2778	206
69	1.24	303.2	0.923	51.6	1.20	1920	2703	206
71	1.24	304.2	0.946	55.5	1.41	2010	3704	206
72	1.24	304.6	0.914	49.7	1.24	1883	3922	69
74	1.25	306.3	0.914	49.7	1.30	1880	3774	69
75	1.25	305.8	0.917	50.1	1.37	1888	3448	69

B. Spectral and Integrated Absorption Coefficients

To determine the apparent spectral absorption coefficients, the oscillogram traces were measured on an optical comparator. Using the data in Table II, $P_{\omega, ap}$ was then calculated from Eq. (33) while $\tilde{P}_{\omega, ap}$ was calculated from Eq. (32).

Unfortunately, the various shock tube runs of each of the two groups produced slightly different temperatures behind the reflected shock wave: for one group the temperature varied from 960 ^{o}K to 1038 ^{o}K, for the other from 1873 ^{o}K to 2014 ^{o}K. In order for the apparent spectral absorption coefficients of each group to be comparable, they had to be adjusted to a standard temperature. This change was accomplished approximately by assuming that the absorption cross section σ_T of the H_2O molecule at temperature T did not change with the temperature, or

$$\sigma_{\overline{T}} = \sigma_T \tag{36}$$

where $\sigma_{\overline{T}}$ is the absorption cross section at the average temperature of the group of runs. The absorption cross section σ_T and spectral absorption coefficient $P_{\omega, T}$ are related by

$$\sigma_T = P_{\omega, T} kT \tag{37}$$

Therefore,

$$P_{\omega, \overline{T}} = P_{\omega, T} \frac{T}{\overline{T}} \tag{38}$$

where $P_{\omega, \overline{T}}$ is the spectral absorption coefficient at the average

temperature $\overline{T}$ of the group of runs. It was assumed that Eq. (38) was valid for $P_{\omega, ap}$ as well as for P_{ω}.

The apparent absorption coefficients of H_2O for nine shock tube runs with an average temperature of 1000 ^{o}K are given in Fig. 29, based on both absorption and emission measurements. Except for one run, $\tilde{P}_{\omega, ap}$ (for emission) was larger than $P_{\omega, ap}$ (for absorption). The effective band widths given are for the monochromator set at 3704 cm^{-1} and would be somewhat different at other wave numbers despite the use of the same slit settings for all runs in the group.

The apparent spectral absorption coefficients for H_2O for sixteen shock tube runs with an effective bandwidth $\Delta\omega$ at 3704 cm^{-1} of 206 cm^{-1} and an average temperature of 1933 ^{o}K are given in Fig. 30 along with coefficients from three runs with $\Delta\omega$ at 3704 cm^{-1} of 69 cm^{-1}, the apparent spectral absorption coefficients of which were also adjusted to 1933 ^{o}K according to Eq. (38). The broadening of the envelope of the bands with increasing temperature is evident when Figs. 29 and 30 are compared.

The two points ⊡ at 3448 cm^{-1} and 3922 cm^{-1} correspond approximately to maxima in $P_{\omega, ap}$ observed in Ref. (19). The point ⊡ at 3774 cm^{-1} corresponds to a minimum in Ref. (19). Since all three points ⊡ were obtained with much smaller effective band width than the points ⊙ through which the curve was drawn, one would expect the two points ⊡ at 3448 cm^{-1} and 3922 cm^{-1} to be located above the curve because of the averaging effect of large effective band width on the curve. By similar reasoning, one would expect the point ⊡ at

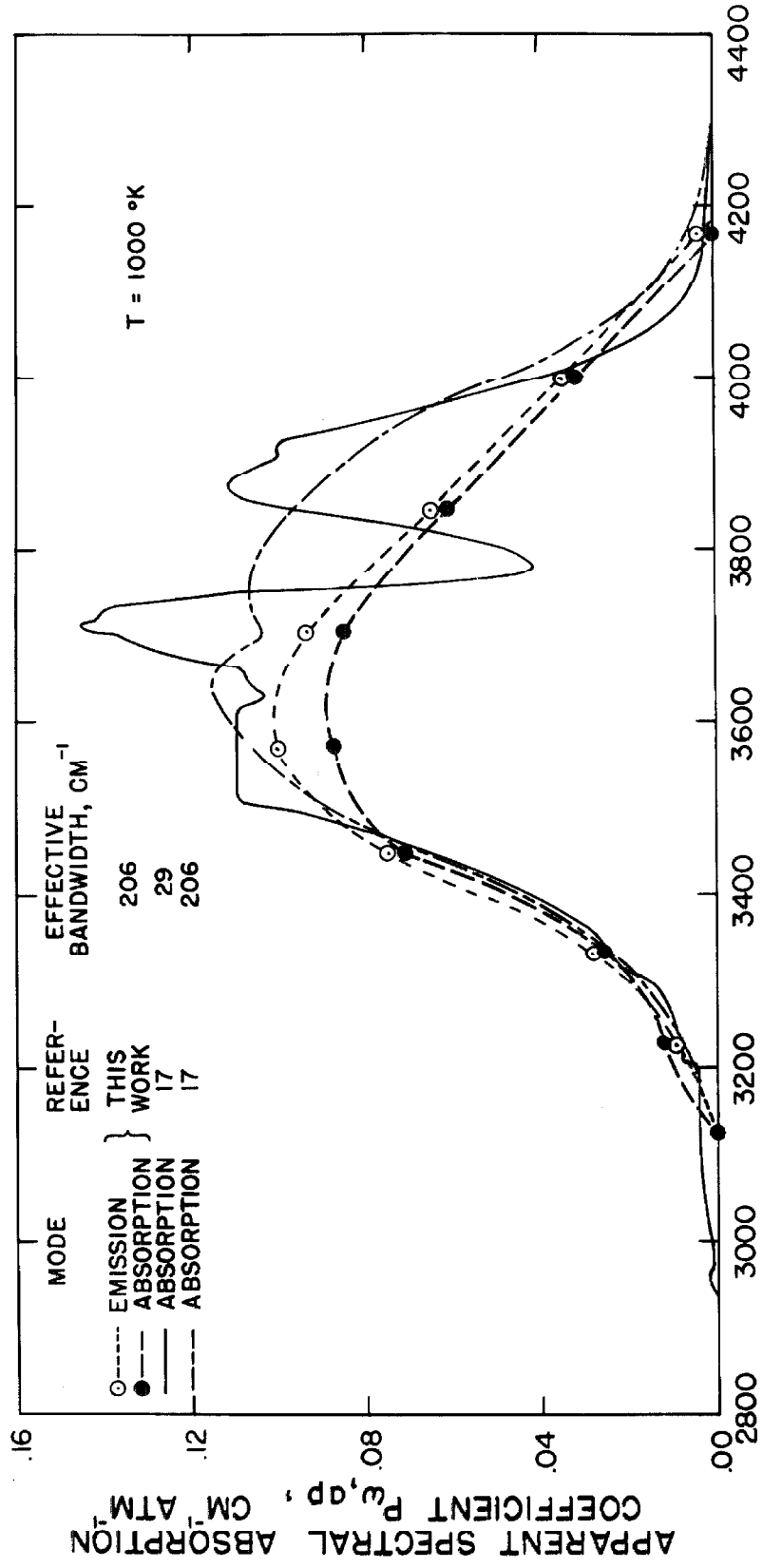

Fig. 29. Graph of spectral absorption coefficients of H_2O vapor obtained in shock tube runs at an average temperature of 1000°K. The coefficient given in Ref. 17 was also included both in its original form and converted to lower resolution.

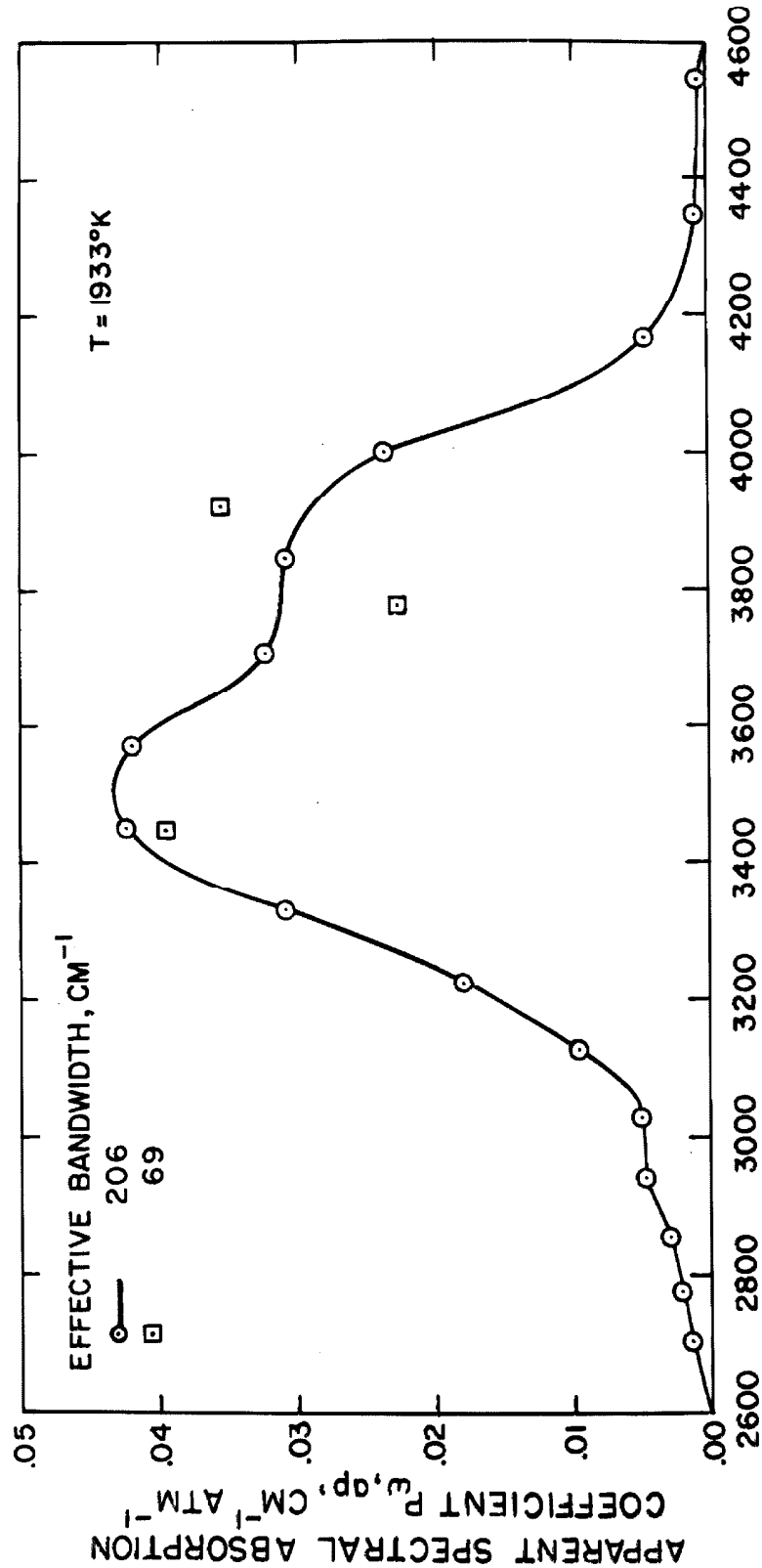

Fig. 30 Graph of the spectral absorption coefficient of H_2O vapor obtained by emission measurements in shock tube runs at an average temperature of 1933° K with effective band width of 206 cm^{-1}. Also included were three points from emission measurements with an effective band width of 69 cm^{-1}.

3774 cm^{-1} to be located below the curve. Two of these three expectations were fulfilled; apparently the point ⊡ at 3448 cm^{-1} was unexpectedly below the curve as the result of scatter of about 15% in the data.

To obtain the integrated absorption coefficients α, the curves in Figs. 29 and 30 were integrated numerically by Simpson's rule. The results are given in Table III.

TABLE III. INTEGRATED ABSORPTION COEFFICIENTS FOR H_2O BANDS BETWEEN 2700 CM^{-1} AND 4550 CM^{-1} OBTAINED FROM SHOCK TUBE MEASUREMENTS

Method	Temperature ^{o}K	Integrated absorption coefficient, α $cm^{-2}atm^{-1}$
absorption	1000	49.8
emission	1000	54.7
emission	1933	31.6

Ideally the two methods of measurement at 1000 ^{o}K should give the same value of α, but in our studies the value of α from emission measurements was 9.8% higher than the value of α from absorption measurements.

C. Estimate of Accuracy

With all factors held as constant as possible, the scatter in the apparent spectral absorption coefficients for a few shock tube runs was about 15%. Consequently, the probable error in α due to random errors should be much less than 15%.

Unfortunately, there were probably some biased errors in addition to the random errors. For example, one chromatographic analysis indicated that the H_2O concentration decreased 7% in 5 min while the mixture was stagnant. Due to the 5% accuracy in such measurements, the actual decrease might have been 12%. If the decrease was linear with time, an error no greater than 5% would occur in shock tube runs and would cause both $P_{\omega, ap}$ and $\tilde{P}_{\omega, ap}$ to be too small.

Another possible cause of biased error was the cement used to hold the shock tube windows in place. Infrared radiation emitted by hot H_2O could be reflected by the cement used to hold the shock tube window on the monochromator side (Fig. 5), partially reflected by the shock tube window on the chopper side, and passed into the monochromator. The magnitude of this effect was difficult to estimate but should be small. The cement on the shock tube window on the chopper side would have an even smaller effect.

Not all of the water vapor in the optical path was in the shock tube: the blackbody had to be open to the atmosphere, the air used in the chopper was not completely dry, the vacuum enclosures did not have perfect vacuums, and a thin layer of air was present between the vacuum enclosure and the detector due to the mounting design. If it is assumed that the ambient relative humidity was 50% at 303 ^{o}K, that the chopper air dew point was 253 ^{o}K, and that all the gas or vapor in the vacuum enclosures was water, then there were 6×10^{-5} precipitable cm of H_2O in the optical path during runs. To obtain a very rough

idea of theabsorption of this H_2O, data from Ref. (7) for H_2O in air at 1 atm and 300 ^{o}K were used. Averaged over 100 cm^{-1}, the absorption should not exceed 3%. This error would tend to cancel out except that the absorption would be higher than 3% near line centers, and these line centers would coincide with H_2O lines in the shock tube.

The shock velocity was measured about 27 cm from the end of the shock tube, and shock velocities are known to decrease with distance[51]. The principal effect would be on the temperature behind the reflected shock wave. Using Emrich and Curtis' correlation[51], the error should not have exceeded 6^{o}K, which is negligibly small.

Possible nonlinearity of the detector could cause an error; with sufficient infrared radiation the number of migrating holes in the p-type photodiode should approach a limit so that the sensitivity would decrease. Use of a filter to decrease the infrared reaching the detector gave just the opposite result, probably due to experimental error instead of nonlinearity of the detector.

In the 1000 ^{o}K group of runs, the intensity of the chopped beam was the same for all runs. Consequently, very small emission intensities were lost in the relatively large 60 kc wave form, resulting in loss of the tails of the band (see Fig. 29). This error probably did not exceed 5%.

It was pointed out in Section IIC that Eq. (24) or, equivalently, Eq. (25), which were used to find α in all cases in both groups of runs, are approximations. To find out what error was involved in the use of Eq. (25), a specific $P_{\omega, ap}$ was selected from Ref. (17) and is shown

as the solid curve in Fig. 29. This $P_{\omega, ap}$ applies to the 3125 cm^{-1} and 3704 cm^{-1} overlapping bands of water vapor at 1000 ^{o}K with $\mathfrak{L}p_{H_2O}$ = 3.8 cm atm and was obtained with a monochromator with a $\Delta\omega$ of 29 cm^{-1} at 3704 cm^{-1}. The $\mathfrak{L}p_{H_2O}$ was practically the same as for the shock tube runs, but $\Delta\omega$ was so much smaller than the 206 cm^{-1} of most of the shock tube runs that it was reasonable to consider the curve from Ref. (17) as a good approximation to the true spectrum.

First the solid curve in Fig. 29 was integrated by Simpson's rule to find α. Then $P_{\omega, ap}$ was computed from it on an IBM 7090 digital computer using Eqs. (13), (15), and (22) and the slit function with 206 cm^{-1} effective band width at 3704 cm^{-1} given in Fig. 25. This is the broader slit function in Fig. 25. The computed $P_{\omega, ap}$ is also plotted in Fig. 29 but is represented by unequal length dashes. The smoothing effect of the wide slit function is apparent. The $P_{\omega, ap}$ curve was next integrated by Simpson's rule to get an α equivalent to α calculated from Eq. (24). This approximate α was 3% higher than the exact α determined directly from the solid curve in Fig. 29. Such an error is considered negligible for shock tube work. In most cases, however, the approximate α is lower than the exact α[13].

Summarizing, the principal errors in the experiments were probably due to reflections from the cement used to hold the shock tube windows in place, adsorption of H_2O on the shock tube walls while stagnant, and absorption by H_2O along the optical path but outside the shock tube. These errors probably did not cause an error in α

exceeding 20%.

VI. DISCUSSION AND COMPARISON OF RESULTS

In this section the difference between the values of integrated absorption coefficients a obtained from shock tube absorption and emission measurements, respectively, is discussed. The integrated absorption coefficients a from the shock tube runs and other investigations are normalized and compared; discrepancies are chiefly due to insufficient collision (pressure) broadening of spectral lines in some investigations.

As noted in Section VB, the value of the integrated absorption coefficient from shock tube emission measurements at 1000 ^{o}K was 9.8% higher than the value from shock tube absorption measurements at 1000 ^{o}K. The two values would have been the same if the gas mixture behind the reflected shock wave had been 18 ^{o}K hotter than calculated from one-dimensional gas dynamics. However, it is not felt that the accuracy of the shock tube measurements warrants any such conclusion. There were two causes that were more probable: 1) infrared radiation from the water vapor in the shock tube may have been reflected from the cement on the edges of the lower shock tube window in Fig. 3 and then reflected by the upper shock tube window into the monochromator entrance optics, and 2) small amounts of H_2O vapor in the optical path between the blackbody and the upper shock tube window in Fig. 3 may have made the 60 kc infrared radiation deficient in intensity at wave numbers corresponding to H_2O lines, thus causing the value of $P_{\omega, ap}$

from absorption measurements to be too small. Before concluding that the gas mixture was 18 ^{o}K hotter than calculated, the experiment should be refined.

In his excellent study Goldstein[17] introduced a normalized integrated absorption coefficient a_n defined by

$$a_n \equiv a \frac{T}{T_o} \tag{39}$$

where T is the temperature at which a was measured, and T_o is some standard temperature (273 ^{o}K for this study). The advantage of the normalized integrated absorption coefficient is that it varies slowly, if at all, with temperature.

The coefficient a_n for all bands between 2700 cm^{-1} and 4550 cm^{-1} taken collectively was calculated from the data of various investigators, using, where possible, only their highest pressure runs because it was expected that only these would have sufficient collision broadening for Eqs. (24) and (25) to be good approximations. Goldstein[17], however, clearly had adequate pressure broadening for all his runs because his data for various pressures fell on a straight line in plots used for the determination of a by standard procedures. Values of a_n from various investigations are given in Table IV. Timnat's value for a_n of 399 cm^{-2}atm^{-1} was omitted from Table IV because he reduced his data using a relation valid only for monochromators with rectangular slit functions, whereas his monochromator had a triangular slit function similar to that shown in Fig. 1A.

TABLE IV. NORMALIZED INTEGRATED ABSORPTION COEFFICIENT a_n OBTAINED BY VARIOUS INVESTIGATORS FOR THE ν_3 H_2O BAND ALONE AND FOR ALL H_2O BANDS IN THE RANGE 2700 CM^{-1} TO 4550 CM^{-1}.

Method	Temperature T,	Partial pressure of H_2O p_{H_2O},	Pressure P,	Broadening gas	Integrated absorption coefficient a_n normalized to 273 °K		Reference	Estimated collision half width b_c of a line,
					000 → 001,	All bands in region,		
	°K	atm	atm		$cm^{-2}atm^{-1}$	$cm^{-2}atm^{-1}$		cm^{-1}
1	1000	0.46	38	Ar		200±20%	This work	1.4
2	1000	0.46	38	Ar		182±20%	This work	1.4
1	1933	1.26	52	Ar		224±20%	This work	1.5
3	473	2.5-18	2.5-18	None		213±10%	17	0.98-7.1
3	673	2.5-18	2.5-18	None		203±10%	17	0.82-5.9
3	873	2.5-18	2.5-18	None		215±10%	17	0.72-5.2
3	1000	2.5-18	2.5-18	None		226±10%	17	0.68-4.9
3	1273	0.26	0.92	N_2		158	14	0.088
3	900	0.99	0.99	None		144	15	0.28
3	1200	0.99	0.99	None		169	15	0.24
3	1500	0.50	0.50	None		157	15	0.11
4	1000	0.36	1	O_2		154±16%	19	0.13
4	1200	0.44	1	O_2		168±13%	19	0.13
4	1500	0.53	1	O_2		176±11%	19	0.13
4	1800	0.63	1	O_2		182±10%	19	0.14
4	2200	0.75	1	O_2		171±11%	19	0.14
5	293	0.0090	0.83	CO_2	166	(186)	20	0.10
6	300	0.040	0.040	None	211±15%	(236)	22	0.020

TABLE IV (Continued)

Key to "Method" column:

1. Emission of bands observed in shock tube.
2. Absorption of bands observed in shock tube.
3. Absorption of bands observed in cell.
4. Absorption of bands observed in rocket exhaust.
5. Absorption of single line observed in cell.
6. Refraction of single line observed in hollow prism.

In two investigations, only α for the $000 \rightarrow 001$ band was given, but $000 \rightarrow 100$ and $000 \rightarrow 020$ contribute significantly in the 2700 cm^{-1} to 4550 cm^{-1} region also. Benedict et al.[10] estimated the $000 \rightarrow 100$ band to have 0.1 of the value of α for the $000 \rightarrow 001$ band, and the $000 \rightarrow 020$ band is still weaker. As a crude approximation, the values of α_n for the $000 \rightarrow 001$ band were multiplied by 1.12 to get α_n for all bands in the 2700 cm^{-1} to 4550 cm^{-1} region, and the latter values are enclosed in parentheses in Table IV.

It was desired to find the collision half width b_c of a line in each of the investigators' experiments. Vasilevsky and Neporent[20] measured the broadening of a line of the $000 \rightarrow 001$ band as H_2O, Ar, N_2, and CO_2 were added, but his optical collision diameters $d_{H_2O\text{-}X}$ were calculated incorrectly. However, Vasilevsky and Neporent defined a quantity $\sigma_{H_2O\text{-}X}$ as the relative broadening ability of gas X on H_2O lines and a quantity γ^o as the hypothetical half width of an H_2O line in pure H_2O vapor at 1 atm pressure and 293 ^oK. Using these two quantities, it is easy to show that

$$b_c = \gamma^o(p_{H_2O} + \sigma_{H_2O\text{-}X} p_X)\sqrt{\frac{293}{T}} \qquad (40)$$

where T is in degrees Kelvin, and the pressures are in atmospheres. Vasilevsky and Neporent found $\gamma^o = 0.5\ cm^{-1}\ atm^{-1}$. Their results for $\sigma_{H_2O\text{-}X}$ are given in Table V.

TABLE V. RELATIVE BROADENING ABILITY OF GAS X ON H_2O LINES[20]

X	$\sigma_{H_2O\text{-}X}$
H_2O	1
Ar	0.123
N_2	0.165
CO_2	0.239

Since no value was given for $\sigma_{H_2O\text{-}O_2}$, it was assumed to be the same as $\sigma_{H_2O\text{-}N_2}$.

Using Eq. (40) and Table V, collision half widths for the cases in Table IV were calculated, entered in Table IV, and plotted in Fig. 31 versus a_n for all bands between 2700 cm^{-1} and 4550 cm^{-1} taken collectively. In Fig. 31 the probable errors in a_n are indicated when available. In the case of the data derived in Ref. (17), average values of b_c were plotted in Fig. 31.

It is clear from Fig. 31 that a_n was higher for higher b_c. However, Goldstein[17] found no significant change in a_n when the pressure was increased by a factor of 7. From this result it is inferred that values of a_n measured with a low resolution monochromator should be substantially constant for H_2O provided b_c is greater than about 0.68 cm^{-1}.

The values of a_n for all bands between 2700 cm^{-1} and 4550 cm^{-1}, taken collectively, were plotted against temperature in Fig. 32. Any

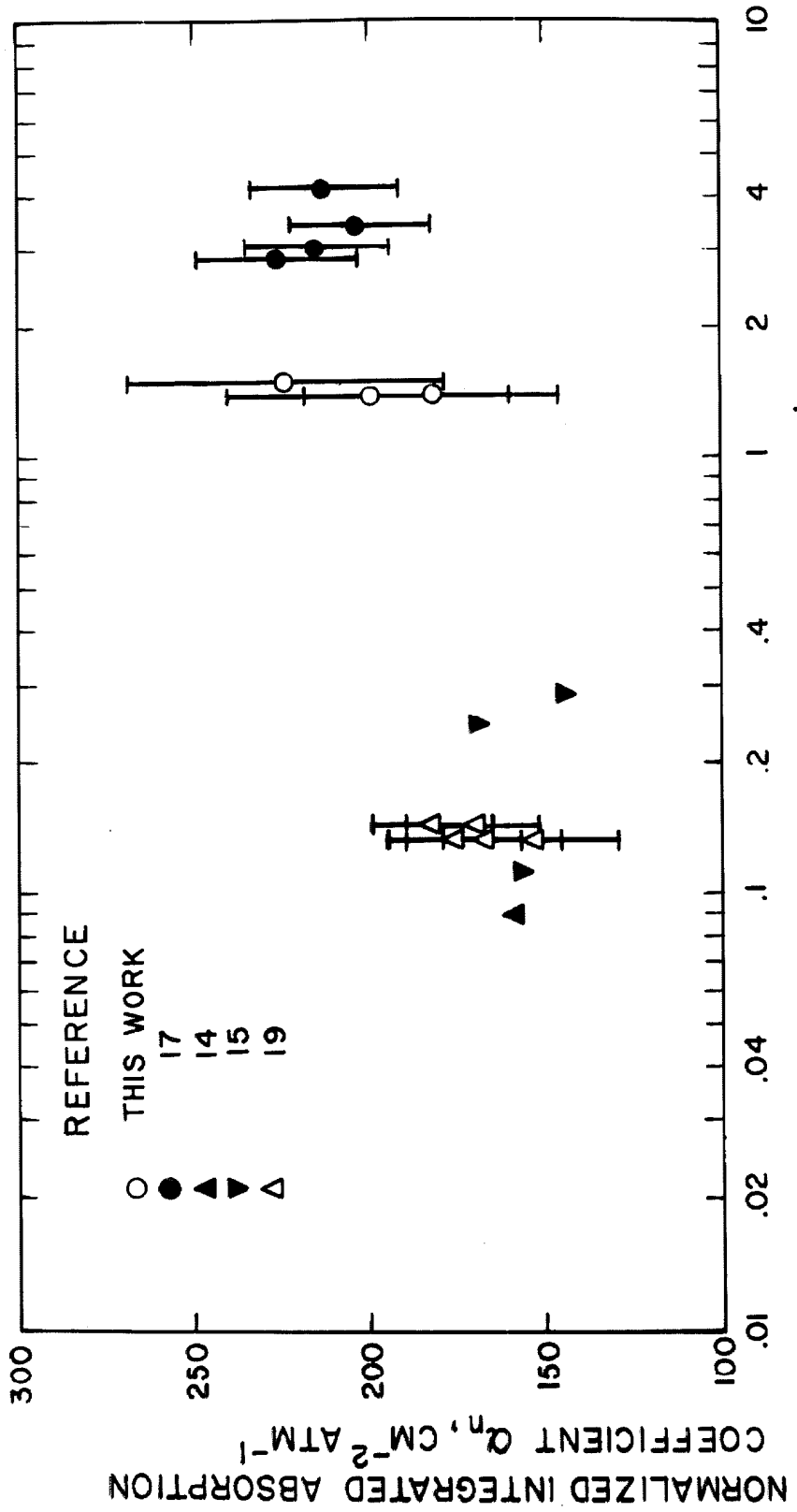

Fig. 31. Graph of the normalized integrated absorption coefficient α_n obtained by various investigators for all H_2O bands in the range 2700 cm^{-1} to 4550 cm^{-1} versus collision half width b_c. The normalization was to 273°K. Investigations based on measurements of single lines were omitted.

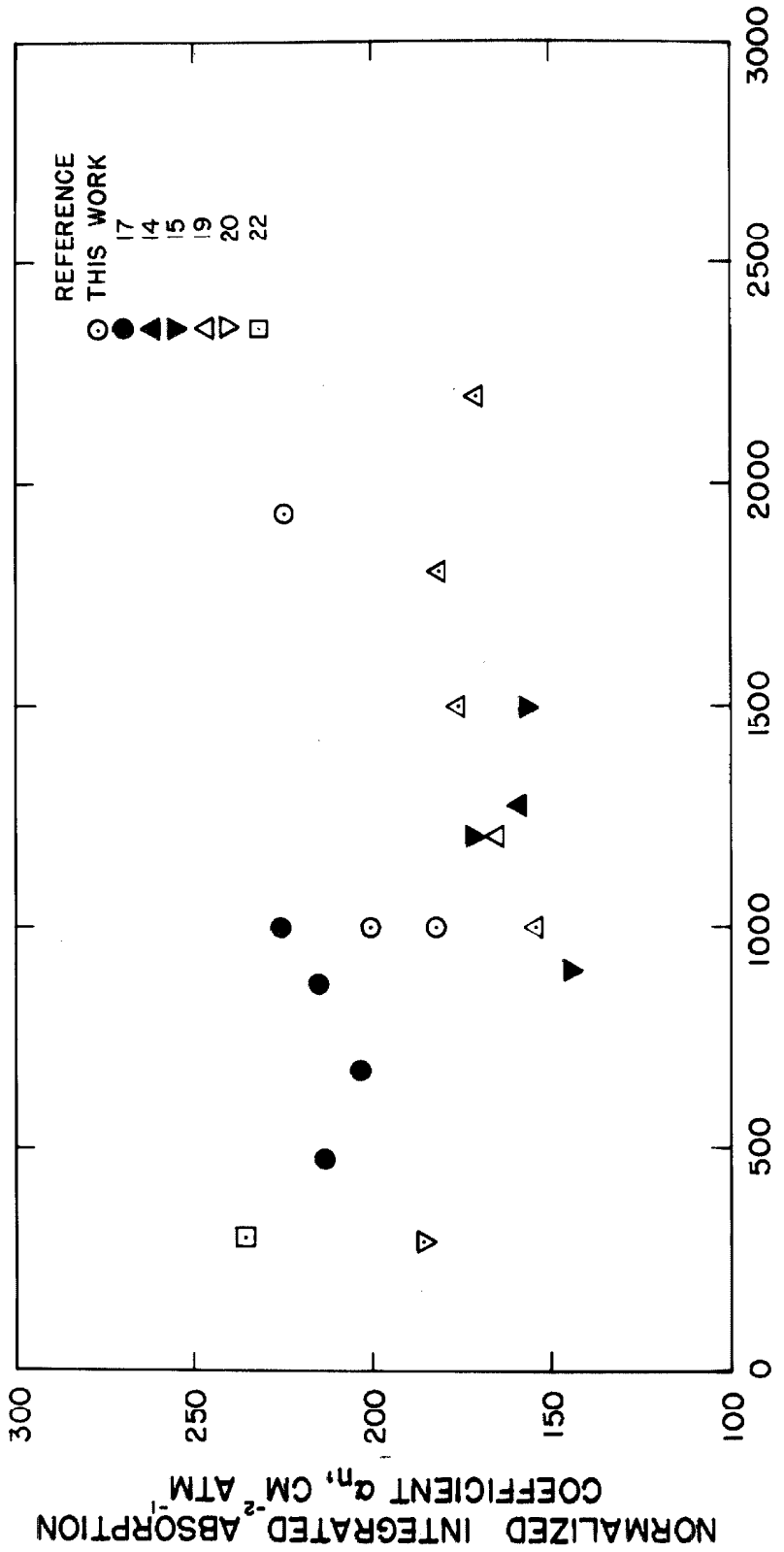

Fig. 32. Graph of the normalized integrated absorption coefficient α_n obtained by various investigators for all H_2O bands in the range 2700 cm^{-1} to 4550 cm^{-1} versus temperature. The normalization was to 273°K.

trend is obscured by the scatter of the points due to insufficient pressure broadening in many of the investigations. If a_n were independent of temperature, a would be proportional to T^{-1} (see Eq. (39)). However, Goldstein[17] made a least-squares fit to his data and found that a was proportional to $T^{-0.93}$ for the bands between 2700 cm^{-1} and 4550 cm^{-1}.

VII. CONCLUSIONS

The described shock tube investigation shows that, when sufficient precautions are taken, both spectral and integrated absorption coefficients can be measured with accuracies nearly as good as those that are obtained in careful equilibrium cell investigations[17]. The agreement of the shock tube results with Goldstein's[17] results gives great confidence that the shock tube can be used as a qualitative research tool at temperatures where the cell method is inapplicable. There can be no doubt that equilibrium cell measurements are always preferable to shock tube measurements when they can be used. The present studies are probably the first shock tube studies in which a precision much better than a factor of two has surely been obtained.

APPENDIX A

Radiant Flux from a Monochromator Focused in a Homogeneous, Non-Scattering, Radiating Substance of Finite Thickness

In Fig. A-1 some plane at a depth ℓ inside a homogeneous radiating substance of thickness $\mathfrak{L}$ and index of refraction near one is focused by means of a lens (not shown) to the left of plane ϕ on to the vertical entrance slit of a monochromator set at ω. The two polyhedrons, to the right and left of the image respectively, contain all points from which emitted light of wave number ω' can produce radiant flux passing through the exit slit of the monochromator. The boundaries of these polyhedrons depend somewhat on ω and ω' because radiant flux of wave number ω' passing through the exit slit of the monochromator depends in general on illumination of only part of the entrance slit. Consequently, a and b are functions of ω and ω'. However, if the exit slit is wider than the entrance slit, then for a range of ω' near ω the entire entrance slit is effective in producing flux passing through the exit slit.

Plane ϕ is located anywhere between the lens and the transparent surface of the container. Plane ϕ and the transparent and black surfaces of the container are all parallel to each other and perpendicular to the optical axis.

Consider an element of area dX dY in plane ϕ. A typical ray passes through dX dY at an angle θ to the optical axis. Let $\mathfrak{F}_{\omega',\phi}$ be the spectral radiant flux through plane ϕ that is effective in producing flux passing through the exit slit although $\mathfrak{F}_{\omega',\phi}$ may subse-

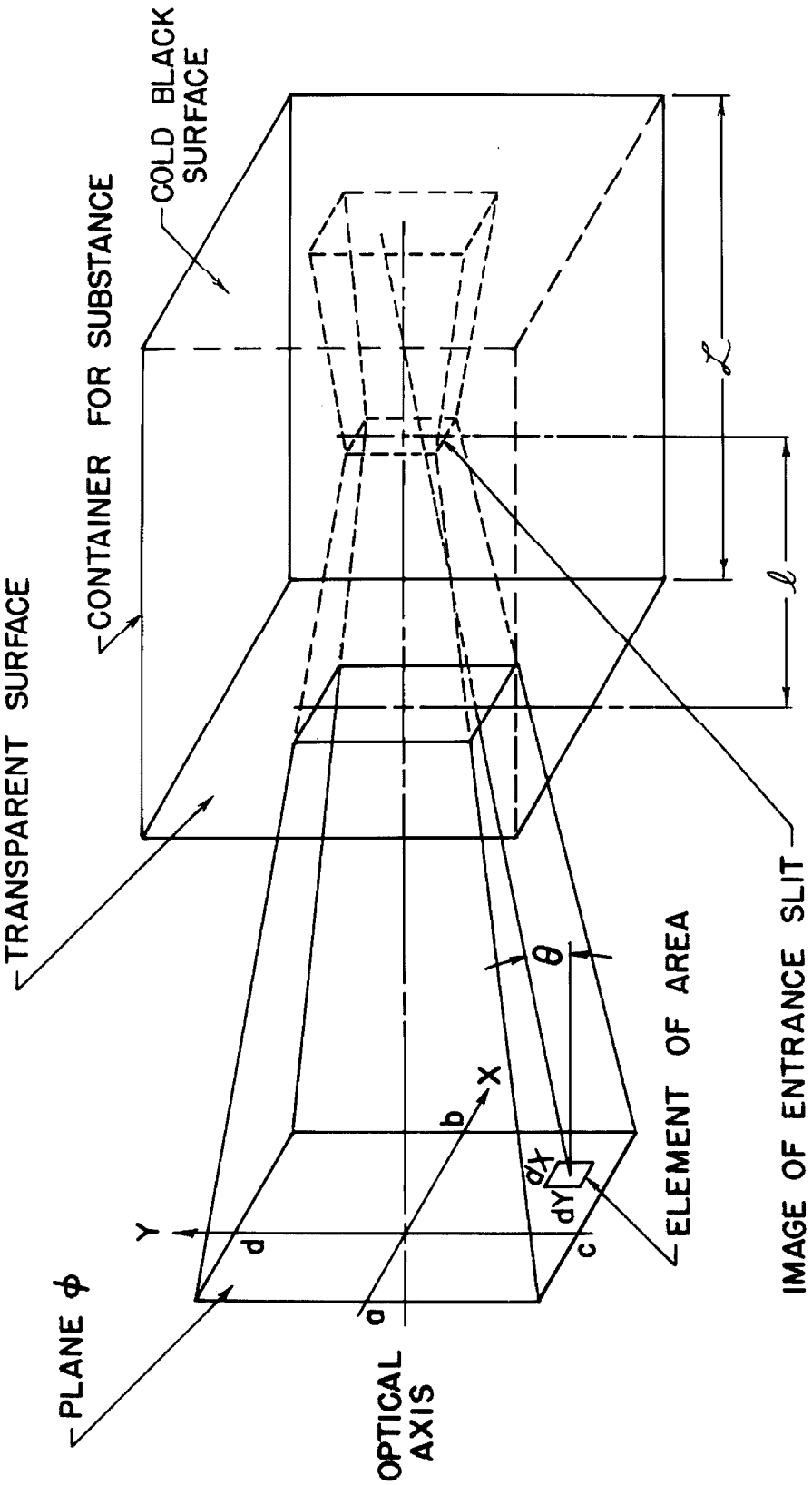

Fig. A-1. Diagram of radiating substance of finite thickness L and of rays to a slit outside the diagram to the left. The slit is focused on a plane at a depth ℓ in the substance.

quently be attenuated slightly by losses in the lens and monochromator.

$$\mathfrak{F}_{\omega', \phi} = \int_c^d \int_{a(\omega, \omega')}^{b(\omega, \omega')} \int_{\Omega(X, Y, \omega, \omega')} B_{\omega', \phi} \, d\Omega \, dX \, dY \qquad (A-1)$$

where $B_{\omega', \phi}$ is the spectral steradiancy at plane ϕ, and $\Omega(X, Y, \omega, \omega')$ is the solid angle at point X, Y effective in producing flux passing through the exit slit. The solid angle $\Omega(X, Y, \omega, \omega')$ at a given X, Y does not necessarily include all points of the image of the entrance slit.

Considering spontaneous emission, absorption, and induced emission but no scattering and assuming local thermodynamic equilibrium, the solution of the equation of radiative transfer for any ray under consideration is[52]

$$B_{\omega', \phi} = \int_0^{\mathcal{T}_{\ell_2}} B^o_{\omega', \mathcal{T}} e^{-\mathcal{T}} \, d\mathcal{T} \qquad (A-2)$$

where $B_{\omega', \phi}$ is the spectral steradiancy at plane ϕ of radiation passing from right to left, $\mathcal{T}_{\ell_2}$ corresponds to where the ray strikes the black surface, and $\mathcal{T}$ is the optical depth, found by integrating along a ray.

$$\mathcal{T} = \int_0^{\ell} K \, ds \qquad (A-3)$$

Here ℓ is the distance along the ray from plane ϕ toward the right, and K is the absorption coefficient in units of length^{-1} and includes induced emission. Let ℓ_1 be the point where the ray intercepts the transparent surface. Then

$$\mathcal{T} = K(\ell - \ell_1) \qquad (A-4)$$

$$B_{\omega',\phi} = B^{o}_{\omega',\mathscr{s}} K \int_{\mathscr{s}_1}^{\mathscr{s}_2} e^{-K(\mathscr{s}-\mathscr{s}_1)} ds \qquad (A-5)$$

where $B^{o}_{\omega',\mathscr{s}}$ is the blackbody steradiancy at the temperature of the substance. Integrating,

$$B_{\omega',\phi} = B^{o}_{\omega',\mathscr{s}}(1 - e^{-K(\mathscr{s}_2-\mathscr{s}_1)}) \qquad (A-6)$$

or

$$B_{\omega',\phi} = B^{o}_{\omega',\mathscr{s}}(1 - e^{-K\mathscr{L}\sec\theta}) \qquad (A-7)$$

If the f-number of the optics is large, $\sec\theta \approx 1$, so Eq. (A-1) becomes

$$\mathfrak{F}_{\omega',\phi} = B^{o}_{\omega',\mathscr{s}}(1 - e^{-K\mathscr{L}}) \int_c^d \int_{a(\omega,\omega')}^{b(\omega,\omega')} \int_{\Omega(X,Y,\omega,\omega')} d\Omega\, dX\, dY \qquad (A-8)$$

To find the flux $\mathfrak{F}_{\omega',e}$ passing through the exit slit, a transmission factor $A(X, Y, \Omega, \omega, \omega')$ slightly less than one must be used because of losses at the lens and in the monochromator. Eq. (A-8) becomes

$$\mathfrak{F}_{\omega',e} = B^{o}_{\omega',\mathscr{s}}(1 - e^{-K\mathscr{L}}) \int_c^d \int_{a(\omega,\omega')}^{b(\omega,\omega')} \int_{\Omega(Y,Y,\omega,\omega')} A(X, Y, \Omega, \omega, \omega')\, d\Omega\, dX\, dY \qquad (A-9)$$

Integrating yields the total radiant flux $\mathfrak{F}_e$ passing through the exit slit.

$$\mathfrak{F}_e = \int_0^\infty B^{o}_{\omega',\mathscr{s}}(1 - e^{-K\mathscr{L}}) \int_c^d \int_{a(\omega,\omega')}^{b(\omega,\omega')} \int_{\Omega(X,Y,\omega,\omega')} A(X, Y, \Omega, \omega, \omega')\, d\Omega\, dX\, dY\, d\omega' \qquad (A-10)$$

Let

$$F_\omega g(\omega'-\omega, \omega) = \int_c^d \int_{a(\omega, \omega')}^{b(\omega, \omega')} \int_{\Omega(X, Y, \omega, \omega')} A(X, Y, \Omega, \omega, \omega')\, d\Omega\, dX\, dY \tag{A-11}$$

where g is the slit function defined in Section IIB, and F_ω varies in such a manner that g can satisfy Eq. (11). Combining Eqs. (A-10) and (A-11),

$$\mathfrak{F}_e = F_\omega \int_0^\infty B^o_{\omega', \mathcal{A}} (1-e^{-K\mathfrak{L}}) g(\omega'-\omega, \omega)\, d\omega' \tag{A-12}$$

Note that $\mathfrak{F}_e$ does not depend on the dimension ℓ in Fig. A-1.

APPENDIX B

Elimination of Error in an Absolute Intensity Calibration Using an Off-Axis Spherical Concave Mirror

Consider an optical system consisting of a spherical concave mirror of radius ρ and a light source with steradiancy B_{bb} constant across its aperture, arranged as in Fig. B-1. From the equation of radiative transfer[52] the steradiancy B_{bb} does not vary along a ray from the source to the mirror provided no absorbing or scattering medium intervenes. Let B_r be the steradiancy of the reflected ray, and R_m be the reflectivity of the mirror. Then[53]

$$B_r = R_m B_{bb} \tag{B-1}$$

Similarly, B_r does not vary from the mirror to the image. However, the image is blurred, so for accurate absolute intensity calibration it is necessary to use only the central part of the image from which the source aperture can be seen through all points of the surface of the mirror.

To determine the useable portion of the image it is necessary to examine the aberrations of the system. With the arrangement of Fig. B-1 astigmatism is the principal aberration. In a side view the source and image coincide with the center of curvature, so there is little or no aberration. For a top view the aberration of an extreme ray is easily found. The law of tangents gives

$$\frac{M - \rho}{M + \rho} = \frac{\tan \frac{\psi - \xi}{2}}{\tan \frac{\psi + \xi}{2}} = \frac{\tan \left(\psi - \frac{\zeta}{2} - \frac{\pi}{4}\right)}{\tan \left(\frac{\zeta}{2} + \frac{\pi}{4}\right)} \tag{B-2}$$

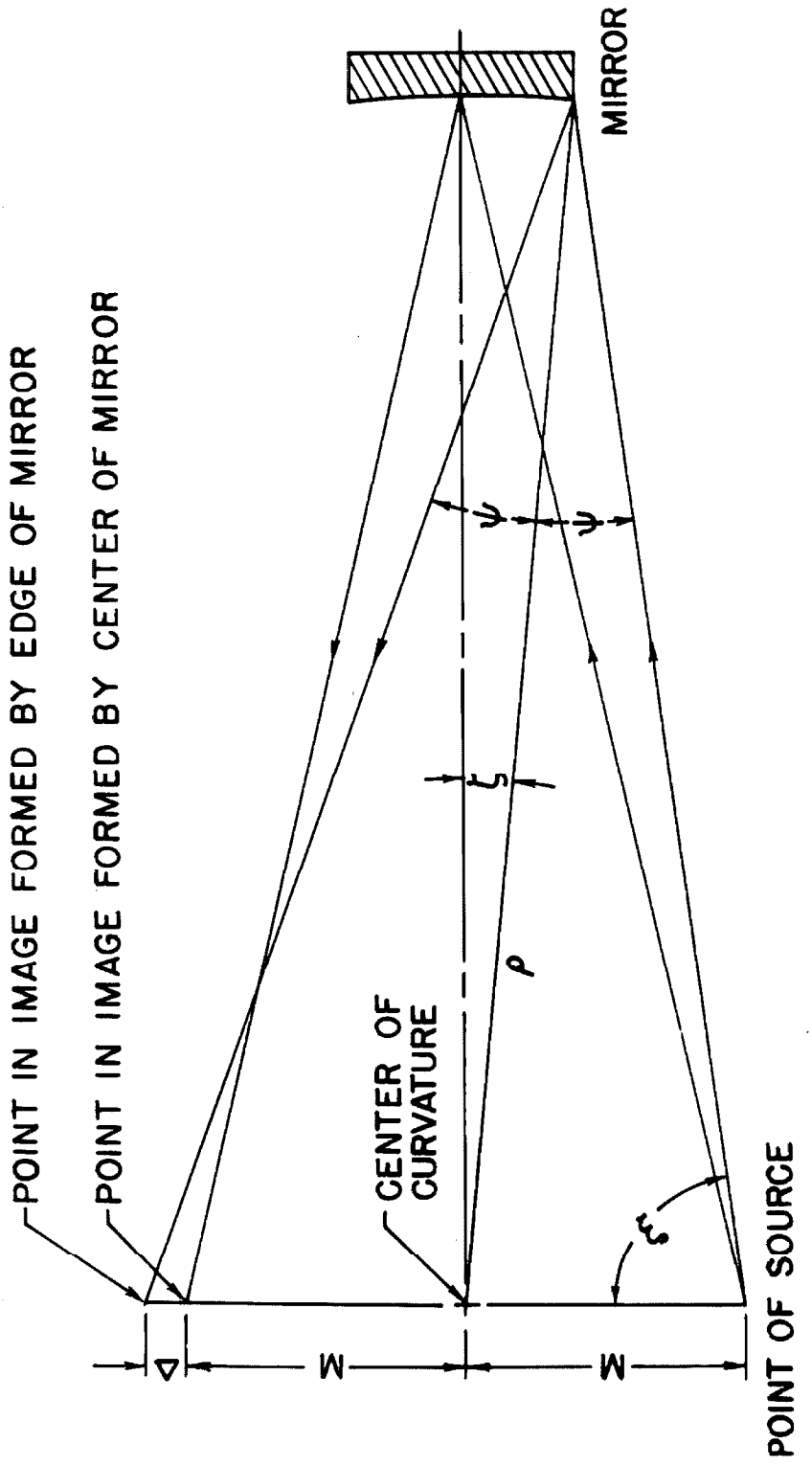

Fig. B-1. Diagram of optical system for absolute intensity calibration, showing quantities used to compute astigmatism Δ in the plane containing the centers of the source and image and the center of curvature of the mirror. The view is from the top.

so

$$\psi = \frac{\zeta}{2} + \frac{\pi}{4} + \arctan\left[\frac{M - \rho}{M + \rho} \tan \left(\frac{\zeta}{2} + \frac{\pi}{4} \right) \right] \qquad \text{(B-3)}$$

By the law of sines

$$\frac{M + \Delta}{\sin \psi} = \frac{\rho}{\sin \left(\frac{\pi}{2} - \zeta - \psi \right)} \qquad \text{(B-4)}$$

or

$$\Delta = \frac{\rho \sin \psi}{\cos (\zeta + \psi)} - M \qquad \text{(B-5)}$$

A similar expression can be derived for the aberration of a ray reflected from the other side of the mirror, so the image of the point in the source is spread over a width of about 2Δ. Thus if the width of the aperture of the source is w, the useable width of the image is $w - 2\Delta$.

APPENDIX C

Effective Transmission of a Window at Near Normal Incidence with Media of Equal Indices of Refraction on Either Side

Consider a ray of steradiancy $B_{\omega',1}$ in a medium of index of refraction n_1 incident on a non-absorbing window with index of refraction n_2, as shown in Fig. C-1. Let r be the reflectivity of the 1-2 interface and also the 2-3 interface on the opposite face of the window. The relation of the steradiancies of incident and refracted rays has been derived[53] and is

$$B_{\omega',2} = B_{\omega',1}(1 - r)U \tag{C-1}$$

where $B_{\omega',2}$ is the steradiancy of the refracted ray in region 2, and U is defined by

$$U \equiv \left(\frac{n_2}{n_1}\right)^2 \tag{C-2}$$

Similarly, when a ray of steradiancy $B_{\omega',2}$ is incident on the right hand interface

$$B_{\omega',3} = \frac{B_{\omega',2}(1 - r)}{U} = B_{\omega',1}(1 - r)^2 \tag{C-3}$$

where $B_{\omega',3}$ is the steradiancy in region 3.

In Fig. C-1 the results of additional reflections are shown. Neglecting interference effects, let $\sum B_{\omega',3}$ be the sum of an infinite number of reflections. Then

$$\sum B_{\omega',3} = B_{\omega',1}(1 - r^2)(1 + r^2 + r^4 + \ldots)$$

$$= \frac{B_{\omega',1}(1 - r)^2}{1 - r^2} \tag{C-4}$$

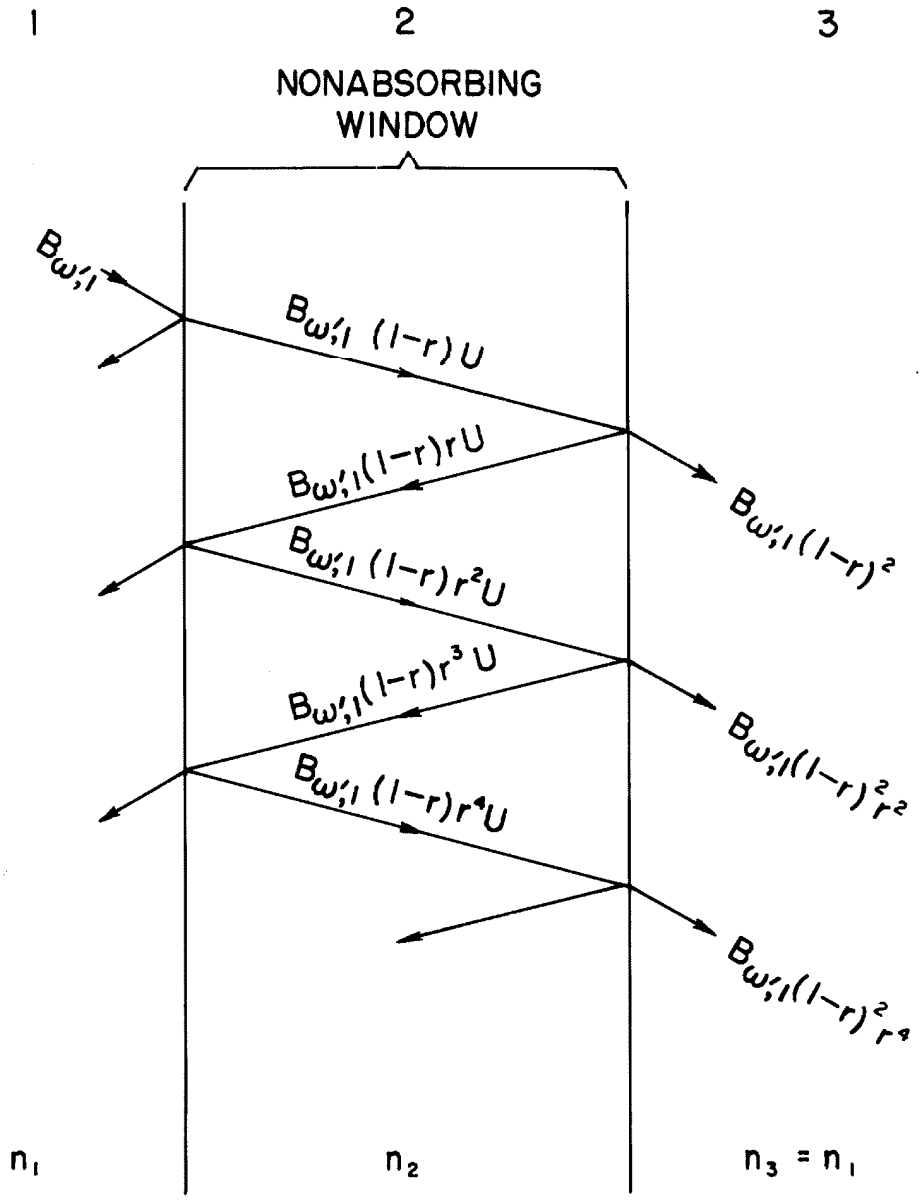

Fig. C-1. Diagram of multiple reflections of a single ray inside a window at near-normal incidence (the angles of incidence, reflection, and refraction have been exaggerated).

Therefore the fraction of energy transmitted by the window at wave number ω' is

$$t_{\omega'} = \frac{\sum B_{\omega', 3}}{B_{\omega', 1}} = \frac{(1 - r)^2}{1 - r^2} \qquad \text{(C-5)}$$

Since it was assumed that the incident ray in region 1 has near normal incidence, r for normal incidence[54] is used as an approximation:

$$r = \left(\frac{n_1 - n_2}{n_1 + n_2}\right)^2 \qquad \text{(C-6)}$$

which is equally valid for either of the two interfaces.

APPENDIX D

Steradiancy Outside a Homogeneous, Non-Scattering, Radiating Substance Contained between Two Parallel Partially-Reflecting Windows

Consider a homogeneous, non-scattering, radiating substance contained between two parallel non-absorbing windows shown in Fig. D-1, each having an effective transmission $t_{\omega'}$ calculated by the method given in Appendix C for near-normal rays. Assume the substances to the left of the window bd and to the right of the window ace are transparent and have indices of refraction n_1 and n_3, respectively, which are about the same as n_2 of the radiating substance. It is desired to find $B_{\omega'}$, the spectral steradiancy of a ray transmitted through the right-hand window at a. Since only near-normal rays will be considered, the path length L may be approximated by the thickness $\mathcal{L}$.

Assume that the radiating substance is in local thermodynamic equilibrium and has an absorption coefficient K in units of length^{-1}. Then the contribution $\delta_a B_{\omega'}$ to $B_{\omega'}$ by the radiating substance between a and b is, according to the solution of the equation of radiative transfer,

$$\delta_a B_{\omega'} = B^o_{\omega', s}(1 - e^{-K\mathcal{L}})t_{\omega'} \qquad \text{(D-1)}$$

where $B^o_{\omega', s}$ is the blackbody steradiancy at the temperature of the substance. The contribution by the radiating substance between b and c is

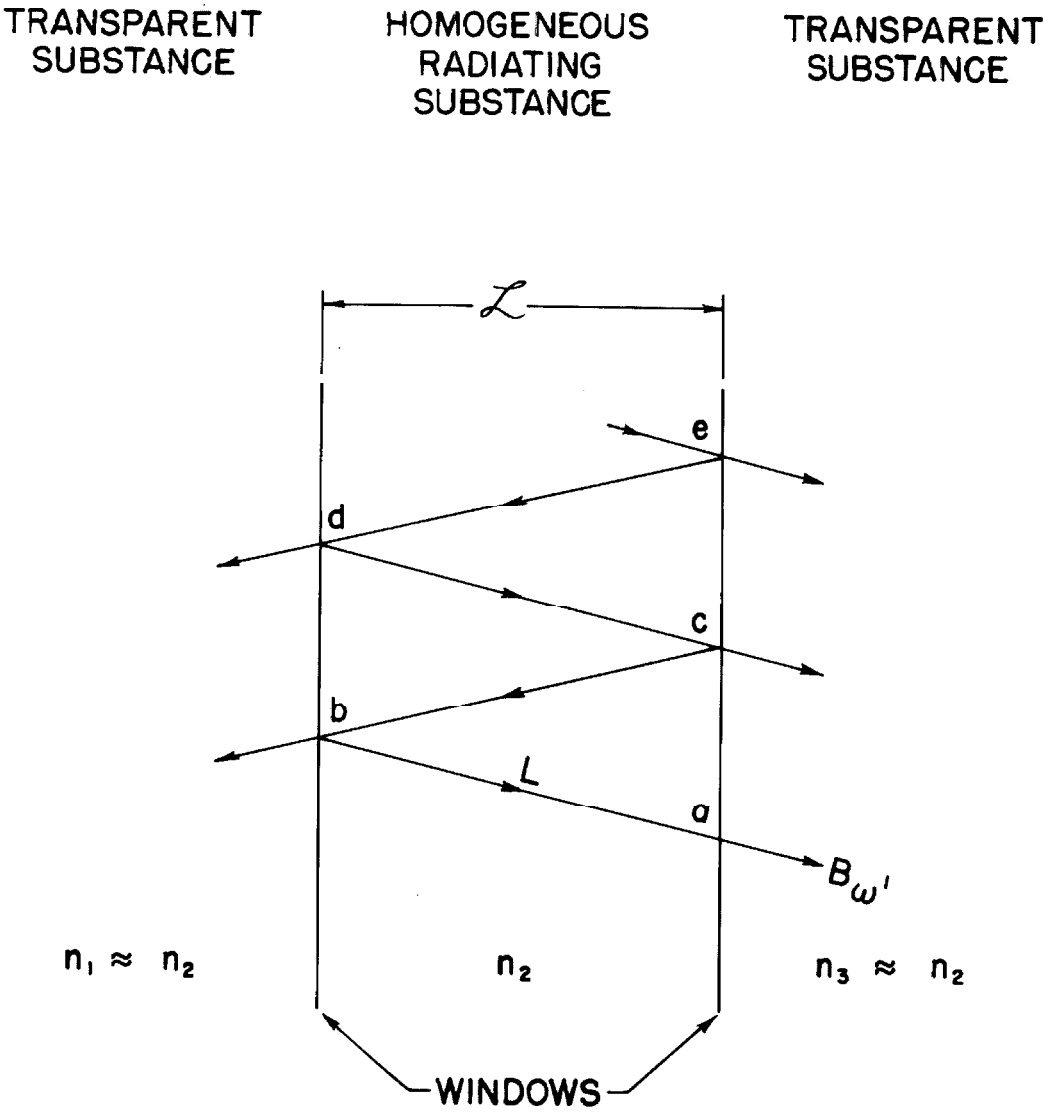

Fig. D-1. Diagram of multiple reflections of a near-normal ray in a homogeneous, nonscattering, radiating substance contained between two parallel partially-reflecting nonabsorbing windows. The windows are represented by lines. The angles of incidence and reflection have been exaggerated.

$$\delta_b B_{\omega'} = B^o_{\omega', s}(1 - e^{-K\mathfrak{L}})e^{-K\mathfrak{L}}(1 - t_{\omega'})t_{\omega'} \qquad (D\text{-}2)$$

where the factor $(1 - t_{\omega'})$ is the fraction reflected at point b, and the factor $\exp(-K\mathfrak{L})$ is the fraction not absorbed while passing from b to a. Similarly

$$\delta_c B_{\omega'} = B^o_{\omega', s}(1 - e^{-K\mathfrak{L}})e^{-2K\mathfrak{L}}(1 - t_{\omega'})^2 t_{\omega'} \qquad (D\text{-}3)$$

Considering an infinite number of such contributions, $B_{\omega'}$ becomes

$$B_{\omega'} = \sum \delta_i B_{\omega'} = B^o_{\omega', s}\left[1 - e^{-K\mathfrak{L}}\right]t_{\omega'}\left[1 + (1 - t_{\omega'})e^{-K\mathfrak{L}} + (1 - t_{\omega'})^2 e^{-2K\mathfrak{L}} + (1-t_{\omega'})^3 e^{-3K\mathfrak{L}} + \ldots\right] \qquad (D\text{-}4)$$

Thus

$$\frac{B_{\omega'}}{B^o_{\omega', s}} = \frac{(1 - e^{-K\mathfrak{L}})t_{\omega'}}{1 - (1 - t_{\omega'})e^{-K\mathfrak{L}}} \qquad (D\text{-}5)$$

REFERENCES FOR PART II

1. S. S. Penner, Quantitative Molecular Spectroscopy and Gas Emissivities, Addison-Wesley, Reading, Mass., 1959.

2. R. A. Allen, J. C. Camm, and J. C. Keck, "Radiation from Hot Nitrogen," J. Quant. Spectr. Radiat. Transfer, 1, 269-277 (1961).

3. J. Keck, J. Camm, B. Kivel, and T. Wentink, "Radiation from Hot Air. Part II. Shock Tube Study of Absolute Intensities," Ann. Phys. 7, 1-38 (1959).

4. S. S. Penner, "Oscillator Strengths of the Ultraviolet γ Bands of NO," J. Opt. Soc. Am. 50, 627 (1960).

5. P. C. Cross, R. M. Hainer, and G. W. King, "The Asymmetric Rotor. II. Calculation of Dipole Intensities and Line Classification," J. Chem. Phys. 12, 210-243 (1944).

6. G. Yamamoto and G. Onishi, "Absorption Coefficient of Water-Vapour in the Near Infra-Red Region," Science Reports of Tohoku U., ser. 5, Geophysics, 1, 71-75 (1949).

7. P. J. Wyatt, V. R. Stull, and G. N. Plass, "Infrared Transmission Studies Final Report. Vol. II. The Infrared Absorption of Water Vapor," Aeronutronic Div. Ford Motor Co., Report No. SSD-TDR-62-127, September 1962.

8. Louise D. Gray, "Theoretical Calculations of Equilibrium Infrared Gas Emissivities from Spectroscopic Data," Part I, Ph. D. Thesis, Calif. Inst. of Tech., 1963.

9. W. S. Benedict and Earle K. Plyler, "Absorption Spectra of Water Vapor and Carbon Dioxide in the Region of 2.7 Microns," J. Res. NBS 46, 246-265 (1951).

10. W. S. Benedict, N. Gailar, and Earle K. Plyler, "Rotation-Vibration Spectra of Deuterated Water Vapor," J. Chem. Phys. 24, 1139-1165 (1956).

11. E. Bright Wilson, Jr., J. C. Decius, and Paul C. Cross, Molecular Vibrations, McGraw-Hill, New York, 1955.

12. Gerhard Herzberg, Molecular Spectra and Molecular Structure. II. Infrared and Raman Spectra of Polyatomic Molecules, D. Van Nostrand, New York, 1945.

13. John Nelson Howard, Darrell L. Burch, and Dudley Williams, "Near-Infrared Transmission Through Synthetic Atmospheres," Ohio State U. Report No. AFCRC-TR-55-213, November 1955. Also see J. Opt. Soc. Am. 46, 186-190 (1956) and 46, 242-245 (1956).

14. Richard H. Tourin, "Spectral Emissivities of Hot CO_2-H_2O Mixtures in the 2.7μ Region," J. Opt. Soc. Am. 51, 799-800 (1961).

15. Darrell E. Burch and David A. Gryvnak, "Infrared Radiation Emitted by Hot Gases and Its Transmission through Synthetic Atmospheres," Aeronutronic Div. Ford Motor Co. Report No. U-1929, October 1962.

16. Gunter J. Penzias, G. Jordan Maclay, and Harold J. Babrov, "Infrared Analysis of High Temperature Gases in Situ," NASA CR-1, October 1962.

17. R. Goldstein, "Quantitative Spectroscopic Studies on the Infrared Absorption by Water Vapor and Liquid Water," Ph. D. Thesis, Calif. Inst. of Tech., 1964.

18. Keith Ernest Nelson, "Experimental Determination of the Band Absorptivities of Water Vapors at Elevated Pressures and Temperatures," M. S. Thesis, U. of Calif. at Berkeley, 1959.

19. Carmine C. Ferriso and Claus B. Ludwig, "High Temperature Emissivities of the 2.7 Micron Band of H_2O between 1000 ^oK and 2200 ^oK," General Dynamics/Astronautics Space Science Laboratory Report No. BBE63-002, April 1963.

20. K. P. Vasilevsky and B. S. Neporent, "Effect of Foreign Gases on the Absorption of Infrared Radiation by Water Vapors in the Region of an Individual Line in Band 2.7μ," Opt. Spectrosc. (translation) 7, 353-354 (1959).

21. W. S. Benedict, private communication, 1964.

22. J. H. Jaffe and W. S. Benedict, "The Strength of the ν_3 Vibration of H_2O," J. Quant. Spectrosc. Radiat. Transfer 3, 87-88 (1963).

23. R. Rollefson and A. H. Rollefson, "The Optical Dispersion of HCl in the Infrared," Phys. Rev. 48, 779-785 (1935).

24. Y. M. Timnat, "Preliminary Study of Infrared Absorption of Water behind Incident Shock Waves," Technical Report No. 40, Contract Nonr-220(45), NR 015 401, Calif. Inst. of Tech., August 1962.

25. George Rudinger, Wave Diagrams for Nonsteady Flow in Ducts, D. Van Nostrand, New York, 1955.

26. Otto Laporte and Thomas D. Wilkerson, "Hydrodynamic Aspects of Shock Tube Spectroscopy," J. Opt. Soc. Am. 50, 1293-1299 (1960).

27. W. C. Gardiner, Jr. and G. B. Kistiakowsky, "Density Measurements in Reflected Shock Waves," J. Chem. Phys. 34, 1080-1081 (1961).

28. T. A. Brabbs, S. A. Zlatarich, and F. E. Belles, "Limitations of the Reflected-Shock Technique for Studying Fast Chemical Reactions," J. Chem. Phys. 33, 307-308 (1960).

29. Gordon B. Skinner, "Limitations of the Reflected Shock Technique for Studying Fast Chemical Reactions," J. Chem. Phys. 31, 268-269 (1959).

30. R. A. Alpher and D. R. White, "Flow in Shock Tubes with Area Change at the Diaphragm Section," J. Fluid Mech. 3, 457-470 (1958).

31. S. Byron and N. Rott, "On the Interaction of the Reflected Shock Wave with the Laminar Boundary Layer on the Shock Tube Walls," pp. 38-54 in Proceedings of the 1961 Heat Transfer and Fluid Mechanics Institute edited by R. C. Binder, M. Epstein, R. L. Mannes, and H. T. Yang, Stanford Univ. Press, Stanford, 1961.

32. Paul W. Huber and Arthur Kantrowitz, "Heat-Capacity Lag Measurements in Various Gases," J. Chem. Phys. 15, 275-284 (1947).

33. I. H. Malitson, F. V. Murphy, and W. S. Rodney, "Refractive Index of Synthetic Sapphire," J. Opt. Soc. Am. 48, 72-73 (1958).

34. H. E. Bennett and W. F. Koehler, "Precision Measurement of Absolute Specular Reflectance with Minimized Systematic Errors," J. Opt. Soc. Am. 50, 1-6 (1960).

35. J. J. Chessick, F. H. Healey, and A. C. Zettlemayer, "Adsorption and Heat-of-Wetting Studies of Teflon," J. Phys. Chem. 60, 1345-1347 (1956).

36. T. A. Jacobs, "Consideration of Some Electronic Components in Shock Tube Instrumentation," Technical Report No. 2, Contract AF 49(638)-984, Calif. Inst. of Tech., 1961.

37. William Joseph Hooker, "Shock-Induced C_2H_2 Pyrolysis and CO Emissivity," Ph.D. Thesis, Calif. Inst. of Technology, 1958.

38. Leroy W. Tilton and Earle K. Plyler, "Refractivity of Lithium Fluoride with Application to the Calibration of Infrared Spectrometers," J. Res. NBS 47, 25-30 (1951).

39. A. B. Naugle, V. R. Allen and A. J. Cussen, "Properties of Photoconductive Detectors," NAVORD Reports 4641, 4642, and 4646, U. S. Naval Ordnance Laboratory, Corona, November-December 1957.

40. Ronald Watson, "Procedure for Reliable Preparation of Shock Tube Test Gas Mixtures Containing Water Vapor," Rev. Sci. Instr. 33, 1113-1114 (1962).

41. Charles D. Hodgman, Robert C. Weast, and Samuel M. Selby (editors), Handbook of Chemistry and Physics, 40th ed., Chemical Rubber Publishing, Cleveland, 1958.

42. Earle K. Plyler, L. R. Blaine, and Matthew Nowak, "Reference Wavelengths for Calibrating Prism Spectrometers," J. Res. NBS 58, 195-200 (1957).

43. G. K. T. Conn and D. G. Avery, Infrared Methods, Academic Press, New York, 1960.

44. Anonymous, "Tables for the Spectral Radiant Intensity of a Blackbody and of a Tungsten Ribbon," Rocketdyne Research Rept. 59-32, Canoga Park, Calif., undated.

45. Roger L. Wilkins, Theoretical Evaluation of Chemical Propellants, Prentice Hall, Englewood Cliffs, N. J., 1963.

46. Bonnie J. McBride, Sheldon Heimel, Janet G. Ehlers, and Sanford Gordon, "Thermodynamic Properties to 6000 ^{o}K for 210 Substances Involving the First 18 Elements," NASA Interim Draft, July 1963.

47. Leonard Glatt, Joan H. Adams, and Herrick L. Johnston, "Thermodynamic Properties of the H_2O Molecule from Spectroscopic Data," Ohio State U. Technical Report TR 316-8, June 1953.

48. Bonnie J. McBride and Sanford Gordon, "Thermodynamic Functions of Several Triatomic Molecules in the Ideal Gas State," J. Chem. Phys., 35, 2198-2206 (1961).

49. Anonymous, "Selected Values of Chemical Thermodynamic Properties. Series III." NBS, 1954.

50. Abraham S. Friedman and Lester Haar, "High-Speed Machine Computation of Ideal Gas Thermodynamic Functions. I. Isotopic Water Molecules," J. Chem. Phys. 22, 2051-2058 (1954).

51. R. J. Emrich and C. W. Curtis, "Attenuation in the Shock Tube," J. App. Phys. 24, 360-363 (1953).

52. S. Chandrasekhar, An Introduction to the Study of Stellar Structure, Dover, New York, 1957.

53. L. C. Martin, Geometrical Optics, Philosophical Library, Inc., New York, 1956.

54. F. Woodbridge Constant, Theoretical Physics. Thermodynamics, Electromagnetism, Waves, and Particles, Addison-Wesley, Reading, Mass., 1958.